New frontiers in THz quantum cascade lasers

by

Ali Khalatpour

B.A.Sc, Electrical Engineering
Amirkabir University of Technology (2009)
M.A.Sc Electrical Engineering and Computer Science
McMaster University (2011)
M.Sc Physics
University of Toronto (2014)

Submitted to the Department of Electrical Engineering and Computer Science
in partial fulfillment of the requirements for the degree of

Doctor of Philosophy in Electrical Engineering and Computer Science

at the

MASSACHUSETTS INSTITUTE OF TECHNOLOGY

September 2020

Author . . . .
Department of Electrical Engineering and Computer Science
August 28, 2020

Certified by . . . .
Qing Hu
Distinguished Professor
Department of Electrical Engineering and Computer Science
Thesis Supervisor

Accepted by . . . .
Leslie A. Kolodziejski
Professor of Electrical Engineering and Computer Science
Chair, Department Committee on Graduate Students

New frontiers in THz quantum cascade lasers

by

Ali Khalatpour

Submitted to the Department of Electrical Engineering and Computer Science
on August 28, 2020, in partial fulfillment of the
requirements for the degree of
Doctor of Philosophy in Electrical Engineering and Computer Science

Abstract

Terahertz (THz) frequencies (0.5-10 THz) are among the most underdeveloped electromagnetic spectra, even though their application potentials are great in imaging, sensing, and communications. This underdevelopment is primarily due to the lack of compact and powerful THz sources. The invention of THz quantum cascade lasers (QCL) held great promise to bridge the gap between semiconductor electronic and photonic devices. However, the demanding cooling requirements for THz QCL have been a hard brake in the race for achieving compact and portable systems, and they have confined THz QCL systems to a laboratory environment. Therefore, raising the maximum operating temperature to above that of a compact cooler (≥ 235 K for single-stage thermoelectric coolers), has been a paramount long-term goal in the THz field. In this thesis, THz QCLs (at ≈ 4 THz) with a maximum operating temperature T_{max}= 250 K has been developed. This operating temperature enabled the construction of coherent THz radiation sources using cheap commercial single- and multi-stage thermoelectric coolers, yet with power levels sufficient for real-time imaging of beam pattern and fast spectral measurements without requiring expensive cryogenically cooled detectors. The combination of TEC-cooled THz QCLs with room-temperature cameras and detectors enables portable systems that are operable outside the laboratory environment. Furthermore, and perhaps more importantly, the demonstrated significant increase in T_{max} and the preservation of room-temperature NDR pave a clear path toward further increases in T_{max}: designing clean n-level systems based on the direct-phonon scheme with tall barriers.

Thesis Supervisor: Qing Hu
Title: Distinguished Professor
Department of Electrical Engineering and Computer Science

Acknowledgments

I would like to thank my supervisor, Professor Qing Hu for providing the opportunity to work with him at MIT. I have learned many research skills while working with him. His mindset of pragmatism in research has had profound impact on my academic mentality.

I am deeply grateful to Professor Mark Baldo my academic advisor, Janet Fischer and Professor Leslie Kolodziejski in the EECS Graduate Office for providing constant academic support. Undoubtedly, they were my torch in darkness during academic challenges and research frustrations.

Words fail to express my gratitude to Dr. John Reno at the Sandia National Laboratory and Professor Zbig Wasilewski at the University of Waterloo for providing excellent MBE growth. This thesis would have been impossible without their efforts. I enjoyed humor, modesty, and critical thinking of Professor Wasilewski in the last two years of my PhD. I also thank Professor Jérôme Faist at ETH for his amazing book and Professor Benjamin Williams at the UCLA, Professor Sushil Kumar at Lehigh University, and Dr. Wilt Kao at LongWave Photonics for their instructive theses. I learned a lot from you!

I enjoyed the company of my colleagues and friends Ali Shariat, Elise Uyehara, Ted Letsou, Andrew Paulsen, and Tianyi Zeng.

Last but not least, I am indebted to my family for everything.

Contents

List of Figures

List of Tables

Chapter 1

Introduction

1.1 Applications of Terahertz Technology

Terahertz (THz) radiation is loosely defined by the frequency range of 0.5 to 10 THz (1 THz=10^{12} cycles per second). The THz region of the electromagnetic spectrum has been the least developed and utilized owing to the lack of available sources. THz technology research and funding has been mainly driven by applications in astronomy, earth, and planetary science. This is mainly due to the fact that there is a vast amount of radiation from the interstellar medium (ISM), the matter between stars consists of low-density gases and dust [20] at THz frequencies. Carbon line [CII] at 1.9 THz, Oxygen line [OI] at 4.7 THz, and Nitrogen line [NII] at 1.4 THz are among the most important emission lines in ISM. Each line conveys important information to astronomers about the process of star formation and evolution.

THz spectroscopy shows great promise due to its ability to 'see' through most packaging material to probe for the presence of illicit drugs that exhibit a characteristic THz spectral fingerprint. A dominant feature of the THz spectra is the sharp absorption peaks caused by phonon modes directly related to the crystalline structure of these drugs and explosives [21, 2, 22]. Competing detection technologies such as x-rays and millimetre wave imaging lack a spectral fingerprint in their respective electromagnetic frequency ranges to identify illicit drugs. Infrared imaging has the capability to distinguish different drugs based on fingerprint spectra in the infrared

Figure 1-1: False color image of W51A taken by SOFIA. W51A is the largest massive star-forming region in Milky Way. The intense radiation pressure glow brightly at infrared wavelengths of 37 and 70 microns, shown in green and red respectively. Image is taken from [1].

region, but most packaging materials (e.g. envelopes, cardboard, etc) are opaque to probing in the infrared.

In medical applications, THz systems have been demonstrated and shown to be highly effective in cancer imaging. In particular, skin cancer is one of the most common forms of cancer in the United States. Early detection is a key for a higher survival rate and can be done by THz imaging [3]. THz wave is also used for breast cancer imaging [23], colon cancer imaging [24], brain imaging [25, 26]. THz waves not only can be used to detect cancer, but they can also be used for cancer therapy. DNA methylation is an essential epigenetic modification of DNA that regulates gene expression. Abnormal regulation of gene expression is closely related to carcinogenesis. Consequently, the assessment of DNA methylation is a key factor in cancer research. Terahertz radiation may play an important role in active demethylation for cancer therapy because the characteristic frequency of the methylated DNA exists in the terahertz region (1.7 THz) [27].

1.2 Broadband THz Sources

Broadband THz radiation can be generated by illumination of different materials with femtosecond optical pulse with a pulse duration of < 1 ps. Among those, Pho-

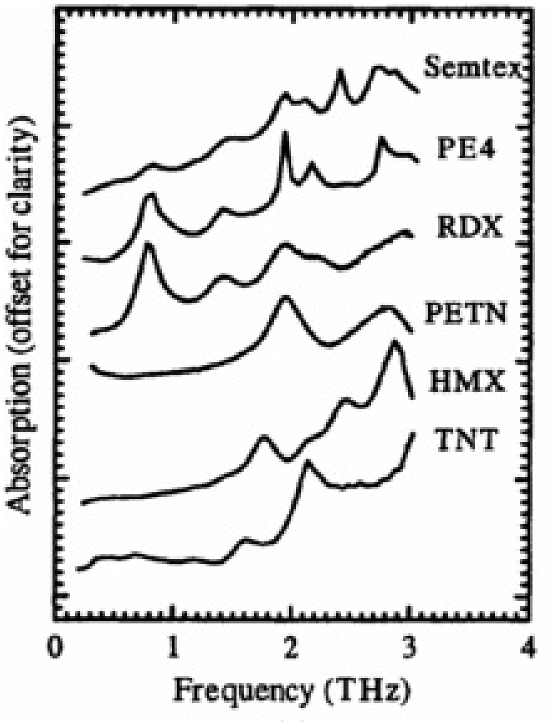

Figure 1-2: Spectral fingerprints of some common explosives. Image is taken from [2].

toconductive antenna (PCA) is one of the most promising and commonly used means of broadband terahertz generation [4]. The PCA consists of a DC biased antenna patterned on a photoconductive substrate. Optical pulse with photon energy larger than the bandgap (E_G) of the photoconductive substrate is received by the antenna and transmitted into the substrate. The generated electron–hole pairs in the photoconductive substrate is then accelerated in the DC bias field across the antenna terminals. The transient photocurrent drives the antenna and ultimately re-emits as a THz frequency pulse. An illustrative example of pulsed THz generation using PCA is shown in Figure 1-4. THz emission from photo-conductivity was first demonstrated using silicon [28]. However, the majority of current photoconductive antennas are based on GaAs or InGaAs (for telecom wavelength) due to the high carrier mobility in these materials and well-established techniques for reducing the carrier lifetime. Traditional photoconductor sources are typically generating an average power of $\approx$100 μW [29, 4]. One recent work achieved an average THz powers of 181 μW centered at 1.5 THz by placing a photoconducting switch within a resonant

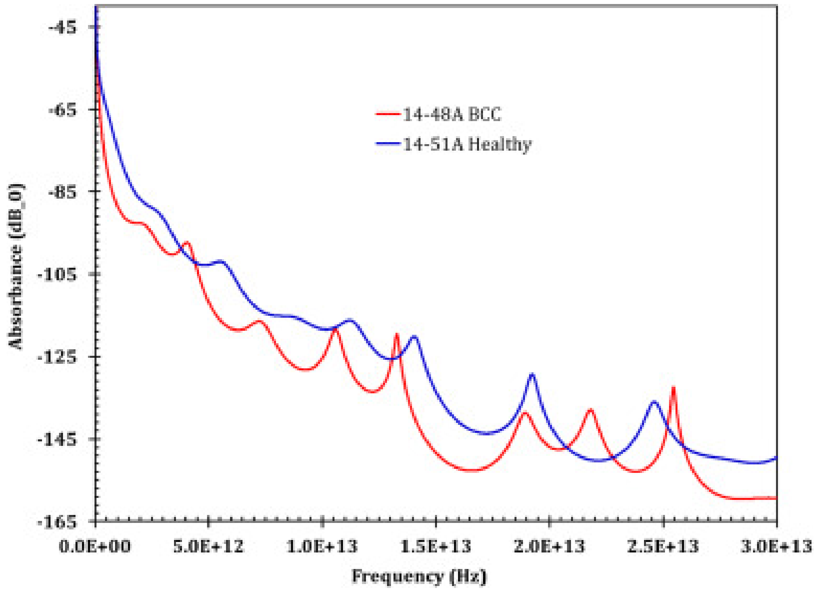

Figure 1-3: Absorbance spectra of healthy and cancerous skin samples. Image is taken from [3].

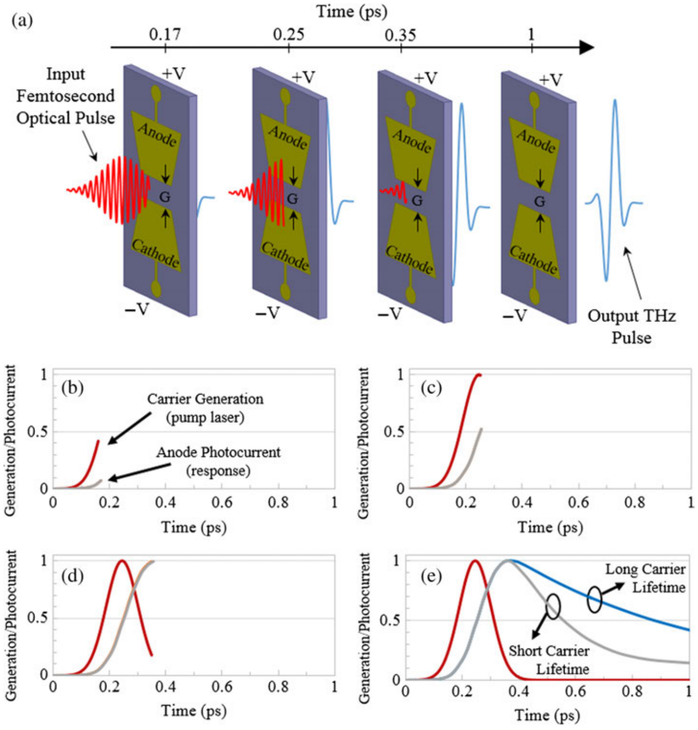

Figure 1-4: Illustrative example of pulsed THz generation in a PCA. (a) Femtosecond optical pulse propagates into the photoconductor, generates a transient photocurrent, which drives the antenna, and is re-emitted as a broadband THz pulse. (b–e) Time profile of the carrier generation (red trace) and photocurrent in the antenna gap for photoconductive material (gray trace) for short-carrier lifetime and (blue trace) for long carrier lifetime. Image and caption are taken from [4]

metal–insulator–metal cavity [30]. It has been demonstrated that incorporation of plasmonic contact electrodes can mitigate the inherent tradeoff between high quantum efficiency and ultrafast operation in conventional photoconductors. In [5], an array of 3×3 plasmonic photoconductive terahertz emitters with logarithmic spiral antennas is fabricated on a low temperature (LT) grown GaAs substrate. Pulsed terahertz radiation with high average power levels up to 1.9 mW in the 0.1–2 THz frequency range is measured at an optical pump power of 320 mW. These results were later improved and the same group demonstrated a broadband, pulsed terahertz radiation with radiation power levels as high as 3.8 mW at an optical pump power level of 240 mW over the 0.1–5-THz [31]. PCA can also achieve high conversion efficiency. Terahertz radiation powers up to 105 μW is obtained at an optical pump power of 1.4 mW, exhibiting a high optical-to-terahertz conversion efficiency of 7.5% [32]. In contrast to the widely used photoconductive materials such as GaAs and InGaAs, Ge is a nonpolar semiconductor characterized by a gapless transmission in the THz region due to absence of one-phonon absorption. Ge-based photoconductive THz emitter with a broadband spectrum extending up to 13 THz was recently demonstrated. [33]. The performance further improved to 70 THz of bandwidth using an Au-implanted Ge emitter that is compatible with mode-locked fibre lasers operating at wavelengths of 1.1 μm and 1.55 μm. [34].

Another technique to generate broadband THZ radiation is through optical rectification. Generally, optical rectification refers to the generation of a DC or low-frequency polarization when intense laser beams propagate through a crystal. The linear electro-optic effect describes a change of polarization of a crystal from an applied electric field. Optical rectification and the linear electro-optic effect occur only in crystals that are not centrosymmetric. However, optical rectification of laser light by centrosymmetric crystals is possible if the symmetry is broken by a strong electric field. Furthermore, generation and detection of THz-radiation pulses by optical rectification and the Pockels' effect require that the crystals are sufficiently transparent at THz and optical frequencies. THz radiation emission has been reported [35] from a variety of nonlinear materials such as lithium niobate (LiNbO3), lithium tan-

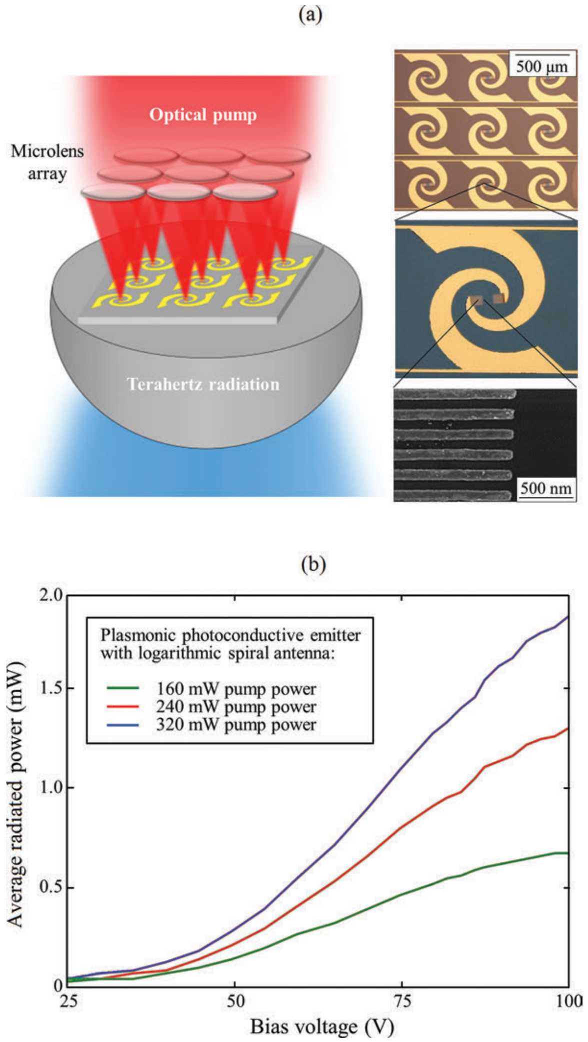

Figure 1-5: (a) Plasmonic photoconductive terahertz emitter array. A microlens splits and focuses the optical pump beam onto the active area of each plasmonic photoconductive emitter element. The emitter array is mounted on a hyper-hemispherical silicon lens through which the terahertz radiation emits. (b) Radiated power from a 3×3 plasmonic photoconductive emitter array as a function of optical pump power and bias voltage. Image and caption are taken from [5].

talate (LiTaO3), zinc telluride (ZnTe), indium phosphide (InP), gallium arsenide (GaAs), gallium selenide (GaSe), cadmium telluride (CdTe), cadmium zinc telluride (CdZnTe), and 4-dimethylamino-N-methylstilbazolium tosylate(DAST).

1.3 Narrowband THz Sources

Narrowband THz sources are crucial for high-resolution spectroscopy applications. Continuous-wave THz radiation can be achieved through up-conversion of lower-frequency microwave oscillators, such as voltage-controlled oscillators and dielectric-resonator oscillators. Up-conversion is typically achieved using a chain of planar GaAs Schottky-diode multipliers. Multiplier device fabrication techniques have been developed to enable robust implementation of monolithic circuits well into the THz frequency range [36]. Using on-chip power combined topology and extensive optimization of devices and circuits, room temperature emission at 1.03 THz with 2 mW and at 1.64 THz with 0.7 mW is recently achieved [6]. As these devices are utilizing freely moving electrons, they are limited by the transit time and parasitic RC time constants. As a result, the power level of these devices decreases rapidly as the frequency increases above 1 THz ($\frac{1}{f^4}$). Nevertheless, research is undergoing to achieve higher frequency range using multipliers. An output power of 2–14 μW at 2.49–2.72 THz is demonstrated [37].

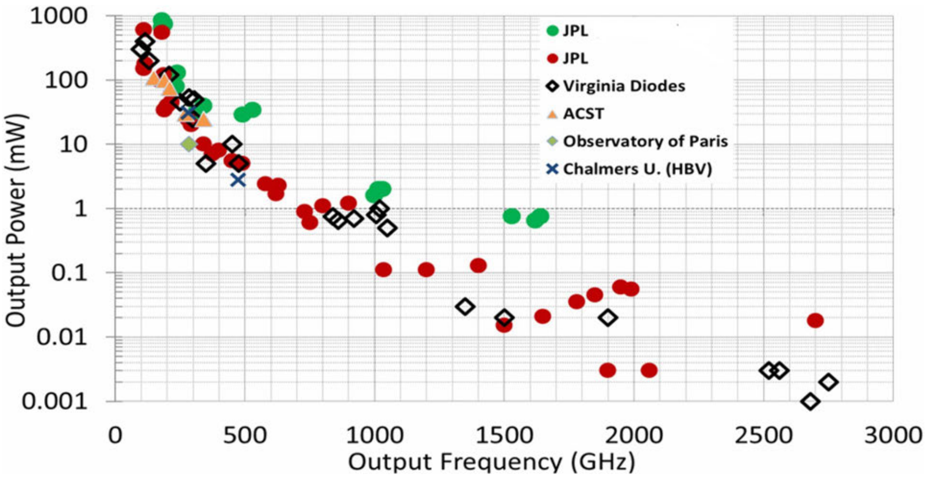

Figure 1-6: State-of-the-art frequency-multiplied sources. Image is taken from [6].

Optical down-conversion is a rich area for materials research. In non-linear photomixing, two continuous-wave lasers with slightly differing center frequencies are mixed in a material exhibiting a high second-order optical non-linearity. This results in output oscillations at the sum and difference of the laser frequencies. Such systems can be designed such that the difference term is in the THz range. Mid-infrared (mid-IR) QCL technology is now the leading semiconductor source in the mid-IR range [38]. Mid-IR-QCLs are able to not only produce high power and high efficiency but also possesses nonlinearity for THz difference-frequency generation (DFG). With a proper wavelength selection mechanism for dual mid-IR wavelength operation, a narrow-band THz emission can be intracavity generated [39, 40, 41]. Therefore, this type of terahertz source inherits the advantage of the mid-IR QCLs, such as room temperature operation, electrical pumping, compact size, as well as potential for mass production. High THz power up to 1.9 mW in pulse mode and 14 μW for continuous wave operations at room temperature is demonstrated [7, 42].

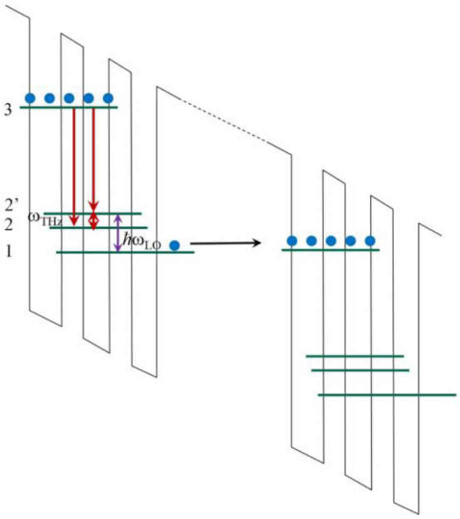

Figure 1-7: Schematic of the DFG process between the electron states in a band structure of quantum cascade laser. Image is taken from [7].

The invention of THz QCLs [8] held great promise to bridge the so-called “THz gap” between semiconductor electronic and photonic devices. As a fundamental oscillator, THz QCLs can generate much greater output power levels (>1 W) [43] and as will be demonstrated in chapter 2 can achieve much greater C.W power efficiencies (>1%) [44]. Furthermore, broadband THz-QCL gain media can be developed into other devices such as THz laser frequency combs [45, 46]and radiation amplifiers [47]. However, the demanding cooling requirements for THz QCLs have been a showstopper for achieving compact and portable systems, and they have confined THz QCL systems to a laboratory environment. Therefore, raising the maximum operating temperature $T_{\max}$ to above that of a compact cooler (>235 K for single-stage thermoelectric coolers), or even no cooler at all, has been a paramount long-term goal in the field.

1.4 Continuous Wave Operation Using Photonic Wire Laser

Figure 1-8 shows the schematic of a QCL with a metal-metal waveguide. In this scheme, multiple quantum wells and barriers are sandwiched between multiple layers of metals. In THz QCL, metal-metal (M-M) cavity has been developed to achieve higher mode confinement and lower waveguide loss [48, 11, 12]. These two properties are necessary to reduce the threshold gain and achieve higher temperature performance. In a THz QCL, the required Molecular Beam Epitaxy (MBE) growth limits the active medium thickness to $\approx 10\mu m << \lambda \approx 100\mu m$ [49]. In addition, for proper alignment of the lasing levels in a THz QCL with a phonon depopulation scheme [12], the voltage drop per module should be greater than the sum of longitudinal optical phonon energy in GaAs ($E_{LO} \approx 36\,\mathrm{meV}$) and emitted photon energy $\approx 14\,\mathrm{meV}$. Therefore, the biasing voltage per module is $\geq\ 50\,\mathrm{mV}$. As a result, in a typical THz QCL with ≈ 200 modules the biasing voltage is typically $\geq 10\,\mathrm{V}$ across the device. On the other hand, the maximum current density ($J_{\max}$) of a THz QCL is $\approx 1000\ \frac{\mathrm{A}}{\mathrm{cm}^2}$. As a result, even a millimeter long FP device with 30 μm of width can dissipate $\approx 5\,W$. To achieve stable continuous wave (C.W) performance, heat dissipation needs to be minimized. This is mostly done by reducing the waveguide width ($<< \lambda$), which also minimizes the impact of higher order lateral modes. However, in a FP laser,

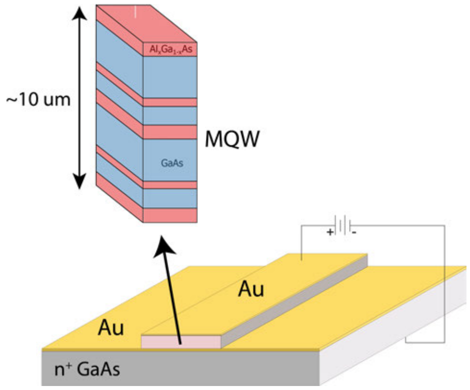

Figure 1-8: Schematic of a QCL with Metal-Metal waveguide.

sub-wavelength transverse dimension, as well as interference from the front and back facets produces divergent beam pattern with rapidly changing phase front [50]. Such small transverse dimensions compared to the wavelength places the THz QCL lasers in a broader theme often called photonic wire lasers [51, 52, 53, 54, 55]. Photonic wire lasers are characterized as w « λ (where w is the dimension of the cross-section and λ is the wavelength). In such lasers, individual sources in the laser medium emit coherently with their phases determined by the cavity modes. Consequently, each laser mode can be thought of as a continuous phased array [56]. In addition, in wire lasers a large fraction of the cavity modes propagates outside of the deep sub-wavelength core. Therefore, the radiation properties of a wire laser can be efficiently manipulated by perturbing its lateral boundary condition, both electrically and geometrically. This unique feature was utilized in a tunable laser whose frequency can be changed by moving an object placed alongside of the wire laser [57]. In THz QCL with M-M waveguides, Distributed FeedBack (DFB) grating with various $\frac{w}{\lambda} << 1$ (w is the width of waveguide) are commonly used to achieve mode selectivity, improved radiation efficiency, and enhanced beam quality.

First-order edge-emitting DFB lasers can produce single-mode emission. However, the problem of divergent radiation pattern remains and the out coupling of the optical power is still low (so as efficiency) [58]. However, C.W performance is achievable for narrow ridges ($w < 30\mu m$). Second order DFB cavity enables surface coupling of single-mode radiation. However, surface emission from a M-M waveguide is inherently difficult, as the light must be emitted from a metallic surface patterned with only sub wavelength structures [59]. As the polarization of the emitted light is transverse to the light generated from the intersubband transition in THz QCL active medium, these cavities are inherently inefficient as they possess low modal overlap. In contrast to more optimized surface emitting DFB lasers [60, 61, 62, 43, 63], edge-emitting structures with narrow cavity widths are potentially more suited for applications in sensing, spectroscopy, and metrology due to the lower electrical power dissipation, which better enables continuous-wave operation. [64, 65]. This is mainly due to the fact that the radiation originates from the same polarization generated by intersubband transition within the active medium. In-plane emitting wire lasers using 3rd-order DFB gratings [66, 67, 68, 69], and including integrated microstrip-antennas [70] are the most exploited solutions since their dimensions can be scaled down without compromising the beam quality. Specially, Antenna coupled third order DFB (ADFB) [70] is overcoming the limitations in controlling the beam quality and radiation efficiency as compared to earlier designs [66] and has achieved record high efficiencies. Due to the flexibility in controlling the effective mode index and higher efficiency, ADFBs are used as a platform to achieve more efficient and versatile sources for THz radiation in this thesis.

1.5 Thesis Structure

Unidirectional emission from an antenna coupled 3rd-order DFB is highly desirable as such emission pattern will yield a nearly factor-of-two increase in the output power with the same heat dissipation. Such increase in the absolute power is important for direct bolometric imaging [64]. In chapter 2, we propose a simple, yet effective technique to achieve unidirectionality based on ADFBs. Unidirectionality is achieved with a power ratio of the forward/backward $\approx$ 8, and the power of the forward-emitting laser is increased by a factor of 1.8 compared to a reference bidirectional DFB laser. Furthermore, we have achieved the record high CW power wall plug efficiency of $\approx$1%.

Thus far, no scheme has been devised to simultaneously achieve good beam quality, high CW output power, and continious frequency tunability from wire lasers in THz. Because of all the advantages of ADFBs, achieving such performance metrics on this platform will open doors to new applications in imaging and astronomy in which continuous frequency tunability, high C.W output power, and high beam quality is essential [71, 72]. In chapter 3, we propose and demonstrate a new scheme to form ADFB arrays. Inspired by the chemistry of hybridization, our scheme phase locks multiple ADFBs through lateral near field coupling. With the coupled-cavity laser, we have demonstrated several performance metrics that are important for various applications in sensing and imaging: 1) a continuous electrical tuning of $\approx$10 GHz at $\approx$ 3.8 THz (fractional tuning of 0.26%), 2) a good level of output power ($\approx$50-90 mW of continuous-wave power), and 3) tight beam patterns ($\approx 10^\circ$ of beam divergence). Achieving all three metrics simultaneously is the main contribution presented in this chapter.

Recent development in QCL technology has enabled NASA to initiate the Galactic/Extragalactic ULDB Spectroscopic Terahertz Observatory (GUSTO) [71] that will measure emissions from the interstellar medium. Measurement of neutral oxygen line (OI at 4.744 THz), which will provide important information on star formation, is at the heart of this mission. In chapter 4, we describe the design procedure and fabrication details of local oscillator for GUSTO.

The final and technologically more impacting contribution of this thesis is presented in chapter 5. The high power portable THz laser system developed in this chapter is enabled by a record setting of $T_{\text{max}} = 250$ K, far exceeding the current record of 210 K which was established in 2019 [16]. This record was only a marginal increase from a 7-year old record of 200 K [15]. This significant improvement in T_{max} is achieved based on a novel and unique design strategy to achieve a clean 3-level system in the THz QCL structure, and the strategy is rooted in fundamental laser physics. To further emphasize the significant challenges and advances of this work, historical record of T_{max} of THz QCLs over time is plotted in Figure 1-9. It is clear from Figure 1-9 that after the initial fast rise of T_{max} in the early years (2002-2003),

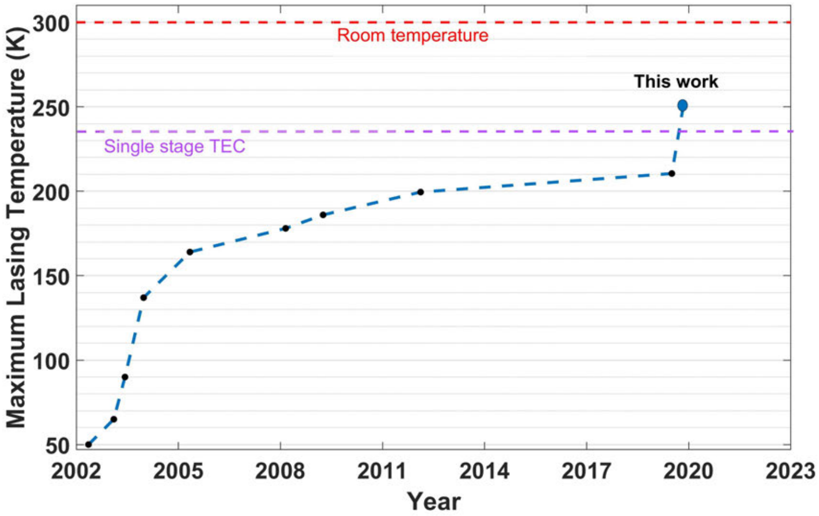

Figure 1-9: Experimentally achieved T_{max} for THZ QCL over time. The temperature of a single-stage thermoelectric cooler ($\approx$ 235 K) and room temperature of 300 K are also marked as reference. The dashed line is for visual guidance.
Data are taken in order from [8, 9, 10, 11, 12, 13, 14, 15, 16].

the progress slowed down and then even stalled after 2012 at 200 K until 2019. This long stretch of lack of progress has prompted many observers to speculate that there is a fundamental physical limit that THz QCLs cannot be operated significantly above 200 K. Our work definitively showed that there is no such limit, and the result should jolt the field and give the THz community the optimism that high-temperature (even at and above room-temperature) operation of THz QCLs can be achieved.

Chapter 2

Unidirectional Photonic Wire Laser

2.1 Introduction

Unidirectional emission from wire lasers is highly desirable since most of the laser power will be in the desired direction. In conventional Fabry-Perot (FP) laser devices, the unidirectional scheme can be easily implemented by the use of high-reflectivity (HR) coating or Distributed Bragg Reflector (DBR) attached to the rear facet. However, in wire lasers mode mostly propagates outside of the solid core due to their small lateral dimension relative to the wavelength. Therefore, from equivalence of displacement current and conduction current in the generation of electromagnetic waves, the electric field outside and along the solid core forms a distributed emitter [56]. If the emission from this distributed emitter dominates that from the facet, then HR coating of the rear facet will have a negligible effect on blocking the backward radiation, resulting in a bidirectional emission pattern even with a HR coating. Therefore, conventional approaches of attaching a highly reflective element to the rear facet, whether a thin film or a DBR, is not effective. Here we demonstrate a novel scheme to achieve unidirectional emission from linear distributed feedback (DFB) lasers. This scheme is inspired by Yagi-Uda antenna in microwave [73]. Here by strategically placing monolithic reflectors relative to the DFB grating, we can substantially enhance the wave in the forward direction and suppress the wave in the backward direction.

2.2 Third Order DFB

Figure 2-1a shows a schematic of a generic 1-D cavity made of GaAs. In this schematic, the black lines at the top and the bottom represent materials (including metals) that confine the wave within the cavity. Here, the only out-coupling and the feedback withing the cavity exist at the end facts (resembling Fabry-Perot cavity). It is shown [66] that by introducing deep air gap inside the cavity, out-coupling and feedback within the cavity with n≈ 3.6(GaAs index in THz) can be achieved. As illustrated in Figure 2-1b, every other crest/trough of the mode inside the cavity couples to a crest/trough of the propagating mode in the free space which results in $n_{\text{eff}} = 3$. Another useful picture to have is to consider a third order DFB as an array of short Fabry-Perot (FP) cavities which are phase locked. In this picture, individual micro-cavities radiate into the free space (similar to open end metallic waveguides in microwave) from their corresponding facets and are coupled to adjacent cavities through the strong coupling at the facets.

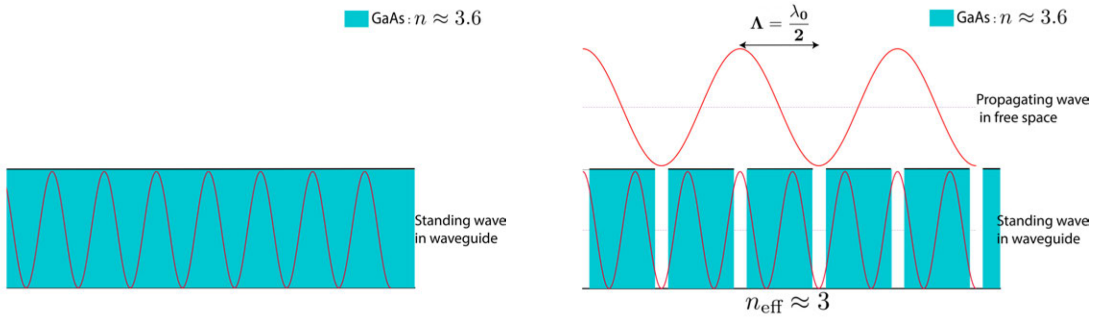

(a) (b)

Figure 2-1: A simple representative model for a third order DFB. (a) no out-coupling except at the facets. (b) introducing periodic out-coupling slots.

2.3 Phased Array Antenna Model For Third-Order DFB Lasers

A 3-D simulation of a 3rd-order DFB structure can be performed using quasi-eigen mode solver of commercially available Electromagnetic (EM) simulators. Figure 2-2 shows the computed mode distribution and the corresponding bidirectional radiation pattern for a third order DFB laser using COMSOL METAPHYSICS package. A

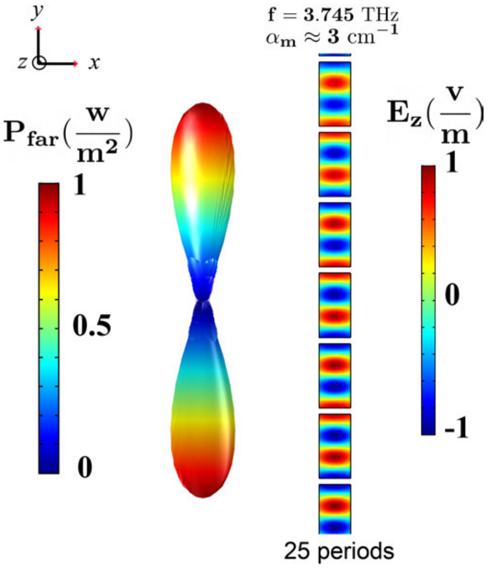

Figure 2-2: Distribution of E_z of a 3rd-order DFB laser for the desired mode and the corresponding far field radiation pattern. The waveguide width is 18 μm and the periodicity is 40 μm. The height of the waveguide (along z) is 10 μm.

.

perfectly phase matched 3rd-order DFB laser can be modeled as an array of evenly distributed radiators with π phase difference between adjacent radiators [67, 68]. A simple 1-D model for this phased antenna array is shown in Figure 2-3. It is well-known that the radiation field of a linear antenna array is the product of the array factor (AF) and the element factor (EF). AF is a function of the positions of the antennas in the array and the weights. EF is the radiation pattern of individual elements in the presence of all other elements (in the case of interacting elements). It can be shown [74] that the array factor for a uniform amplitude 1-D antenna array is:

$$|AF|^2 = \left| \frac{1}{N} \frac{\sin\left(\dfrac{N\Psi}{2}\right)}{\sin\left(\dfrac{\Psi}{2}\right)} \right|^2 \tag{2.1}$$

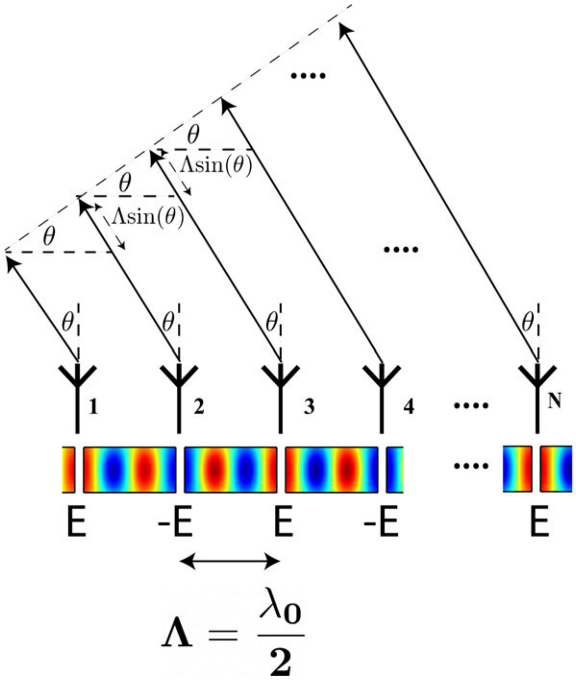

Figure 2-3: Phased array antenna model for a perfectly phase matched 3rd-order DFB with N elements.

Here N is the number of elements (periods) and ψ is defined as:

$$\Psi = 2\pi\frac{\Lambda}{\lambda_0}\sin(\theta) + \pi \tag{2.2}$$

In a perfectly phase matched 3rd-order DFB laser, the periodicity is $\frac{\lambda_0}{2}$, where λ_0 is the free-space radiation wavelength of the laser. This simplifies equation 2.2 as:

$$\Psi = \pi sin(\theta) + \pi \tag{2.3}$$

Computed $|AF|^2$ for different number of periods in a perfectly phased match 3rd-order DFB is shown in Figure 2-4. A tighter beam can be achieved with more elements within the array provided the phase matching condition is met. For a 3rd-order DFB, a figure of merit for phase matching condition is defined as:

$$n_{eff} = 3\frac{2\Lambda}{\lambda_0} \tag{2.4}$$

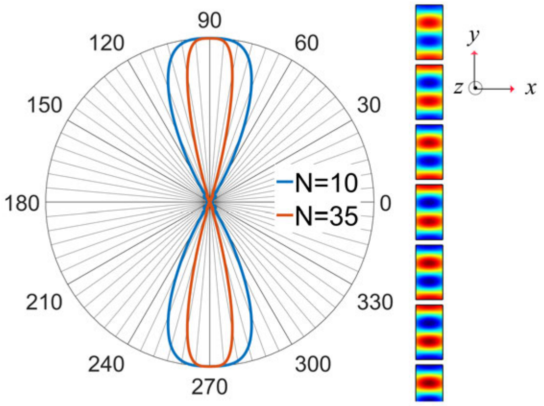

Figure 2-4: Computed $|AF|^2$ for a 3rd-order DFB with 10 and 35 elements.

in a perfectly phase matched 3rd-order DFB, $n_{eff} = 3$. Deviation from this optimum value results in accumulated phase mismatch along the array and degrades the beam quality for longer arrays.

2.4 Third-Order DFB With Asymmetric EF

As shown in section 2.3, the periodicity of the DFB structure enforces the symmetry of AF. Thus, the only way to achieve asymmetric emission from a 3rd-order DFB is to design and implement a highly asymmetric EF to "skew" the bidirectional element factor into unidirectional. Here we explicitly take advantage of a unique feature of photonic wire lasers, that a large portion of the mode propagates outside of the solid core and the radiation from each aperture is highly divergent. Therefore, a reflector placed close to the solid core can reflect a large fraction of the lasing mode propagating outside of the solid core. Unidirectionality can be achieved by placing this reflector at an asymmetric point but close to a node of electric field inside the cavity. This idea is shown in Figure 2-5a. Placing the reflectors close to a node results in minimum disturbance of the desired mode distribution. Therefore, the radiation loss of the desired 3^{rd} order mode will not be significantly impacted. In this scheme, the element factor is the field of a single aperture in the presence of all the passive reflectors. However, the reflector positions are periodic and the impact of adjacent reflectors are amplified by the rest of reflectors. Therefore, for a qualitative under-

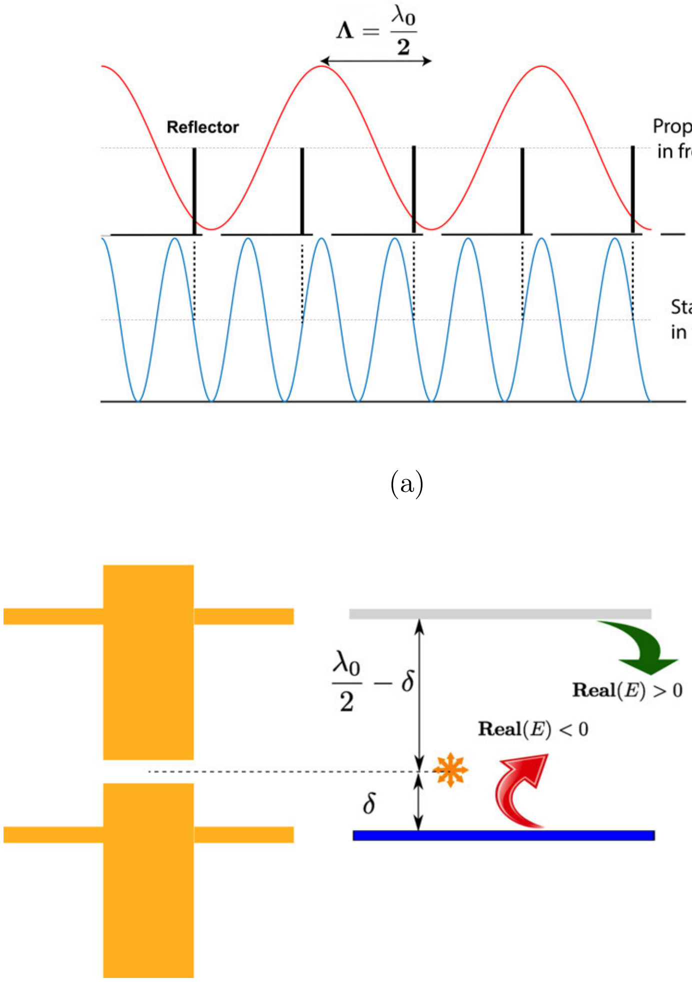

(a)

(b)

Figure 2-5: A simple illustrative model for a 3rd-order DFB with an asymmetric EF.

standing, only the impact of the closest reflectors to EF need to be considered. This simple picture is illustrated in Figure 2-5b. Qualitatively, the aperture of a 3rd- order DFB structure can be approximated as an omnidirectional source with a highly divergent beam pattern, emitting symmetrically in both forward and backward directions. The radiation pattern is similar to the radiation from a short Fabry-Perot cavity with sub wavelength dimensions, which is very divergent. The reflector at the distance of δ from the aperture, where $\delta < \frac{\lambda_0}{8}$ reflects the aperture field in a way that destructively interferes with the backward radiation, causing preferential radiation in the forward direction. More quantitatively, the coefficient of field reflection from vacuum to dielectric is $r = \frac{1-n}{1+n}$ for a TE plane wave, and $r < 0$ causing a 180° phase shift at the interface. The additional phase shift, from a round-trip traveling with a distance of $\delta < \frac{\lambda_0}{8} <$ is $< 90°$ resulting in a total phase shift of $180° - 270°$ between the reflected wave and the backward radiation from the aperture, yielding a destructive interference. Not obvious, but there is also a constructive interference in forward direction due to double reflections from the closest reflectors to the aperture (double negative reflection coefficient leads to a positive coefficient and extra wavelength produces 2π phase shift). The overall mechanism in our simple model is shown in Figure 2-5b. It is important to notice that unidirectionality ratio increases with the number of periods in the array. This is because all the reflectors are separated with the distance of $\frac{\lambda_0}{2}$. Therefore, the round trip phase delay for the reflection from each reflector is 2π. Hence, the impact of adjacent reflectors shown in Figure 2-5b is repeated periodically along the array for the radiation from each gap. This is qualitatively shown in Figure 2-6. It is important to notice, this simple model does not include the radiation from sidewalls of a third order DFB. In a more realistic picture, the reflectors also reflect the wave which exist outside the solid core along the ridges. Based on this qualitative understanding, 3-D full-wave finite element (FEM) quasi-eigen modes simulations were performed (using COMSOL) to explore the optimized reflector position and length. The simulation is performed on a 25-elements 3rd-order DFB with the parameters shown in Figure 2-7. For this simulation, the simulated optimum value is $\delta = 3\ \mu m < \frac{\lambda_0}{8} \approx 10\ \mu m$. Though the simple structure presented

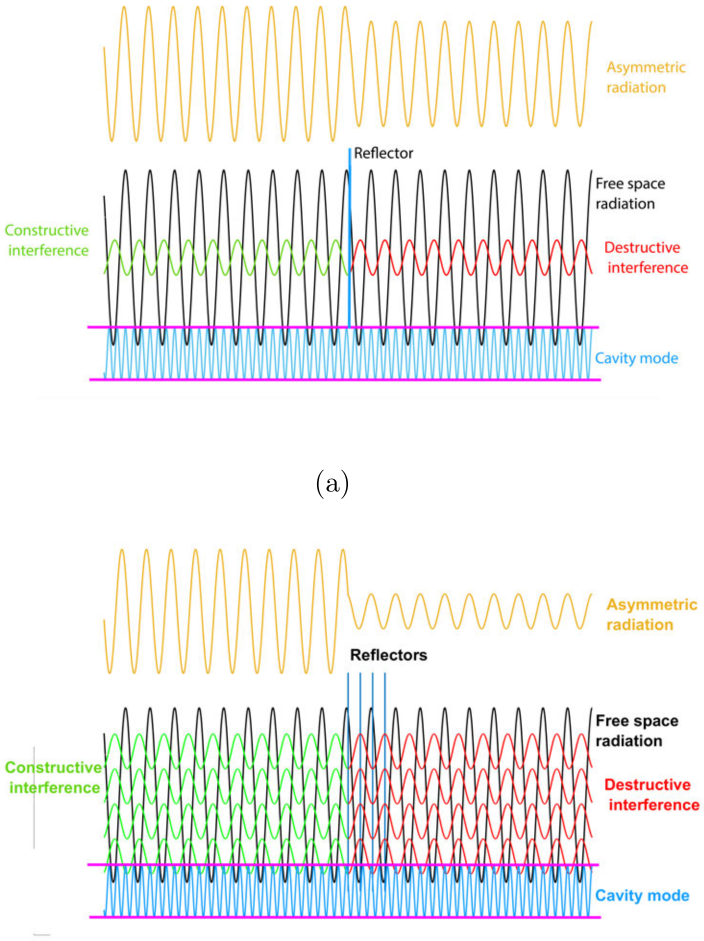

(a)

(b)

Figure 2-6: A simple illustrative model for a 3rd-order DFB with an asymmetric EF. (a) interference with one reflector (b) amplified interference by multiple reflectors.

above produces the favorable asymmetry in the radiation field, it has multiple issues that limits its feasibility. One disadvantage of this scheme is that the mirror loss and the asymmetry ratio are simultaneously depending on the reflector position. As shown in Figure 2-7, the optimum reflector position for achieving the optimum unidirectionality has higher than optimum mirror loss $\alpha_m^{\text{opt}} = \alpha_w \approx 15 - 18\ cm^{-1}$. Ideally, the unidirectionality ratio and the mirror loss should be adjusted independent of each other. The dependence of radiation loss to reflector position is due to the fact that when the reflector is closer to the radiating aperture (crest/trough of the field), it is closer to the field maximum/minimum inside the cavity. This in turn produces more disturbance to the desired mode (out-coupling at discontinuity) and results in a higher radiation loss. At the positions closer to the node, there are two competing effects. One, the reflector introduces extra reflection inside the cavity. Therefore, the radiation loss is reduced. Second, radiation loss will be increased due to the extra out coupling at the discontinuity caused by the reflectors. The overall impact need to be simulated. The other disadvantage of this scheme is the required electrical biasing of individual micro-cavities. This scheme requires bonding pads located in the sideways and connected through fins to the micro-cavities which complicates the fabrication process.

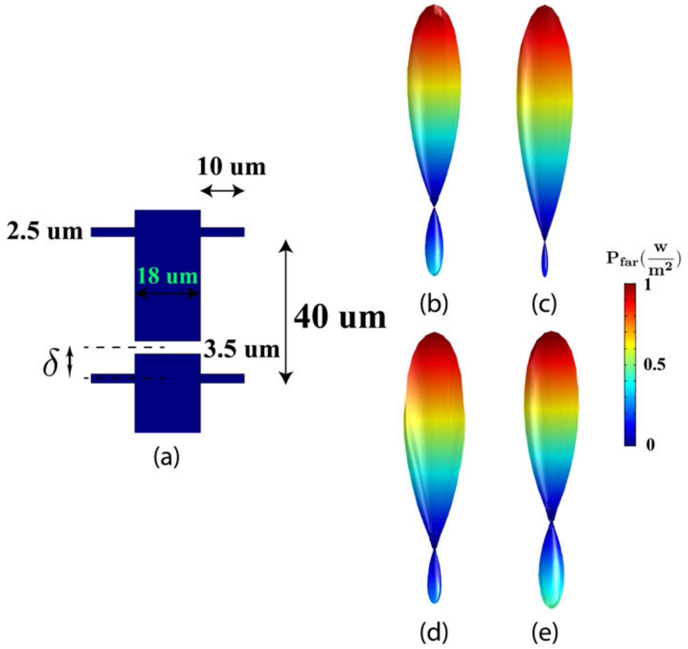

Figure 2-7: Simulation of a third order DFB with asymmetric EF. (a) geometrical parameters for a simulated asymmetric 3rd-order DFB,(b-d) far field radiation pattern of asymmetric 3rd-order DFB with (b) $\alpha_m = 48\ cm^{-1}, \delta = 3\ \mu m$ (c) $\alpha_m = 30\ cm^{-1}, \delta = 4.5\ \mu m$ (d) $\alpha_m = 21\ cm^{-1}, \delta = 5.5\ \mu m$ (e) $\alpha_m = 14\ cm^{-1}, \delta = 6.5\ \mu m$. Here δ is the distance from the center of reflector to the center of radiation gap.

2.5 Unidirectional Antenna Coupled Third Order DFB

To overcome the limitations mentioned in the previous section, we implemented the asymmetric element factor to an already well-established Antenna Coupled 3rd-Order

DFB (ADFB) grating laser [70]. A simulated mode profile and beam pattern of a ADFB grating is shown in Figure 2-8. The difference between an ADFB and a DFB is the integration of antenna loop around the radiation aperture. A 3-rd order DFB can be thought of as an array of phase locked micro cavities. The mirror loss of this array is related to the coupling between the individual cavities and edge emitting radiation from each micro cavity. The antenna loop increases the effective surface area for the edge emitting micro cavities. This is similar to increasing the radiation resistance of a point source radiator by transforming it to a dipole antenna [73]. Such increase in effective surface area increases the mirror loss of a ADFB as compared to a DFB. Antenna loop also has the advantage of tuning the resonance frequency. This is because only the antenna loop length which produces 2π phase shift across the radiation gap provides the minimum perturbation to the corresponding mode distribution. Consequently, by adjusting the antenna loop length, the mode distribution will be re-adjusted for the new boundary condition presented across the loop. This changes the mode distribution mainly in the longitudinal direction. Since in a cavity, $k_t^2 + k_l^2 = (\frac{w}{nc})^2$ (l and t represent longitudinal and transverse directions), such change in k_l will change the lasing frequency. This is called resonance condition and is shown in Figure 2-8d. This scheme can produce high mirror loss and radiate in the same polarization, which is generated by the intersubbnat transition in quantum well structures. Hence, a high wall plug efficiency (WPE =output power/input power) in C.W operation can be achieved. A WPE of 0.57% and single-mode operation is already demonstrated based on ADFB. There are three distinct advantages of using ADFB scheme when the monolithic reflectors are used. First, in ADFB, the extension of the radiation field from the gap into the antenna arm increases the "visibility" of reflectors. Therefore, one degree of freedom is introduced to optimize unidirectionality ratio by adjusting antenna loop length. Second, the radiation loss can be adjusted by antenna loop for a particular design. Third, for a constant position of reflectors, its ratio with respect to wavelength, which control the unidirectionality ratio, can be fine tuned by changing the length of antenna loop. The schematic and the computed overall emission beam pattern of an optimized ADFB with reflectors are shown in

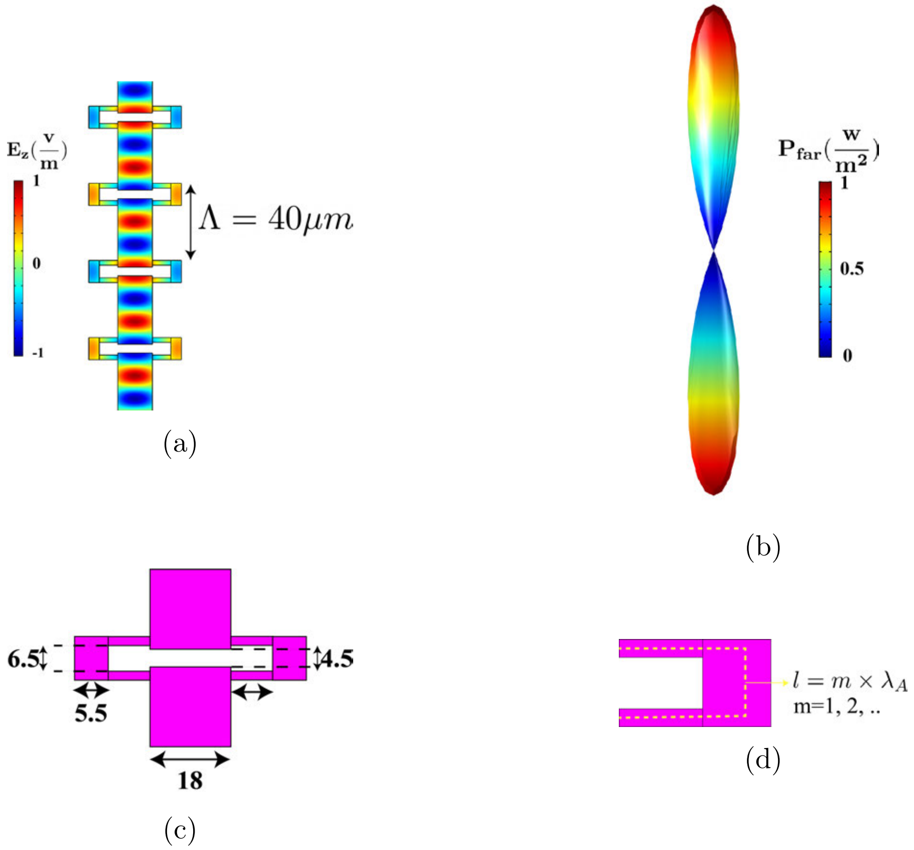

Figure 2-8: Full wave simulation for a 35-period ADFB. (a) distribution of E_z (normal to page) of a 3rd-order DFB laser for the desired mode. (b) far field radiation pattern. (c) schematic of the optimized ADFB. All dimensions are in μm.(d) resonance condition for antenna loop. Here λ_A is the wavelength inside the antenna loop and l is the circumference of the dashed line.

Figure 2-9. In the numerical simulation, we have found that the reflector length is not a sensitive design parameter but should be longer than the length of the aperture antenna to be effective as the size of the reflectors affects the constructive interference in forward direction. The length of 26 μm was chosen based on optimization algorithms in conjunction with full-wave simulation. It is worth mentioning that the top metal layer on the reflectors has small but positive impact on the unidirectionality. This is because the electric field is largely normal to the metal strip producing negligible surface current. Considering the antenna loop and the reflectors, the resemblance of overall structure to a Yagi-Uda antenna shown in Figure 2-10 is canny.

As it is shown in Figure 2-5, the relative position of reflectors with respect to radia-

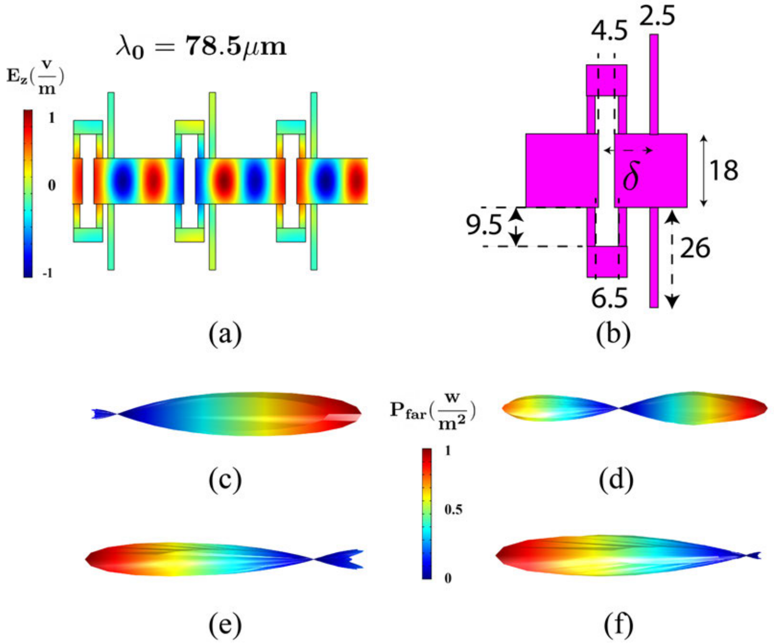

Figure 2-9: Simulation of a unidirectional ADFB. (a) distribution of E_z (normal to page) of a 3rd-order DFB laser, (b) geometrical parameters for a simulated asymmetric 3rd-order,(c-f) far field radiation pattern of a unidirectional 3rd-order DFB with (c) $\alpha_m = 12\ cm^{-1}$, $\frac{\delta}{\lambda_0}$=0.1146 (d) $\alpha_m = 12\ cm^{-1}$, $\frac{\delta}{\lambda_0}$=0.1242 (e) $\alpha_m = 14\ cm^{-1}$, $\frac{\delta}{\lambda_0}$=0.1338 (f) $\alpha_m = 23\ cm^{-1}$,$\frac{\delta}{\lambda_0}$=0.1465. All dimensions are in μm. The periodicity is 40 μm.

Figure 2-10: a Yagi-Uda (more correctly Uda-Yagi antenna) with three directors and one reflector. The director elements produce destructive interference in minor lobe direction.

tion wavelength ($\frac{\delta}{\lambda_0}$) has great impact on the unidirectionality ratio. However, in an ADFB, the radiation field is extended into the antenna loop arms. The distribution of field across this antenna loop closely resemble a $\frac{\lambda}{2}$ dipole antenna. The reflection of this distributed field from a finite length reflectors requires full-wave simulations and the simple model presented in 2-5b is inadequate. Nevertheless, using the simple model presented in Figure 2-5, one expects that the beam pattern flips its direction if $\frac{\delta}{\lambda_0} > \frac{1}{8}$. To illustrate this, simulation of a ADFB with different values of δ is shown in Figure 2-9. As it is shown, unidirectional beam pattern in different directions can be achieved with different values of $\frac{\delta}{\lambda_0}$. However, as illustrated in Figure 2-9f, for greater values of $\frac{\delta}{\lambda_0}$, the reflector position is closer to a crest/ trough within the cavity (shown in Figure 2-5a). This in return increases the radiation loss for the desired third order mode.

Following the simulations results in Figure 2-9, $\frac{\delta}{\lambda_0}$=0.1146 is selected for the reflector position with an estimation $\alpha_m = 12\ cm^{-1}$. However, to fine tune the $\frac{\delta}{\lambda_0}$, we place the reflectors at a constant δ and we adjust the radiation wavelength through the change in antenna loop. The change of the antenna loop also directly impact the unidirectionality ratio due to the finite size of this structures and complicated wave scattering processes. To experimentally demonstrate this idea, several arrays of DFB triplets from this design are fabricated to verify the unidirectionality in the radiation pattern. Each triplet is consisting of a DFB with reflector placed optimally to radiate in the desired direction (front radiator), a DFB with reflector which is flipped 180° compared to the one which radiate in front direction (back radiator), and a reference DFB without reflector which should have a symmetric bidirectional radiation pattern. The short distance among those three lasers ($\approx 150\mu m$) minimizes variation in device performances due to fluctuation in fabrications. The antenna loop arm length varies from one triplet to another to achieve optimum phase matching and unidirectionaliy ratio. The biasing current is provided to the laser array through a large bonding pad on top of a thin (2500 A°) layer of silicon nitride as an isolation layer. The array is gold wire bonded to an electronic chip enabling us to electronically switch the bias among the triplets to provide the same measuring environment. The fabrication and measurement strategy is shown in Figure2-11. The pulsed I-V and L-I curves for DFB triplet with antenna length of 9.5 μm are shown in the Figure 2-12. The spectra measurement shows single-mode emission for the triplet around 3.83 THz which was very close to simulated frequency of 3.82 THz. Similar lasing frequency (within 4 GHz) and I-V characteristics confirm that fabrication fluctuation is negligible from one DFB laser to another. The lasing threshold current densities for the three lasers are also approximately the same, indicating all the three structures have similar radiation (mirror) loss. Clearly, the structure designed for forward emission delivered much higher power (by a factor of ≈ 8) than that from a backward structure, showing a clear unidirectional radiation pattern. Furthermore, compared to the reference of a bidirectional DFB, a factor of 1.8 increase in the output power from the unidirectional laser is obtained, validating the advantage of unidirectionality which is the original motivation of this work. It is worth mentioning that a quick calculation can verify the consistency of these results,assuming that the mirror loss is the same for all the three structures. If the asymmetry ratio in power is 2m (here m =4), the enhanced power of a unidirectional DFB laser as compared to a bidirectional DFB laser should be $\frac{4m}{2m+1} = 1.78$ which is close to what we have measured. The measured WPE is 0.87 % which is a good improvement over the 0.57 % reported in [70, 68]. It is well known that power from a laser is proportional to $\frac{\alpha_m}{\alpha_m+\alpha_w}$ in which α_m is the mirror (radiation) loss and α_w is the waveguide loss [75]. The lasing threshold of the lasers is proportional to $\frac{\alpha_m+\alpha_w}{\Gamma}$ in which Γ is the mode confinement factor. For maximum output without a significant increase of the laser threshold, $\alpha_m = \alpha_w$. Through 3-D full wave simulations, we have noticed that adding reflector to the ADFB may decreases(depends on reflector position) the mirror loss slightly (by 1-2 cm^{-1})as the reflectors increase the feedback which reduces the radiation loss. Consequently, the parameters for the optimum design of antenna-coupled 3rd-order ADFB without reflector are not the same as the optimum design for unidirectional ADFB. In order to make a fair comparison of the relative performance, we further increase the mirror loss for unidirectional ADFBs (and increasing WPE) by aiming for $\alpha_m = 15cm^{-1}$ which is the measured waveguide loss α_w in a similar structure [76]. The schematic of

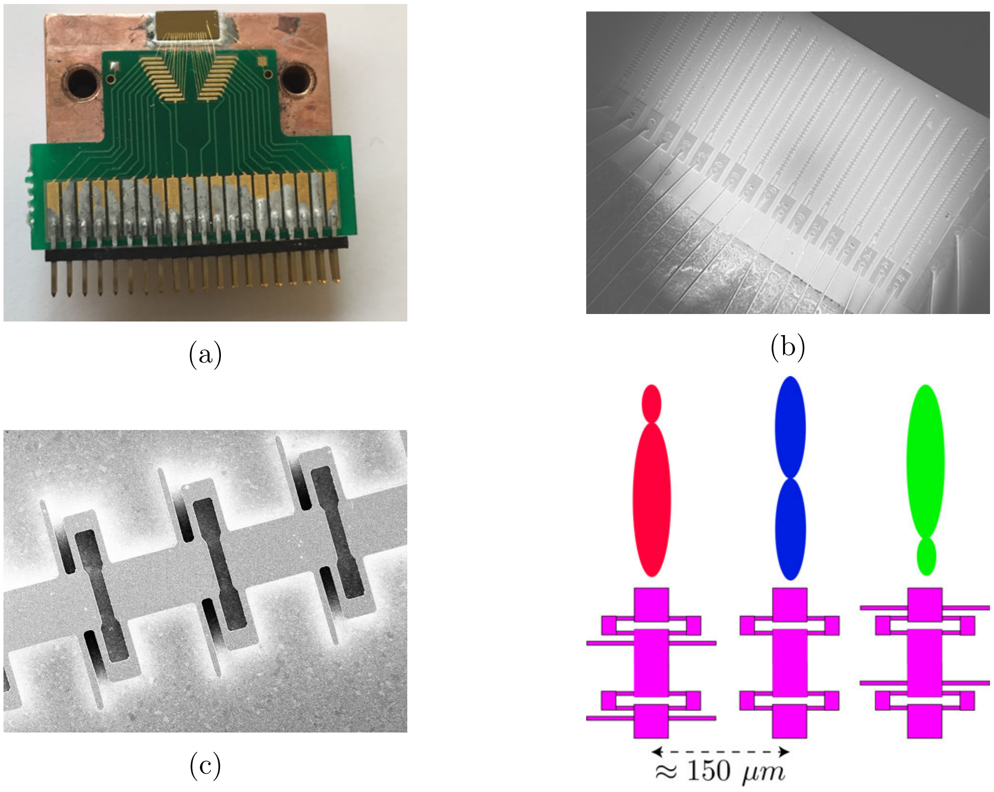

(a)

(b)

(c)

(d)

Figure 2-11: Fabrication and measurement strategy (a) array of 3rd-order DFB lasers gold wire bonded to an electronic chip for nearly simultaneous measurement. (b) photos of fabricated array of DFB triplets. (c) SEM of a DFB device showing three periods. (d) simulated distribution of Ez (normal to page) and the corresponding far field radiation pattern.

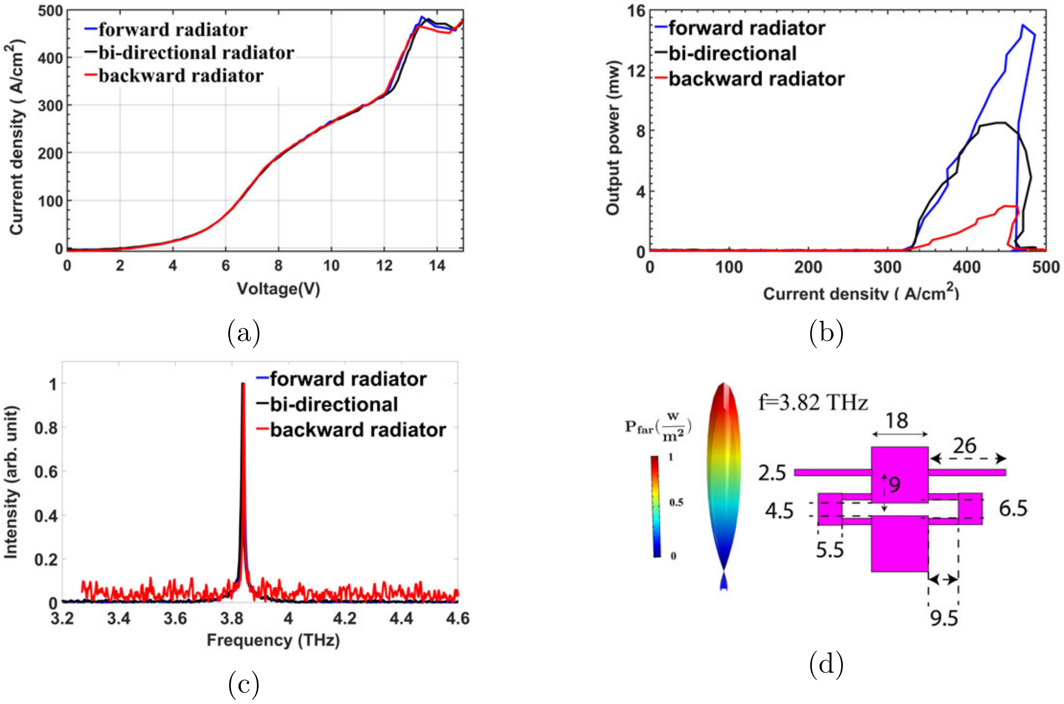

(a)

(b)

(c)

(d)

Figure 2-12: Measurement results for uni-directional 3rd-order DFB (a) V-I measurement for the triplet with antenna length of 9.5 μm (b) L-I measurement, (c) frequency spectra of the lasers. The difference in the lasing frequencies is within the instrumental resolution of 3.75 GHz of FTIR.(d) the schematic of optimum design. All dimensions are in μm

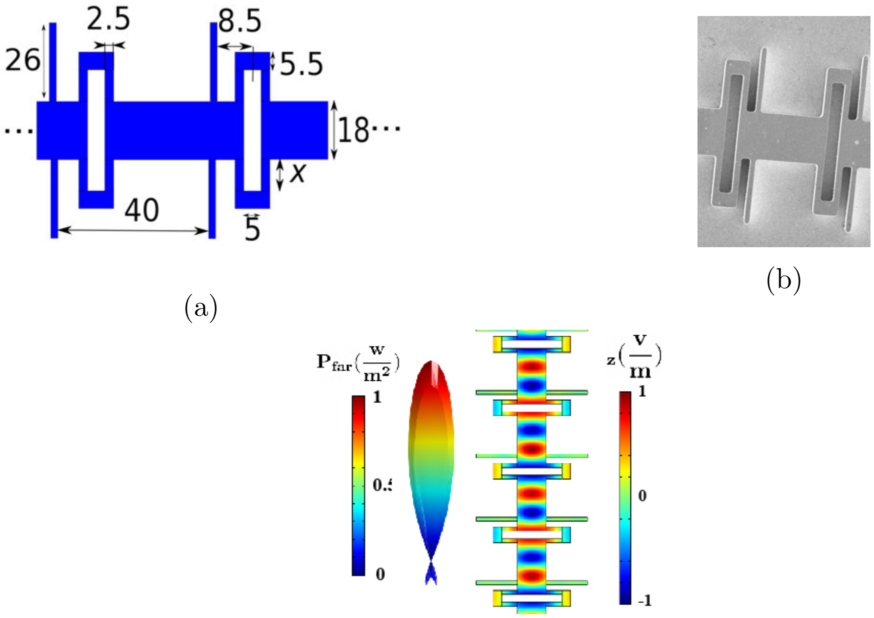

(a)

(b)

(c)

Figure 2-13: An ADFB with enhanced α_m (a) schematic of two periods. (b) SEM of a DFB device showing two periods. (c) simulated far field radiation pattern and mode intensity.

the new design along with the SEM pictures of the finished laser cavities are shown in Figure2-13. The higher mirror loss was achieved (from $\approx 12\ cm^{-1}$ to $15\ cm^{-1}$) by increasing the gap size between cavities and placing the antenna loop arms at the gap edge. The measurement results from this design are shown in Figure 2-14. Similar I-V characteristic and close lasing frequency (within 9 GHz) confirm minimal fabrication fluctuations. The maximum power of a front radiator with 10-μm antenna length is 16.1 mW at a bias of V_d=13.1 V and I_d=124 mA. The resulted wall plug efficiency is about 1%. Single-lobe beam pattern of the laser, which is shown in figure 2-14d, is confirmed using a FLIR camera [77]. Even though the main purpose of this work is to develop and demonstrate a conceptually novel scheme of unidirectional photonic wire lasers, the absolute performance in terms of CW WPE is also superior compared to previously reported results from DFB lasers.

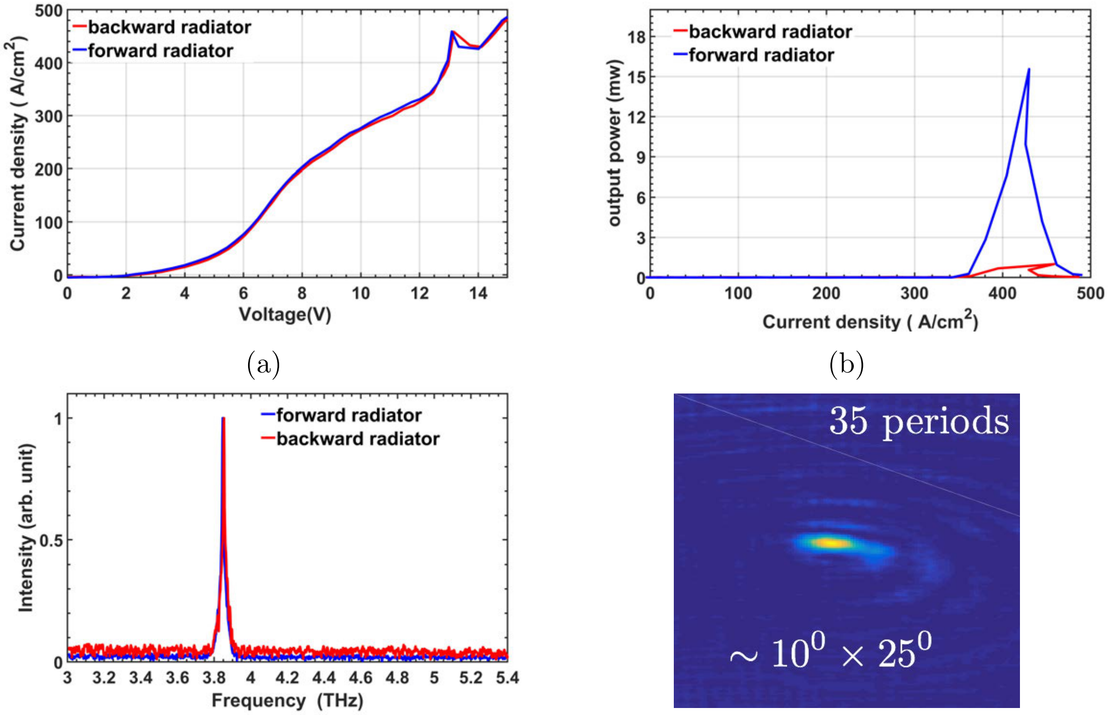

(a) (b)

(c) (d)

Figure 2-14: Measurement results for uni-directional 3rd-order DFB (a) V-I measurement from the DFB's with antenna loop of 10 um (b) L-I measurement, (c) frequency spectrum of the lasers (d) single-lobe beam pattern measured with a FLIR camera from the front radiator.

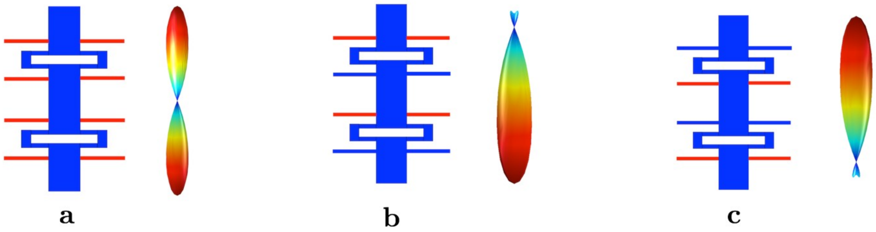

Figure 2-15: Testing the accuracy of finite element simulation a, both real and dummy reflectors are made of vacuum (vacuum shown with red color) b, dummy reflectors made of vacuum and reflectors made of GaAs (shown in blue color), c, dummy reflectors are switched with real reflectors.

2.6 Accuracy of Unidirectional ADFB Simulation

To test the symmetry of the mesh and validity of the simulations, we have performed the following checks. First, when both reflectors and dummy reflectors are made of vacuum, the pattern was perfectly symmetric as we expected and it is shown in figure 6.a. By keeping both reflectors and dummy reflectors and switching the material, the pattern flipped 180 degree confirming the validity of our meshing and simulations. (the structure mesh is exactly the same, only the materials were switched). This verification shown in Figure 2-15 indicates that asymmetry observed in the simulations is not due to any numerical artifacts.

Chapter 3

Phase-Locked Photonic Wire Lasers by π-Coupling

3.1 Introduction

Achieving tight beam pattern, single frequency, and high output C.W power at the same time in photonic wire lasers is a challenging task due to the deep sub-wavelength transverse dimensions. Moreover, in many applications, electrically tuning of the laser frequency is crucial, in addition to high output power and tight beam patterns [71]. In this chapter, a solution is presented to achieve these performance metrics simultaneously using an array of phase locked ADFBs.

3.2 Wire Laser Performance Metrics Review

A significant attempt has been made to improve wire laser performance in THz range in terms of output power and power efficiency, beam pattern, and frequency tunability. In this thesis, up to 1% wall plug efficiency with ≈16 mW of C.W power and single frequency operation by using a unidirectional antenna coupled third order DFB has been demonstrated [44]. By using a new hybrid-grating scheme that uses a superposition of second- and fourth-order Bragg gratings, peak power of 170 mW with a slope-efficiency of 993 mW/A is achieved [62]. In pulsed mode, peak THz output power up to 830 mW at 77 K and 1.35 W at 6 K is achieved using terahertz quantum-cascade vertical-external-cavity surface-emitting laser [43]. In terms of beam quality, using antenna-feedback method in terahertz QCLs, a single-mode terahertz QCL with a beam divergence as small as $4^\circ \times 4^\circ$ is demonstrated [78]. In terms of frequency tuning, by using piezoelectric actuators and an intra-cryostat cavity, tuning of $\approx$ 260 GHz at a center frequency of 3.3 THz is demonstrated with $\approx$5 mW of C.W power [79, 80]. Frequency tuning of a terahertz quantum cascade wire laser over a broad range of $\approx$ 330 GHz is demonstrated with a movable MEMS (microelectromechanical systems) side object (plunger) actuated mechanically [81] or by a mechanical comb drive [82] to manipulate the transverse optical mode. However, for practical applications, electrical tuning is much preferable. This is because electrical tuning is fast, continuous, and insensitive to mechanical disturbance. For pure electrical tuning, it has been demonstrated [83] that a laser device based on a coupled cavity, in which two "knobs" can be tuned by independently biasing the two devices, can achieve electrical tuning with a good range of $\approx$ 4 GHz (within 50% of output power variation) and 0.7 mW of C.W power. In microdisk lasers of small optical volume, a single whispering gallery mode can in fact be current-tuned by $\approx$ 30 GHz through the gain-pulling [84, 85], although the output power changed significantly over the entire tuning range. In a recent work, an electrical tuning method for terahertz QCL is developed based on detuned intersubband absorption in coupled metallic microcavities and $\approx$4 GHz continuous frequency tuning is achieved [86].

3.3 Phase Locking of Multiple Wire Lasers

Thus far, no scheme has been devised to simultaneously achieve good beam quality, high CW output power, and broad electrical frequency tuning, and the combination of all the three desired features is the main novelty of this work. Our scheme to achieve those performance metrics is based on phase locking of multiple wire lasers so that together they form a coupled cavity. A robust phase locking requires a strong coupling among the individual lasers so that otherwise-independent oscillators are forced to oscillate in sync, even if they are biased quite differently. There are five major demonstrated coupling schemes to phase-lock individual laser elements. Laser ridges can be coupled through exponentially decaying fields outside the high refractive-index dielectric core [87](evanescent-wave coupled), or through the Talbot feedback from external reflectors [88, 89](Diffraction-wave coupled), or by connecting two ridges to one single-mode waveguide [90, 91] (Y-coupled), or through lateral propagating waves [92, 93, 94] (Leaky-wave coupled), or through global mutual antenna coupling in far field [95]. The evanescent-wave coupled scheme could be possibly used for two wire lasers with ridge waveguides. However, straight ridge waveguides have very divergent beam pattern and low extraction efficiency. Diffraction wave coupling can also be used for wire lasers. However, this scheme requires an external component and delicate alignment, and it is sensitive to mechanical disturbance. The scheme of Y coupled ridge waveguides does not work well with DFB lasers, as the strong reflection in a DFB structure limits its facet coupling. Leaky-wave coupled schemes cannot be used effectively to couple DFB arrays as the radiation is mostly from radiation apertures and not from the end facets. For global antenna coupling [95], it is unclear if the phase locking can still be maintained if individual elements are biased at very different currents, which is required for frequency tuning at approximately constant optical power.

Here, we present a new scheme for phase locking of several ($\leq$5) wire lasers to form a coupled cavity, but with the main focus on the coupling of two for simplicity and clarity. We chose quantum cascade lasers (QCL) with antenna coupled third order distributed feedback grating (ADFB) as our platform [70]. ADFBs are a superior platform because of their tight beam pattern, high power, and high wall plug efficiency (WPE). Single-mode operation, high CW output power of 16 mW, 1% WPE, and tight beam patterns have already been demonstrated in this platform in chapter 2 of this thesis [44]. Schematic of a single ADFB is shown in Figure 3-1. When a perfect phase-matching condition is met, the modal index $n_{eff} = 3\frac{2\Lambda}{\lambda_0} = 3$, the radiations from all the antenna loops are in phase along the DFB structure, resulting in a tight far-field beam pattern [70]. Antenna loop increases the radiation (mirror) loss by

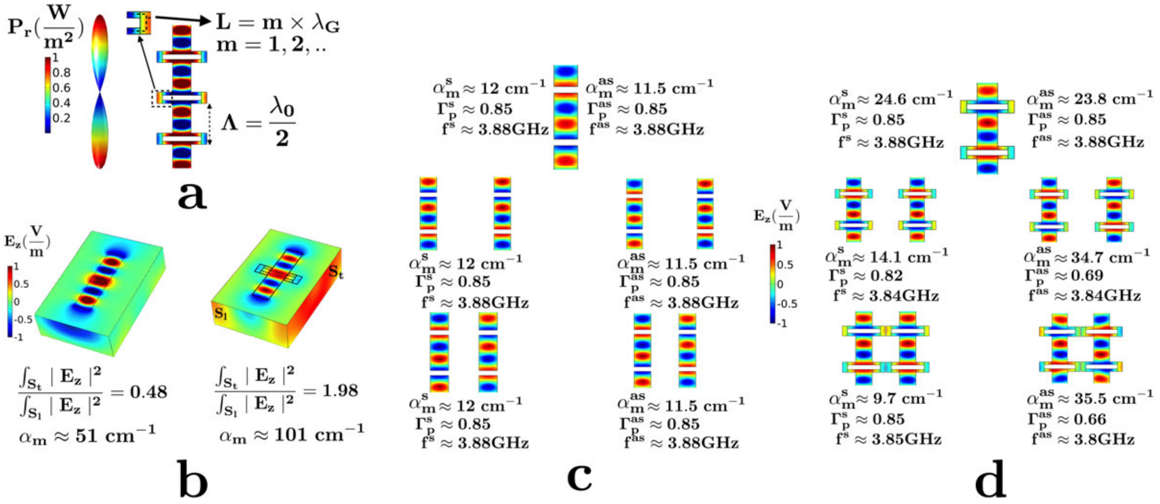

Figure 3-1: a. Schematic of simulated fundamental mode and the beam pattern of an ADFB, b. Comparison between lateral intermediate zone radiation of a short (with two periods) third-order DFB with and without antenna loop, c. mirror loss α_m for a supermode formed in π-coupled DFBs (without the loop antenna) with a center-to-center distance $\approx 4\lambda_0$, λ_0, $\frac{\lambda_0}{2}$ (to save space, only one DFB is shown for the $4\lambda_0$ configuration). Superscript S is for symmetric supermode and superscript A is for asymmetric supermode. d. α_m for a supermode formed in π-coupled ADFBs with a center-to-center distance $\approx 4\lambda_0$, λ_0, $\frac{\lambda_0}{2}$. Simulations in c and d are performed for 10 periods. The reduction in mirror loss is a result of a strong coupling between two cavities.

increasing the effective surface area for the radiation aperture. At resonance, the phases of the electric field inside the gaps are the same on both sides of the gap, thus the antenna length L should be equal to $m \times \lambda_G$ where m is a positive integer and λ_G is the wavelength in the antenna loop. One should notice that in an ADFB, the radiation is mostly from the antenna loop. Due to negligible facet radiation, Y and diffraction grating coupling schemes are not applicable here. Since the antenna loop length is determined by resonance condition, ADFB pairs are $\approx \lambda_G$ (defined above) apart so the evanescent lateral coupling between the ridges is negligible. Since an ADFB with even only a few periods produces a tight beam pattern in the longitudinal direction, far-field coupling through mutual antenna coupling is also not applicable here as this scheme relies on a very divergent beam pattern from individual lasers. Our simulation shows that the fundamental DFB mode is largely confined longitudinally near the center portion. This mode localization and negligible radiation from the facets limit the leaky-wave coupling [94]. Through this discussion, one can infer that the phase locking of ADFBs requires a new coupling mechanism, which is the π-coupling reported in this work. As a photonic wire laser, the radiation from each subwavelength aperture is very divergent. A simulated radiation profile of a single-period third-order DFB with (ADFB) and without antenna loop is shown in figure 3-1b. It can be observed that by attaching the antenna loop, not only the mirror loss increases but also the lateral field distribution in the intermediate zone ($\approx \lambda$) is significantly enhanced. The quantitative treatment of lateral radiation is shown in figure 3-1b through the integration of dominant component of electric field (here E_z). The strong lateral field distribution opens up the possibility for π-coupling of two or even more ADFBs. Since the coupling exists between all in-phase antenna radiation gaps, this scheme will be far more effective compared to earlier schemes utilizing the facet radiation. The same cannot be said for a third-order DFB without the antenna loop. Even though the beam from the radiating aperture is divergent, there is no strong coupling to an adjacent gap through π-coupling. Since a strong coupling will reduce the mirror loss α_m for the coupled cavities [95], it can be used to quantify the coupling strength. As shown in Figure 3-1c, α_m for the third-order DFB without the antenna loop [66] is not changed significantly as they are brought close to each other, indicating a negligible π-coupling between the two. In addition, for very closely spaced cavities the asymmetric mode has a lower radiation loss and thus it will be the lasing mode, as it has a quadrupole moment with a lower radiation loss than a dipole moment. On the other hand, as shown in Figure3-1d, α_m for ADFBs is significantly reduced as they are brought closer to each other due to a strong π-coupling of the in-phase aperture fields. We further notice that the cavities are decoupled for distance more than four wavelengths suggesting that the coupling mechanism is not strong in the far field. Even at the closest distance between the antenna loops, the two ridges are $\approx \lambda_G$ apart so evanescent wave coupling between the ridges is negligible, but α_m is reduced by ≈ 60 % indicating a strong coupling. Also, we cannot characterize this as the leaky-wave coupling as there is no complex wave vector in the lateral direction (no lossy guided mode in the lateral direction). To explain the selectivity between the symmetric and asymmetric mode, we emphasize that the shortest antenna loop length is λ_G at resonance, so that the tip of two parallel antenna arms is $\frac{\lambda_G}{2}$ apart from the edge of the gap, producing 180° phase shift compared to the field in the gap. For an isolated ADFB, the field in the gap is approximately constant and $E_{gap} \approx E_{\max}$, and the field near the tip should be $E_{tip} \approx -E_{\max}$ (but smaller in magnitude). Clearly, such a field distribution is totally compatible with that in the symmetric supermode, resulting in a minimum mode distortion. As can be seen in Figure3-1d, the mode profile for the symmetric supermode resembles closely to that in an isolated ADFB. The additional intracavity coupling reduces the mirror loss from that of an isolated ADFB. For the asymmetric supermode, however, the field at the centerline of the two ADFBs is identical to zero. Thus, when the two tips are brought together, the field at the tip should also be zero, which forces the field at the gap edge to be ≈ 0. This field distribution is quite different from an isolated ADFB, causing a significant mode distortion and consequently a lower mode confinement factor, as shown in Figure3-2. The lower confinement factor yields a higher mirror loss as shown in Figure 3-1d. The quantitative treatment of mode confinement factor for symmetric and asymmetric modes are given in Figure3-2. As it is shown, the

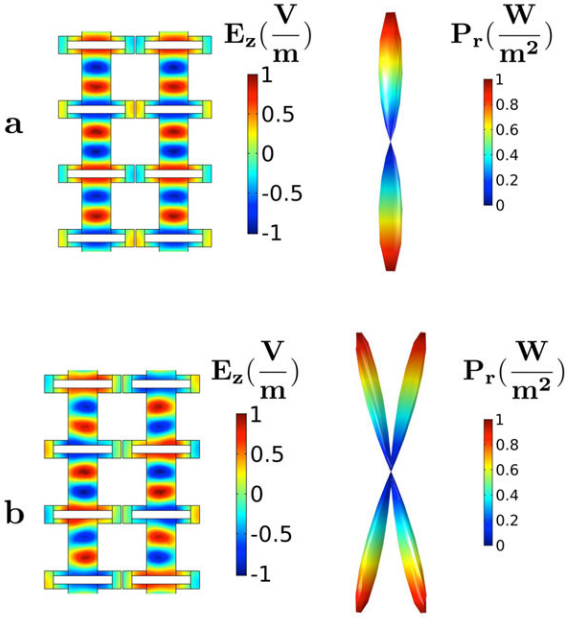

Figure 3-2: Comparison between the far field beam patterns for (a), symmetric and (b), asymmetric supermode of a -coupled ADFBs.

mode confinement factor for the asymmetric mode is decreased at a smaller distance between the ADFBs, indicating a higher level of mode distortion. As a result, the lasing threshold for the symmetric mode becomes much lower than the asymmetric mode due to its lower mirror loss and higher mode confinement factor. To emphasize the importance of mode selectivity between symmetric and asymmetric supermodes, Figure 3-2 shows the simulated difference between the far-field beam patterns of the asymmetric and symmetric supermodes. As expected, the dipole moment cancels out for an asymmetric mode and the quadrupole beam pattern appears. Without a mechanism to increase the mode selectivity, the asymmetric mode might be the lasing mode due to a smaller mirror loss. Using perfect electric conductor (for asymmetric mode) and perfect magnetic conductor boundary conditions (for symmetric mode), a relatively simple but sufficiently accurate simulation for an infinite number π-coupled ADFBs can be performed (since the dominant field component is tangent to those planes). By using these boundary conditions, the combined image fields resemble infinity in the lateral direction. The simulation results are shown in Figure 3-3. As illustrated, the power confinement factor is smaller for asymmetric mode indicating

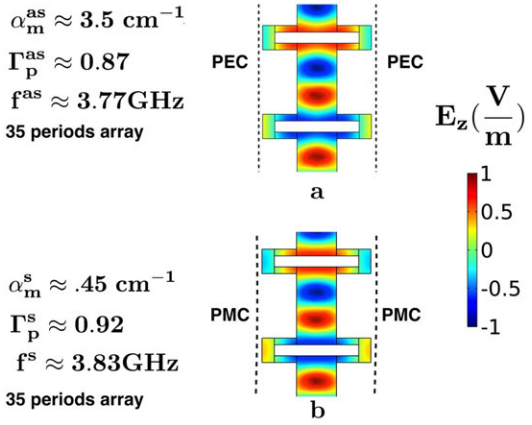

Figure 3-3: Comparison between the symmetric and asymmetric modes of an infinite stage π-coupled ADFBs.There are 35 periods. Antenna length is set to be 9 m and the antenna loop tips are 5.5 m in thickness

a greater mode distortion from that of an isolated ADFB due to the perfect electric conductor boundary condition (the image current resembles neighbor ADFBs)

3.4 Results And Discussion

To implement the idea, we fabricated an array of π-coupled ADFBs. A schematic of the array along with several geometry parameters are shown in Figure 3-4. Each array has 10 pairs of π-coupled ADFB. The antenna-loop length is varied from one pair to another to adjust the resonance condition. The distance between the pairs is designed to be sufficiently large to avoid inter-pair coupling. Considering the fabrication resolution, the gap between the antenna loops in an ADFBs pair is set to $\frac{\lambda_0}{40} = 2\,\mu m$. The size of the gap within the antenna loop is 5.5 μm to ensure a high mirror loss α_m. Based on the simulations, α_m for the supermode is 40% of that of a single ADFB and predicted to be 6 cm^{-1} for the symmetric supermode. The center frequency of π-coupled ADFBs in this chip is designed to be around 3 GHz apart from the adjacent pair (by simply increasing the antenna loop length by 4%, monotonically decreasing frequency shift can be achieved). The measurement results are shown in Figure3-4e and Figure3-4f. The observed interdependence of current thresh-

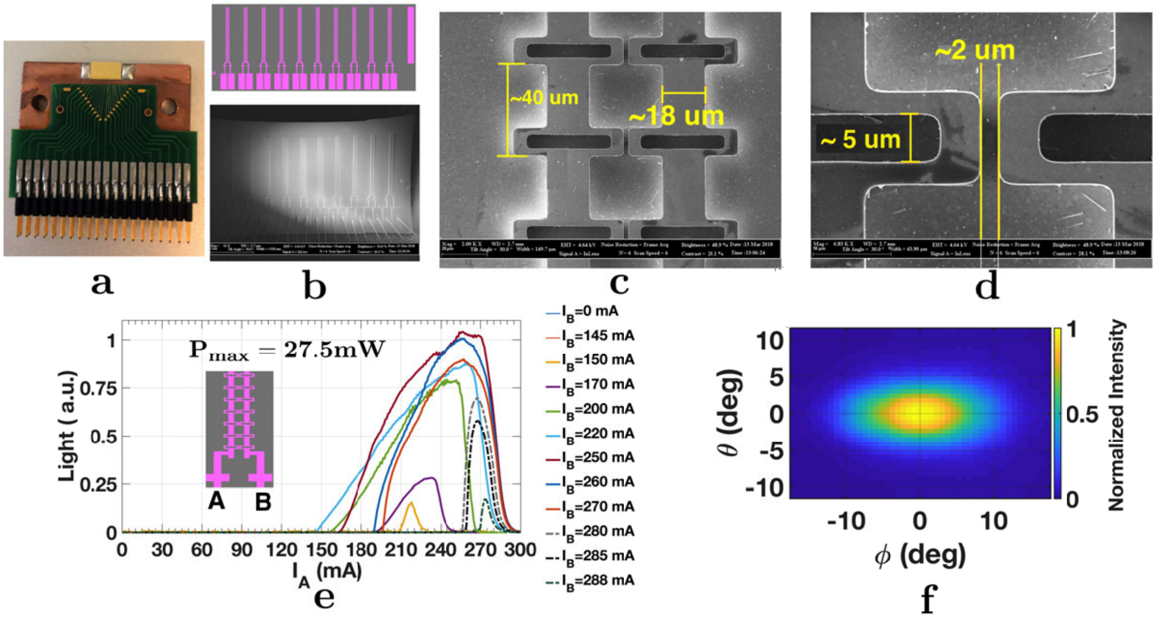

Figure 3-4: a. Electronic chip for simultaneous independent biasing, b. A fabricated die with 10 pairs of π-coupled ADFBs, c. Three periods are shown (from total 35 periods) in the fabricated π-coupled ADFB, d. Magnified SEM image of the gap between the antenna loops, e. light-current curves, f. beam pattern.

olds and single lobe beam pattern is a strong evidence for a symmetric supermode. In particular, no lasing was observed if one ADFB was unbiased suggesting a significant loss in a cold cavity and a strong coupling between the two. When both are biased, as the bias for one ADFB is increased, the lasing threshold for the bias of the other ADFB decreased indicating the total gain increased in the coupled cavity. To measure a possible frequency offset between the two π-coupled ADFBs, we prepared the experimental set-up shown in Figure 3-5. The reference laser shown in Figure 3-5 is turned off for this measurement. The free running beatnote was measured in heterodyne scheme to accurately measure the frequency (typical FTIR resolution of ≈3 GHz is not sufficient for such experiment). The Schottky mixer is integrated with a horn antenna and a Bias-Tee box. The horn antenna aperture size is $\approx 500\ \mu$m $\times$ 500 μm. The beam from the π-coupled ADFBs and the reference laser were focused on the Schottky mixer input RF/LO port (horn antenna aperture, marked 1 in Figure 3-5). The focusing was achieved using two off-axis paraboloid mirrors. The IF output port, which contains the beatnote signal between the reference laser and the -coupled

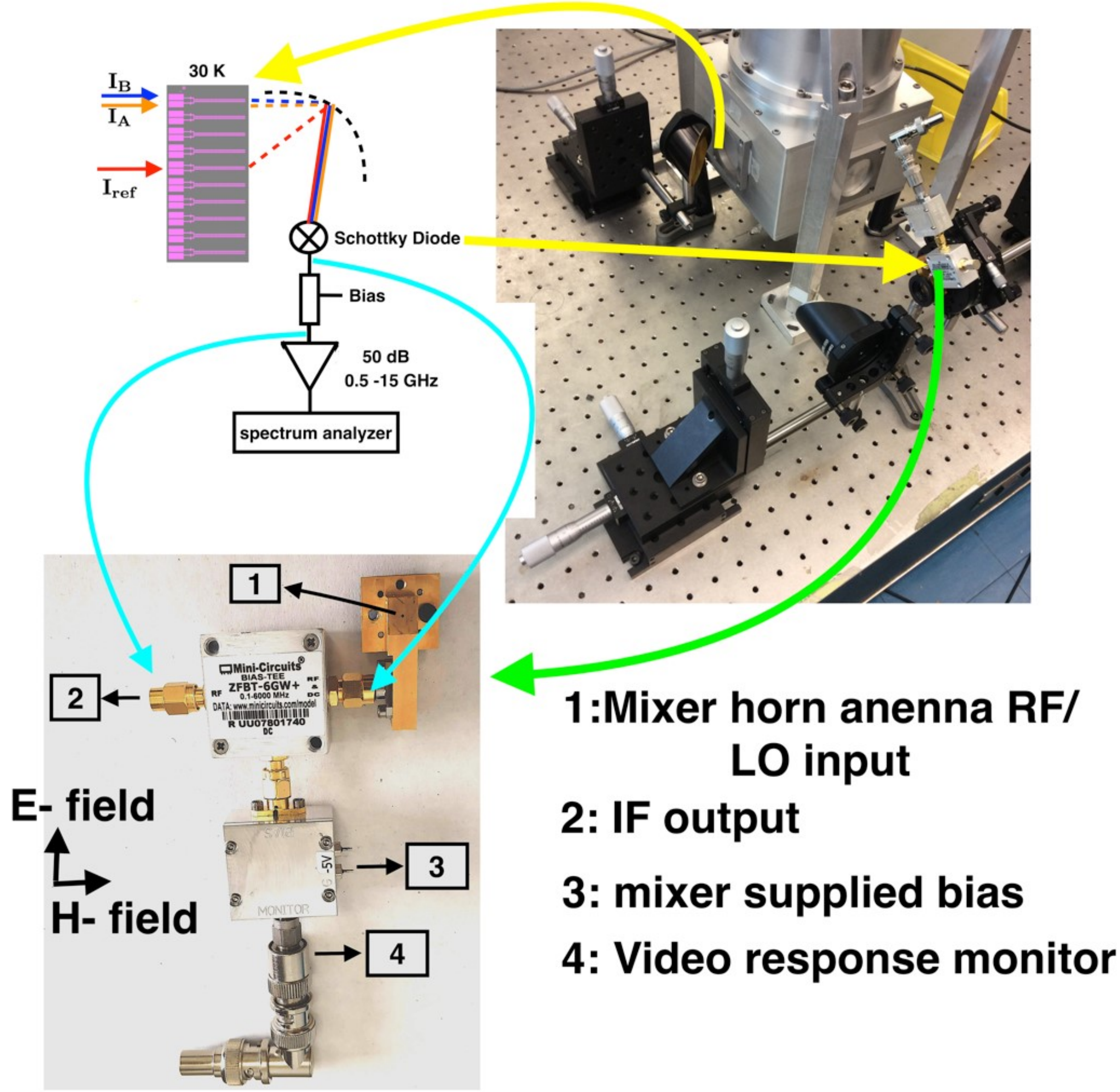

Figure 3-5: Experimental set-up for heterodyne mixing to measure a possible frequency difference between π-coupled ADFBs, and later to measure the frequency tuning with high resolutions (≈ 1 kHz).

ADFBs (port 2 marked in figure 3-5), was connected to a low-noise amplifier with 50-dB gain. The output of the low-noise amplifier was connected to a spectrum analyzer. The free running beatnote has a variation range about 50 MHz due to thermal fluctuation and mechanical vibration. (we did not phase lock the reference laser and the coupled ADFBs due to a negligible variation relative to the frequency difference which is ≈ GHz). The resolution bandwidth of spectrum analyzer was set to 1 MHz for high SNR. The video response monitor port yields the power detected by the mixer. We have observed single-mode operation (without observing any beatnote up to 20 GHz with kHz resolution) in the entire bias range shown in Figure 3-4e. This indicates that the π-coupling scheme is strong enough to maintain a robust phase locking throughout the entire bias range.

The main motivation for the phase-locked ADFBs with separate biases is to achieve frequency tuning at approximately constant power. Since changing the relative bias of π-coupled ADFB changes the gain profile, from Kramers-Kronig relation [96] this change causes changes in the refractive index that produce a slight frequency shift. In more technical terms, this is referred to as mode-pulling effect, which is produced by the blue-shift of the underlying gain profile with applied bias, and the associated change in the refractive index shifts the resonance frequency [97, 98]. Based on this change of refractive index, π-coupled ADFBs can produce continuous frequency tuning with a greater tuning range than a single device as they can act like a master-slave oscillator. Using the same set-up shown in Figure 3-5, we used another π-coupled ADFBs on the same die as the reference (we did a separate measurement confirming its single-mode operation) that was three pairs away from the π-coupled ADFB under investigation. The distant pair is chosen to ensure a sufficient separation of center frequencies and to avoid a possible local heating. In order to rule out thermal tuning, the cold stage was stabilized at 30 K using a Lake Shore PID temperature controller. The frequency of the reference and the π-coupled ADFBs measured by FTIR (their relative positions on the die are shown in Figure 3-5) is shown in Figure 3-6a . Figure 3-6b shows the beat frequency along the current path shown in Figure 3-6c (in the black line, which was aimed for minimum power variation). Figure 3-6d shows the

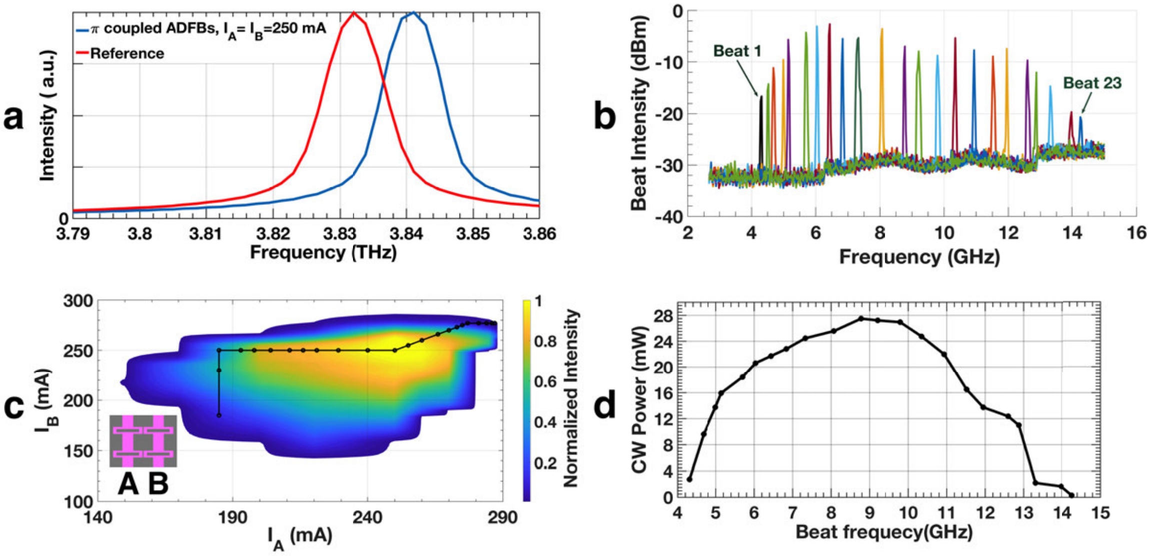

Figure 3-6: Frequency tuning of π-coupled ADFBs, a. measured frequencies from a FTIR, b. the frequency difference between the π-coupled ADFBs and the reference measured using a Schottky diode mixer, c. a 2-D path for the different bias levels based on the dynamic range and output power consideration, d. output power versus the beat frequency.

output power of the super mode at corresponding points. We have observed ≈10 GHz of frequency tuning with maximum CW output power of ≈ 27 mW. 7 GHz of this frequency change is within 50% power change. Even though we only included a few points in the graph, we observed a complete continuous change on spectral analyzer as we changed the biases along the indicated path. No mode hopping was observed. It is worth mentioning that, due to a very sensitive beam alignment to such a small aperture of the integrated horn antenna, any instability in far field beam pattern of the lasers can be easily detected. Even though we did not measure the beam pattern at every bias point, the strong beatnote along the path provided in Figure 3-6 indicates the stability of the far-field beam pattern at different bias points.

Since all off-centered π-coupled ADFB are tested and proved to be single modes, one can design the center frequency of each π-coupled ADFB to be about 10 GHz (for this gain medium) apart. In that case, by electrical switching between the π-coupled ADFBs, a much greater continuous tuning range can be achieved. As shown in Figure3-1d, the supermode in π-coupled ADFB has significantly lower mirror loss than the uncoupled counterpart. It is well known that the output power from a laser

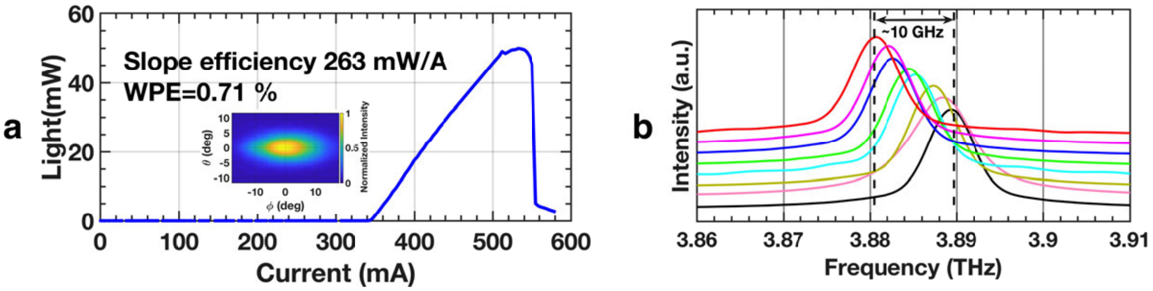

Figure 3-7: Result of a π-coupled ADFBs optimized for output power, a. $I_A = I_B$ light-current curve and beam pattern, b. spectra taken with a FTIR on a linear path shown in a.

is proportional to $\frac{\alpha_m}{\alpha_m+\alpha_w}$, where α_m is the mirror (radiation) loss and α_w is the waveguide loss [75]. For a maximum output power,$\alpha_m = \alpha_w$. In our case the measured [76] $\alpha_w = 15cm^{-1}$. Therefore, one can design individual ADFBs with much higher mirror loss so that the π-coupled ADFB have optimum mirror loss for the symmetric supermode. Here we used another pair of ADFBs and increased the antenna gap size to 6 μm. Simulations show an 8 cm^{-1} mirror loss for the symmetric supermode. The measurement results are shown in Figure 3-7. Measurement confirms a single-mode frequency at 3.87 GHz with ≈10 GHz of frequency tuning, ≈50 mW of CW power, and high-quality beam pattern. The Wall plug efficiency was measured to be 0.71% and the slope efficiency was 263 $\frac{\mathrm{mW}}{\mathrm{A}}$. Here, having already proved the continuous nature of frequency tuning, we simply measured the spectra with an FTIR. In order to demonstrate the versatility of the π-coupled phase-locking mechanism, we have designed and fabricated π-coupled ADFBs with more than two ADFBs. By coupling more ADFBs, even higher power levels can be achieved; and in principle, with more knobs to turn, a better performance (for example, less power variation over the entire frequency tuning range) can be achieved. Figure 3-8 shows the results for π-coupled 3,4,5 ADFBs with each having 35 periods and 5.5-μm slot gap size. For fabrication and operation simplicity, here all the ADFBs are biased together using one bonding pad. The single-mode spectra and single-lobe beam patterns clearly show that these ADFBs are phase locked. As the number of ADFBs is increased, the lateral beam pattern becomes narrower, as expected. The total current for the coupled ADFBs scales

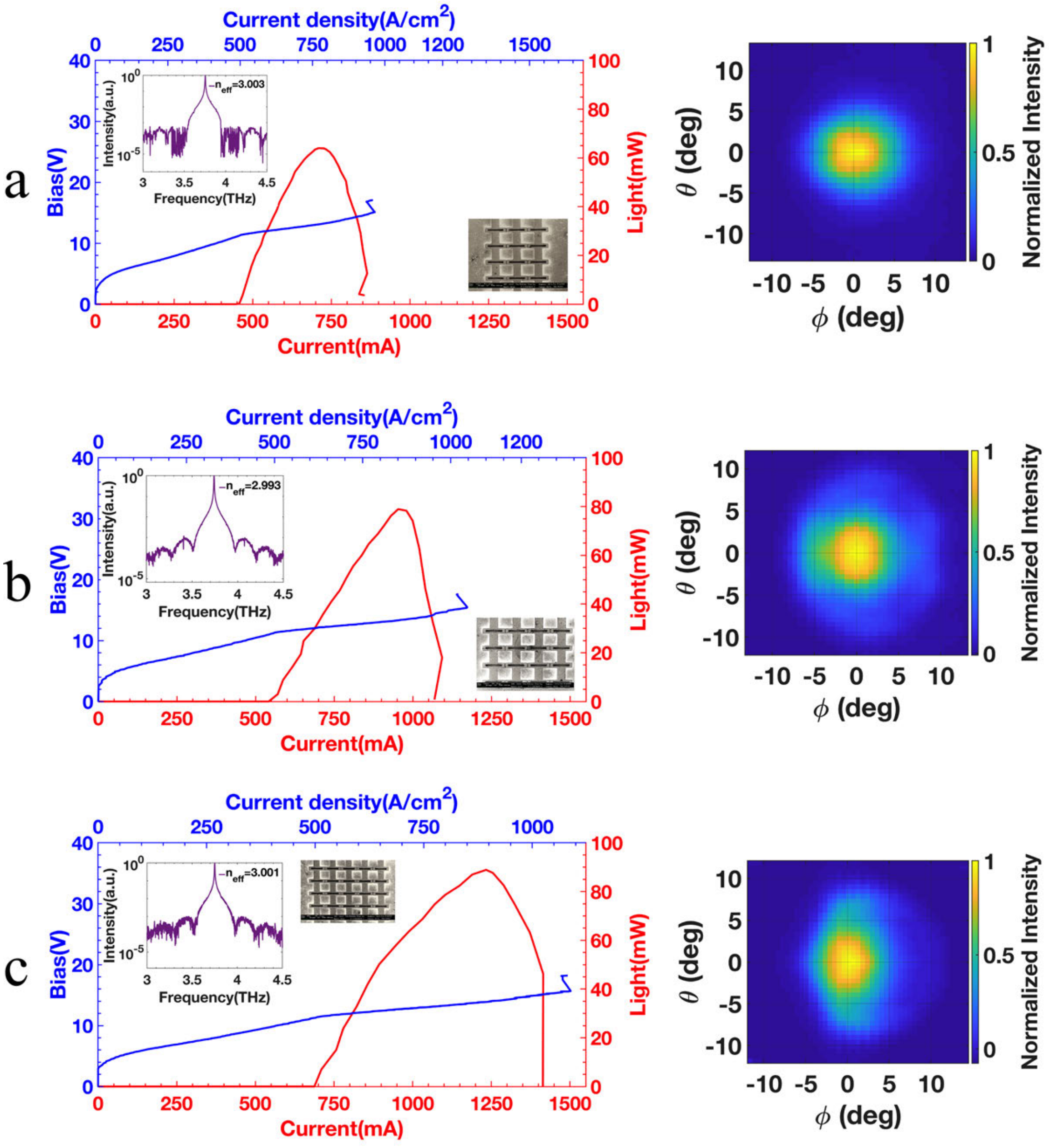

Figure 3-8: Spectra, beam patterns, and LIVs for, a. three π-coupled ADFBs, b. four π-coupled ADFBs, c. five π-coupled ADFBs.

linearly with the number. However, the output power is not increased linearly since the mirror loss decreases with an increasing number of coupled ADFBs. It is worth noticing that the effective index for the coupled array is closer to 3 than individual elements. By increasing the number of coupled ADFBs, the radiation loss decreases, which increases the effective modal index and brings it closer to the ideal value for perfect phase matching ($n_{eff} = 3$). Such phase matching is difficult to achieve for high-power single ADFB since it will require a larger slot gap size that yields $n_{eff} > 3$. In conclusion, we have demonstrated a novel π-coupled scheme to phase lock 2,3,4, and 5 ADFBs. The coupling mechanism is strong enough to maintain a robust phase locking at all biases. Tight beam pattern ($\approx 10^\circ \times 15^\circ$), CW output power of ≈ 50 mW for two π-coupled ADFBs (≈ 90 mW for five π-coupled ADFBs with $\approx 6^\circ \times 8^\circ$ FHBW), and ≈ 10 GHz of continuous electrical frequency tuning is demonstrated at 30 K. With the 20-pins connector shown in Figure 3-4a (which is by no means the upper limit), one can envision to bias 10 pairs of ADFBs with a frequency separation of $\approx$ 10 GHz by varying the lengths of the antenna loops and the periods of the DFB structure. With each pair of ADFBs tunable continuously by $\approx$10 GHz, the whole chip can be electrically tuned continuously over $\approx$ 100-GHz. Such broad and continuous electrical tuning will be highly desirable in sensing and imaging.

Chapter 4

Unidirectional Photonic Wire Laser For GUSTO

4.1 Introduction

The neutral oxygen [OI] line at 4.7 THz is rich with information about star formation. It mostly probes warm natural gas heated by massive newborn stars [20]. Despite its great interest to the astrophysics community, this spectral line has been inaccessible due to the lack of local oscillators (LOs). Far-infrared gas lasers have only discrete lines, and the closest line is 8 GHz away from the 4.744 OI line. The invention of THz QCLs made it possible to do heterodyne observation on this line, and even map it within the Milky Way galaxy.

The [OI] line was detected in the Martian atmosphere using a THz Quantum Cascade Laser (QCL) as the local oscillator with 100 μW of power on 14 May 2014 using the high-frequency channel of the far-infrared heterodyne spectrometer GREAT (German Receiver for Astronomy at Terahertz Frequencies) on board SOFIA (Stratospheric Observatory for Infrared Astronomy) [99]. Following SOFIA's success, Stratospheric Terahertz Observatory (STO2), a NASA balloon-borne mission, was launched from Antarctica on 9 December 2016. Once high above the Antarctic (36 Km), STO2 circled along with the polar vortex for a period of three weeks. During that time STO2 picked up emission lines at 1.4 and 1.9 THz from ionized nitrogen (NII) and ionized carbon (CII). The local oscillator at 4.7 THz failed in STO2 due to a unforeseen technical issue which disconnected the electrical bias from the QCL used as local oscillator. To further improve the results and include the [OI] line measurements, the Gal/Xgal Ultra-Long Duration Balloon-borne Spectroscopic THz Observatory (GUSTO) will be lunched in 2021 [71, 100, 101]. GUSTO will boost our understanding of the universe by probing the interstellar gas throughout the Milky Way and Large Magellanic Cloud (LMC). GUSTO consists of a semi-autonomous 0.9 m Cassegrain telescope, which is a reflecting telescope and cryogenic detection system designed to stay aloft for 100 days. During this time, GUSTO will use its heterodyne array receivers to survey 124 square degrees of the Milky Way and all of the LMC in three important interstellar lines. This brief chapter describes the technical details behind the development of local oscillator at 4.7 THz using unidirectional antenna coupled third order DFB (UADFB) described in chapter 2.

4.2 Performance Metrics

The required performance metrics for the local oscillator were calculated by researchers at SRON and university of Arizona to ensure the proper performance of HEB receiver array and phase grating integrated with the optical set-up [102, 103, 104]. By taking into account the optical losses, non-Gaussian beam pattern of THz QCL, and the available cooling power, the overall performance metrics were calculated and listed in Table 4.1.

performance metric	requirements
nominal frequencies(GHz)	4740.0, 4741.6, 4743.6, and 4749.2
C.W output power	$\geq$1.6 mW at 45 K in single lope
tunability	± 1.5 GHz at nominal frequencies
bias and heat dissipation	voltage$\leq$24.0 V, power dissipation $\leq$ 2.2W

Table 4.1: GUSTO requirements for the local oscillator at 4.7 THz. For GUSTO, the QCL is cooled with approximately 2W lift at 45 K (6W lift at 60 K) provided by a Sunpower CT cryocooler.

4.3 UADFB for GUSTO

In designing a UADFB, there are 9 design parameters as shown in a schematic in Figure 4-1. For reliability of electrical biasing and reducing the risk of burning the top metal stack of antenna loop (Ta(15 nm)/Au (250 nm)) due to heating, t_L=3 μm and w_L>=5.5 μm are used. Increasing the t_L improves the DC bias reliability, but it also increases the perturbation to the fundamental 3rd order mode and consequently reduces the temperature performance by increasing the radiation loss. For active media with $J_{\max} \leq 1200 \ \frac{A}{cm^2}$, those suggested thicknesses have been experimentally verified and no failures have been observed. Similar considerations exist for t_R. Due to large aspect ratio of the reflectors, thin reflectors will be damaged during the fabrication process and thick reflectors will introduce additional undesired perturbation to the fundamental mode. For GUSTO, t_L=2.5 μm has produced reliable performance. To avoid distortion to the beam pattern due to deviation from the perfectly phase matching condition ($n_{\text{eff}} = 3$), the periodicity of the elements should be close to $T = \frac{c}{2f} \approx 31.6$ μm. Having those parametrs in mind, an optimized UADFB at ≈4.74 THz using COMSOL finite element solver is shown in Figure 4-2. The base design was taken by proper scaling from optimum designs presented in chapter 2 at 3.9 THz.

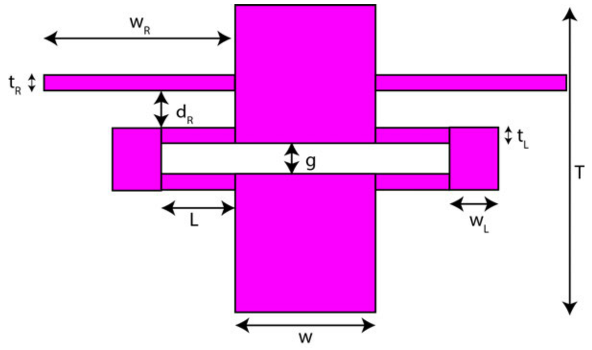

Figure 4-1: A schematic of a UADFB and the relevant design parameters.

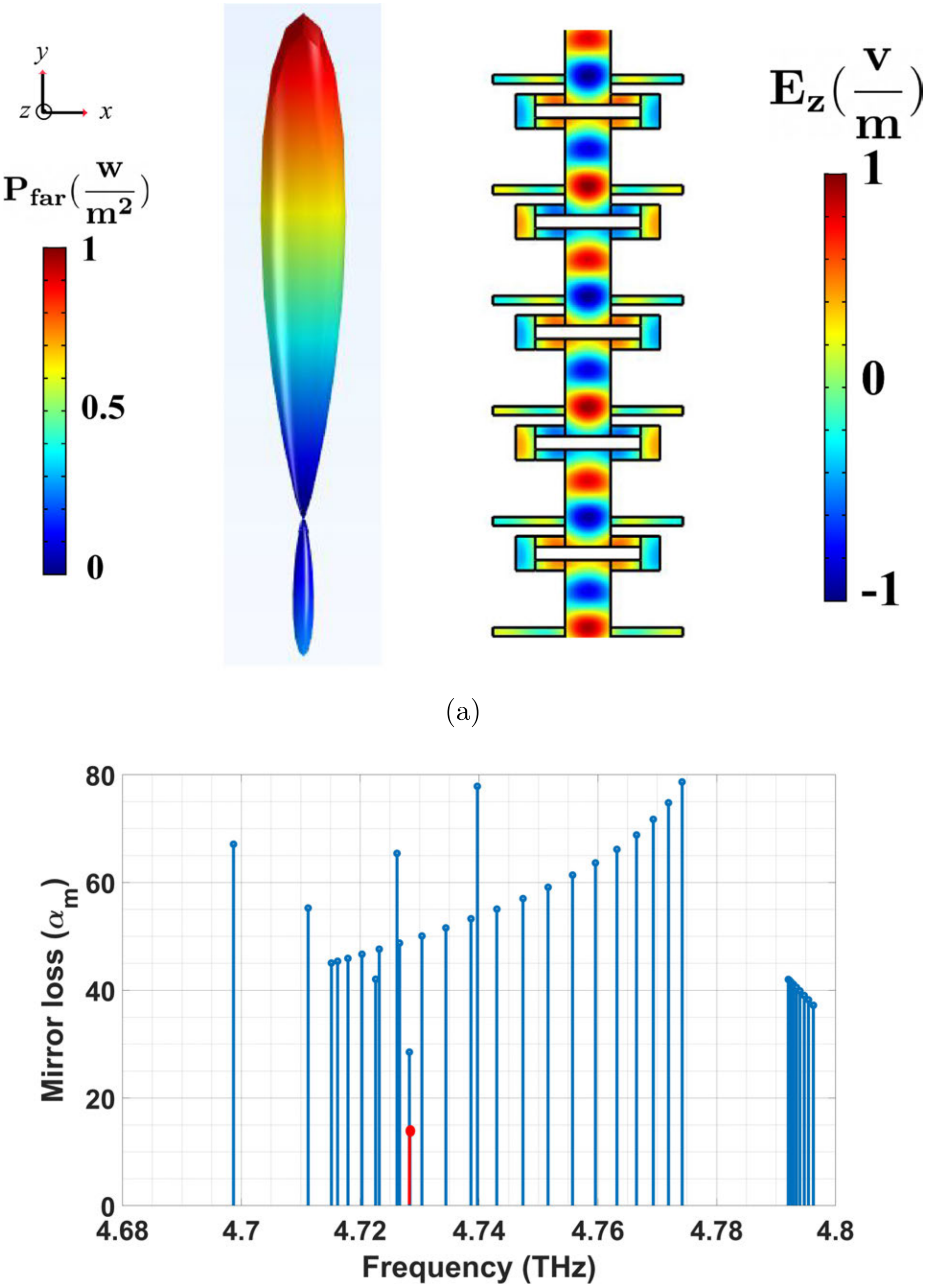

(a)

(b)

Figure 4-2: An optimized UADFB with w_R=20, t_R=2.5, d_R=3, t_L=3, G=3.75, L=8.5, w_L=5.5, W=13, T=31.4. All units are in μm and the number of periods is 30. (a) Simulation for mode profile and far-field beam pattern. $n_{\mathrm{GaAs}} = 3.66$ were used for simulations. (b) Mirror loss (α_m) for various modes. The desired 3rd order mode is marked with a red color.

4.4 Frequency Tuning

Fabrication fluctuation and the change in the peak gain of active medium can produce as large as 200 GHz change in the lasing frequency of a fabricated UADFB compared to simulations and prior fabrications of the same design. Therefore, broad and narrow tuning of lasing frequency is required to achieve accuracy of ≈ 3 GHz in the lasing frequency crucial for GUSTO.

The UADFB cavity width (W), the length of antenna loop arm (L), the periodicity (T), and the size of the gap between micro cavities (G) are the major tuning parameters of the lasing frequency in a UADFB. W can be used to tune the lasing frequency (W↓f↑,W↑f↓). However, care should be taken in the design as wider cavities (W↑) are prone to higher order lateral mode overlap with the fundamental third order mode and narrower cavities (W↓) are prone to lower confinement factor and susceptible to higher loss due to roughness of sidewalls. However, by proper design, the cavity width can be used to achieve discrete frequency tuning in the order of ≈100 GHz. The length of the antenna loop arm (L) can be used to tune the lasing frequency (L↓f↑, L↑f↓). However, the frequency tuning is limited and the power variation due to the change in radiation loss is significant. More specifically, for uni-directional ADFB design, there is an optimum L for achieving highest asymmetry ratio in the forward direction as explained in chapter 2. Therefore, L is not used for large frequency tuning (≥100 GHz) in an UADFB. Antenna gap size can also be used to tune the lasing frequency (G↑f↑, G↓f↓). However, for large frequency tuning, the change in the output power will be significant. Therefore, adjusting G is not used for frequency tuning. However, G is the main parameter which controls the mirror loss and therefore the output power and maximum lasing temperature. This parameter should also be optimized for ultimate temperature performance while maintaining the required output power. The periodicity (T) of the UADFB can also be used for frequency tuning (T↓f↑, T↑f↓). However, deviating from $n_{\text{eff}} = 3$, reduces the beam quality. Therefore, an accurate simulation to target the right frequency is a key to minimize the index mismatch if periodicity is used to tune the lasing frequency.

4.5 Design Strategy

The major design strategy is to fabricate multiple DFB arrays with a defined geometry relation between elements on the same sample ($\approx$ 1.3 cm × 1.3 cm). The width of micro-cavities is used to achieve discrete large frequency change at the center of each DFB array (100 GHz with $\approx 1\mu$m chnage in W) and the periodicity is used (30 nm steps) within each array to achieve $\approx$ 3 GHz change in the lasing frequency. Within the same sample, the gap size (G) should also be adjusted to achieve high power and good C.W performance at high temperatures (T>45 K). Wider gap, which results in in a greater mirror loss, will possibly yield higher power at lower temperatures but it might reduce the power at higher temperatures due to limited gain at 50 K. An example of the lithography mask used for GUSTO is shown in Figure 4-3. Each DFB array is consist of 18 DFBs which are closely spaced and their lasing frequency is finely adjusted through the change in their periodicity. The choice of 18 DFB per array is to ensure minimum wire bonding angles and uniformity in indium bonding in mounting process. An example of such array is shown in Figure 4-4. To achieve 3 GHz frequency tuning in a UADFB at 4.7 THz, the change in the periodicity is only 30 nm which is far from a resolution achievable by non-Ebeam lithography tools. For example MLA150 mask-less aligner used at MIT cleanroom has a nominal 1 μm resolution. Though below the resolution, the relative change in the mask will produce relative change in exposure for the neighbour devices. Such change in the exposure dose, will impact the development process and the undercut in the developed photoresist will impact the geom try size in the lift off process for the definition of the top metal stack. The benefit of avoiding Ebeam lithography is to achieve thicker metal stack (>100 nm) and process larger samples required to cover a large frequency range.

4.6 Experimental Results

The light-current-voltage-spectrum results for a flight candidate device is shown in Figure 4-5. This samples is fabricated on wafer VB1054 grown at SANDIA national

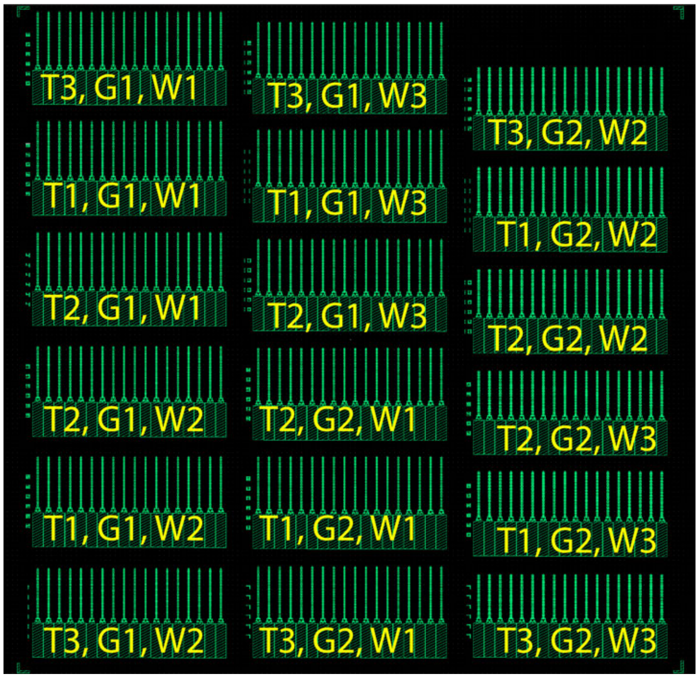

Figure 4-3: A fabrication mask to cover 200 GHz.W_3=13, W_2=14, W_1=12.5, G_2=3.75, G_1=3.5, $T1$=30.8-0.03-31.3, $T2$=31.33-0.03-31.85, $T3$=31.88-0.03-32.4. All the units are in the dimension of μm. For the first and second columns, the number of periods is 35 and for the third column is 30.

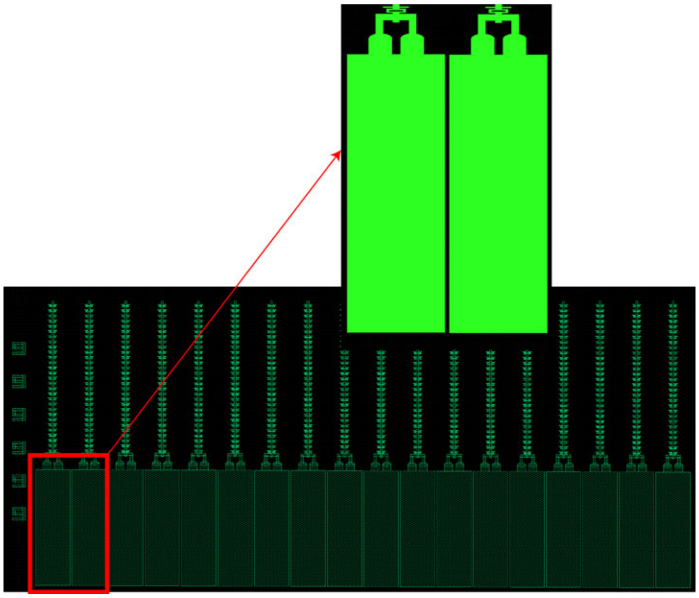

Figure 4-4: DFB array using periodicity for fine adjustment of the lasing frequency. Bonding pads are 210 μm× 700 μm. The spacing between bonding pads is 10 μm.

laboratory based on a modified version of a wafer proposed in [105]. The original 15% barrier suggested in this paper failed to produce satisfactory results. By increasing the barrier composition to 17%, the performance was improved.
Though the neighbour devices have 3 GHz frequency spacing, a combination of red sift in lasing frequency with temperature and blue shift with electrical bias (stark shift) in one of the UADFB could cover the entire frequency band required by GUSTO. Those devices produce 3 times more power that required performance due to high power emission achieved by uni-directional design.

4.7 Bonding Pad Failure At C.W Bias

UADFB laser ridges are too narrow ($\approx$13 μm) for direct wire bonding(in wedge bonds, w should be ≥ 65 μm), which is required for DC electrical biasing. Bonding pads are used for electrical biasing for such narrow ridges. However, using bonding pads adds multiple reliability risk factors to C.W performance and complicates the fabrication process due to the addition of insulation layer. During the course of developing UADFB at 4.7 THz for GUSTO, three bonding pad failures occurred caused by the melting of top metal stack through Joule heating.

There are three main causes for such failures. First, gold contamination during metal evaporation could have occurred. For multi-user facility clean-room, the metal flakes accumulated on the shutter can fall inside the metal evaporation crucible during soaking process. Such contamination were recently reported at MTL clean-room facility. A dedicated gold crucible were used afterward to minimize the risk of cross contamination for GUSTO. Second, GUSTO requires two wire bonds per bonding pad for mechanical stability. However, each wire bond leaves considerable visible damage on small pads with thin gold stack (top metal stack <500 nm). An example of such failure and the visible damage to the pads are shown in Figure 4-6. The melted bonding pads appears in black color in this figure. In most cases, the discoloring of gold layer on bonding pad and subsequently melting initiates at the position of the wire bond. This is emphasized with a blue rectangular box in Figure 4-6. The onset

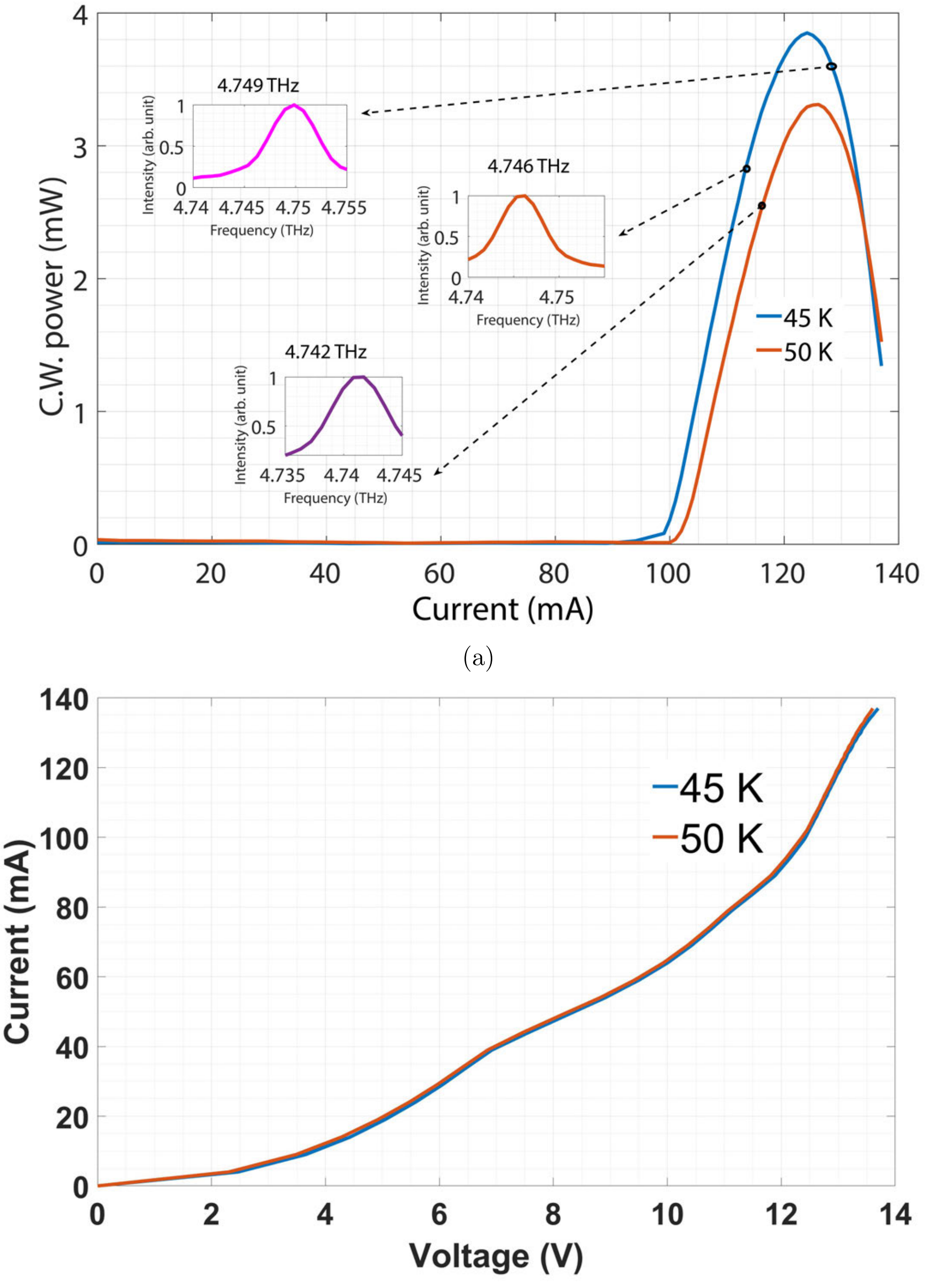

(a)

(b)

Figure 4-5: L-I-V, spectrum for a GUSTO flight candidate device (a) L-I with spectrum as inset. Lower frequency can be achieved at 55K. (b) V-I.

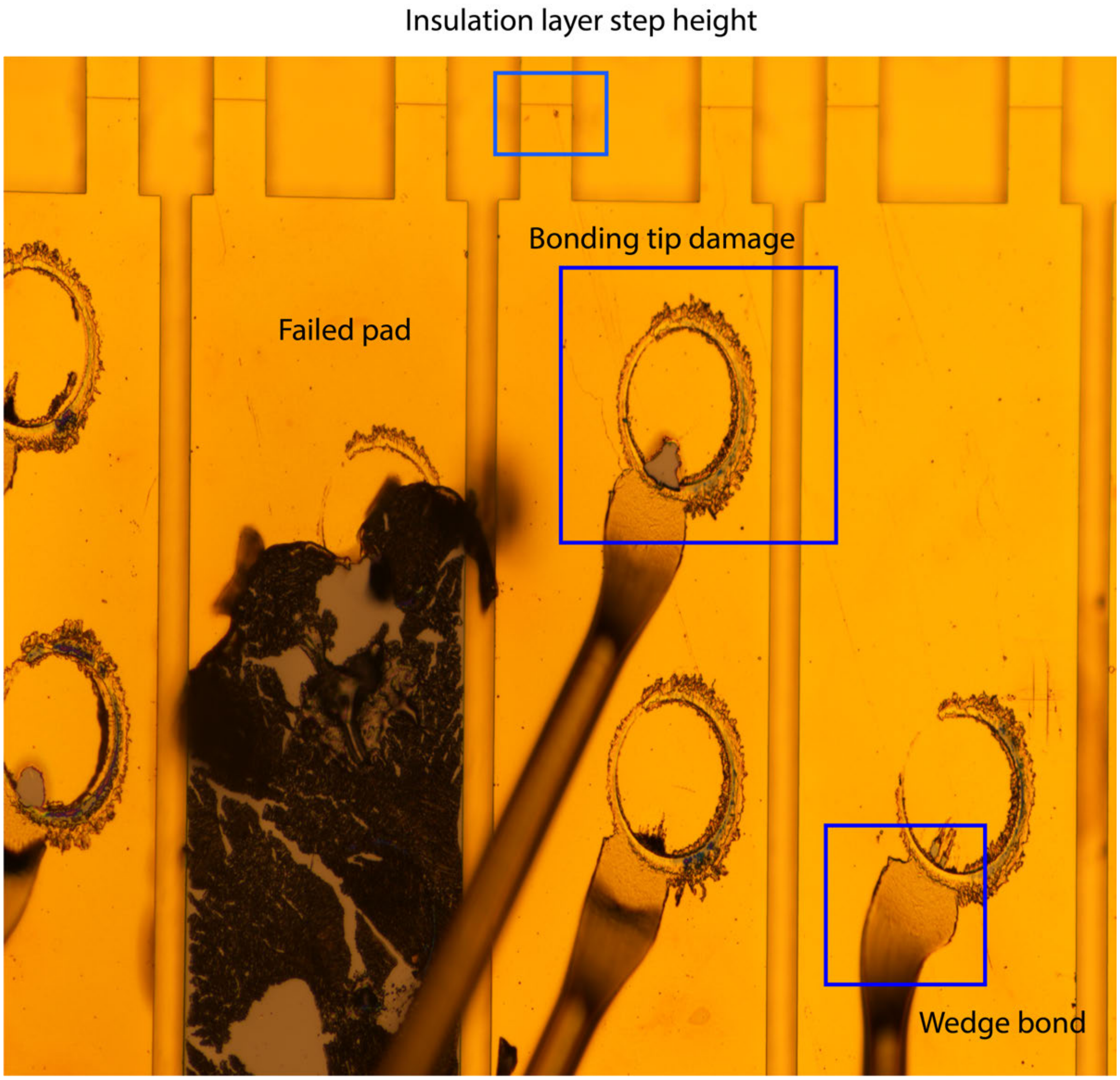

Figure 4-6: Bonding pad failure due to the damage occurred during wire bonding.

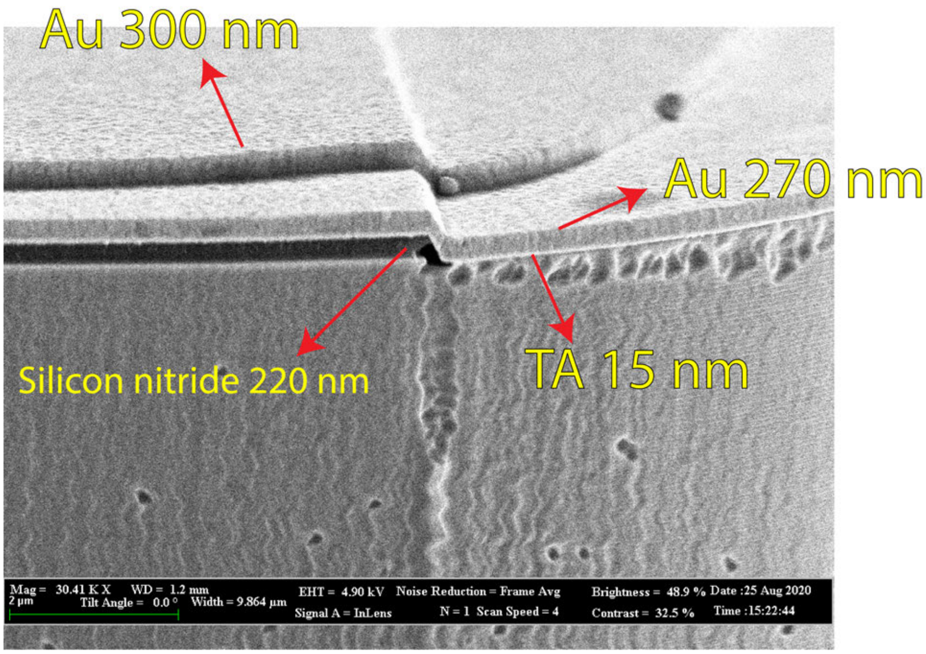

Figure 4-7: Double gold process on bonding pads.

of such discoloring close to the wire bond wedge is visible in this figure. Such damage is more substantial for smaller pads due to higher pressure on the pads during wire bonding. In one particular fabrication attempt, all the bonding pads with 175 μm × 500 μm dimension burned. Third, Silicon nitride which is used for insulation layer is a poor thermal conductor at cryogenic temperatures. In addition, thermal conductivity of this film grown at lower temperatures compatible with QCL processing (T<300 c) is even lower due to porosity of the film. Aluminum oxide can offer alternative for this issue. However, electrical breakdown was observed in one attempt with 100 nm of aluminum oxide deposited with ALD. Due to the time constraints, this approach were not pursued further but it is recommended for future developments.

Another source of failure is the insulation layer step height junction (ISH junction). As the bonding pads are at an elevated plane compared to the DFB ridges, there is a step height between the two sections as shown in the Figure 4-8. ISH junction is often visible under optical microscope. The gold on the ISH junction is generally <50 % thinner than the gold on both bonding pads and the DFB ridges. This is due to the directional nature of metal deposition by evaporation in fabrication process. For GUSTO fabrication, double metal layer were used (550 nm) on the bonding pads

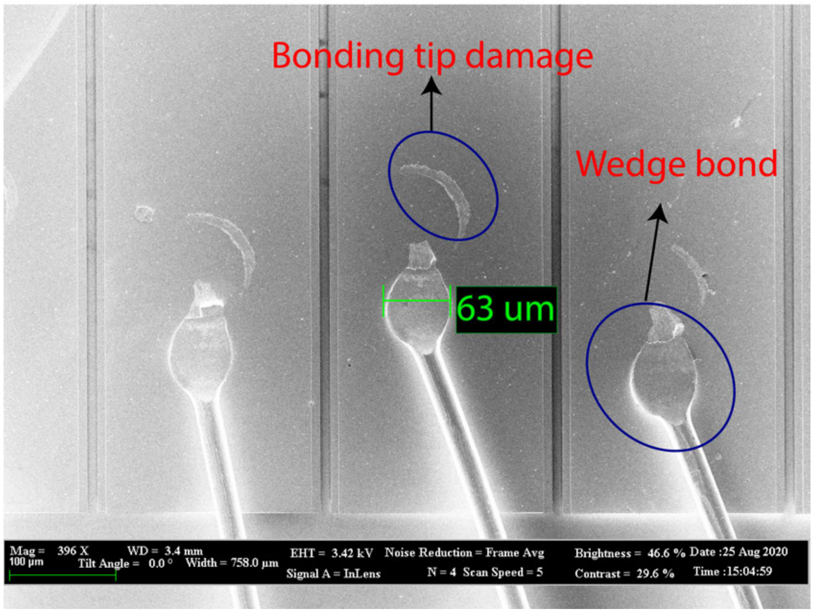

Figure 4-8: Minimization of bonding tip damage by increasing the gold thickness and the bonding pad size.

through two lithography steps. The side view of bonding pads used for GUSTO flight devices are shown in Figure 4-7. As shown in Figure 4-7, by using thicker gold and bonding pads with at least 200 um in width and 700 um in height, the damage is minimized and no further burning was observed at 2W input power (140 mA, 14 V). To further improve the reliability of ISH junction, elliptical profile was used to maximize the junction surface area and minimize the current leakage. The lithography mask for this profile is shown in Figure 4-9

4.8 Wire Bonding Angles

To reduce the wire bond angles, specially when two bonds per pads are required, the spacing between the PCB pads should be ideally equal to the bonding pads on the DFB array die. However, the minimum achievable separation in industrial PCB manufacturing available to us was 76 μm , which is higher than the spacing between DFB array bonding pads (10 μm). Therefore, some bonding angles are unavoidable.

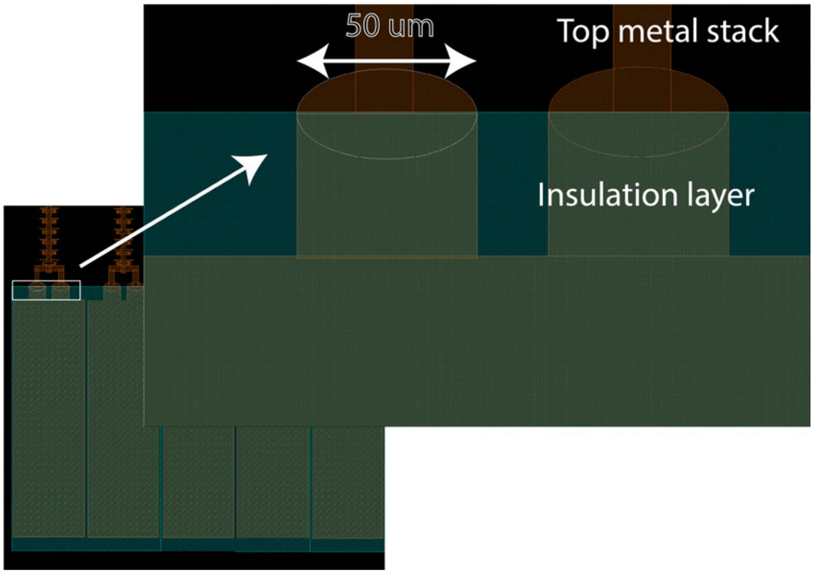

Figure 4-9: Elliptical profile for ISH junction. Two arms are used to connect the bonding pad to the laser ridges to divide the current passing through each junction.

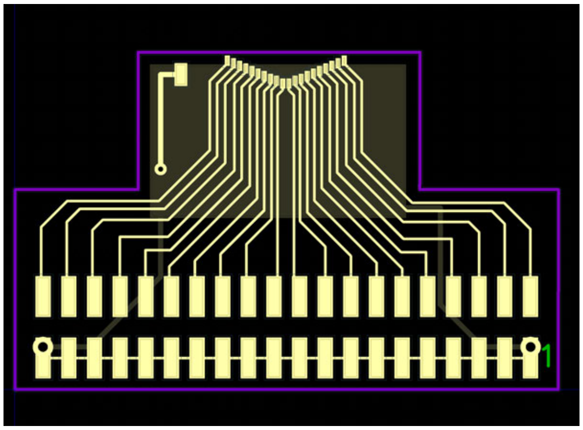

Figure 4-10: PCB with 76 μm pad spacing for minimization of bonding angles.

Figure 4-10 suggests a design which can minimize such angles. By properly wire bonding through the edges of the PCB pads, the bonding angles can be effectively minimized. For GUSTO, The required PCB class is IPC-6012D-Class 3. Using 75 micro inch of soft bondable gold, reliable wire bonding was obtained on the PCB.

4.9 Lithography

Tantalum was used as an adhesion layer because of its lower optical loss at THz [19]. However, to improve the adhesion, thick tantalum film (> 150 A) is often required.

During the evaporation of tantalum film, the relatively high temperature can locally burn the photoresist and cause lift off issues. Since the periodicity adjustment is only 30 nm, any issue at lift off destroys the geometry relation between neighbour devices. For GUSTO devices, two layers of PMGI SF5 (baked at 230 C each for 6 mins) and one layer of SPR700 (baked at 95 c for 6 mins), 165 $\frac{mJ}{cm^2}$ exposing at 375 nm, and 75 seconds developing in CD-26 developer provided a reliable lift off for metal stack $<$ 300 nm.

Chapter 5

High Power Portable Terahertz Laser Systems

5.1 Introduction

The THz spectral range (roughly 1-10 THz) is a fertile ground for many applications [22]. THz spectral range has historically been underdeveloped, as it lies in the gap between frequency ranges that are easily accessible with conventional semiconductor devices. At the low end, electronic devices such as transistors and frequency multipliers work well, but their power levels drop off precipitously above ≈1 THz. Higher frequencies can be accessed by conventional semiconductor photonic devices such as diode lasers, but they are limited to >10 THz by the minimum bandgap energy of semiconductor host materials. Hence the so-called THz gap at ≈1-10 THz. THz QCLs is a promising platform to bridge this gap [8]. However, the demanding cooling requirements for THz QCLs have been a showstopper for achieving compact and portable systems, and they have confined THz QCL systems to a laboratory environment. Therefore, raising the maximum operating temperature to above that of a compact cooler (>235 K for single-stage thermoelectric coolers), or even no cooler at all, has been a paramount long-term goal in the field.

5.2 Historical Development

After the initial rapid increase of THz QCL during 2002-2005 progress slowed [8, 12], eventually stalling in 2012 where the record remained at 200 K [15] until 2019, when $T_{\max}$ =210 K was achieved [16]. This slow and stagnant improvement of $T_{\max}$ begs the question whether there is a fundamental physical reason that THz QCLs cannot be operated significantly above 200 K. During the long stretch from 2002-2018, all the records were achieved using GaAs/AlGaAs active regions with relatively low barriers of $Al_{0.15}Ga_{0.85}As$. In an insightful exploration [106], it was suggested that carrier leakage over these barriers becomes dominant at high temperatures. To suppress this leakage, higher barriers with aluminum composition greater than 15% are needed. Previously, only scattered efforts were made to explore these taller barriers, but they all yielded inferior $T_{\max}$ compared to devices made with $Al_{0.15}Ga_{0.85}As$ as barriers. The prevailing conclusion then was that the increased alloy and interface roughness scattering associated with taller barriers was detrimental to device performance, and therefore barriers with higher aluminum (Al) composition should be avoided. Later, it was found that these tall barrier devices had a previously overlooked leakage channel at elevated temperatures via their higher bound state(s) [107]. By engineering to minimize this leakage channel, devices with $Al_{0.3}Ga_{0.7}As$ barriers yielded desirable nonlinear current-voltage characteristics (distinguished by a negative differential resistance (NDR)) even at room temperature. All the previous THz QCLs showed almost linear current-voltage characteristics at room temperature, suggesting many leakage channels being activated. The works [106, 107] led to the question of the validity of all the previous modeling and simulation studies, in which a clean n-level is assumed where n is the number of subbands involved in the electron transport process and often with the upper lasing level being the highest level. In the works [106, 107], it was also shown that higher-lying leakage channels may be activated at elevated temperatures. Following the works [106, 107] our strategy has been to design structures to be as close to a clean n-level system as possible. This design strategy has led to the significant increase of $T_{\max}$ in the present work. It is well known in the field of THz QCLs that a diagonal structure, in which the upper- and lower-level wavefunctions are spatially separated, is necessary to reduce the scattering of hot tail of electron distribution at elevated temperatures and therefore achieve a high $T_{\max}$. However, higher carrier concentrations are then needed to compensate for the reduced oscillator strength in such diagonal structures [108]. These higher doping levels cause a significant band bending due to the charging effect – something that was largely ignored previously. A solution to mitigate the adverse charging effect is to relax the double-resonance constraint of the resonant-phonon scheme [9] by using a direct-phonon scheme. In this scheme, the depopulation of the lower lasing level takes place by direct LO-phonon scattering to a ground state, without the aid of an extraction level. The direct-phonon depopulation of the lower lasing level is not impacted by the band misalignment caused by higher doping levels, and it has an additional advantage of being insensitive to dephasing caused by interface roughness and impurities. This scheme was explored more than 10 years ago and yielded the simplest QCL structure, involving only two wells per module [109, 110]. The achieved $T_{\max} \approx 125$ K, however, was far inferior to the state-of-the-art at the time (≈186 K) so this approach was not pursued again until recently. By increasing the height of injection barrier to $Al_{0.3}Ga_{0.7}As$ in order to block the aforementioned over-the-barrier leakage channel, was increased by ≈ 50 K to ≈ 173 K [111]. Similar reduction of thermal leakage led to a successful demonstration of room temperature operation of GaAs-based infrared QCL around 9 μm [112]. In hindsight after ref [106], it is clear that carrier leakage over the barriers in those 2-well structures is more significant than in the prevailing resonant-phonon structures, because of a much higher bias electric field associated with a shorter module. Connecting all the dots, it becomes clear that a direct-phonon scheme based on barriers taller than $Al_{0.15}Ga_{0.85}As$ should be the direction to follow in order to break the enduring logjam. This is what was pursued in several recent reports [16, 113, 114] as well as in the present work.

5.3 Band Structure Calculation

The most fundamental tool in the design of THz QCL structures and analysis is a numerical package to calculate subband wavefunctions and energies. In this chapter, the k·p method is employed to calculate electronic states in semiconductor heterostructures based on the envelope function description. The electronics states can be described by the 8-band k·p Kane Hamiltonian (which includes conduction, light-hole, heavy-hole, and split-off bands and their spin interactions). Here we follow the formulation in ref [115]. Assuming that z is the growth direction of quantum wells, with the approximation that in-plane momentum vector is negligible $k_x, k_y \approx 0$, the heavy-hole band is decoupled from the other valance bands. This results in two equivalent 3×3 Hamiltonians for each spin configurations. After these simplifications, the Hamiltonian reads as:

$$\begin{pmatrix} E_c(z) & \sqrt{\frac{2}{3}\frac{p_{cv}}{m_0}}\widehat{p_z} & -\sqrt{\frac{1}{3}\frac{p_{cv}}{m_0}}\widehat{p_z} \\ -\sqrt{\frac{2}{3}\frac{p_{cv}}{m_0}}\widehat{p_z} & E_{lh} & 0 \\ \sqrt{\frac{1}{3}\frac{p_{cv}}{m_0}}\widehat{p_z} & 0 & E_{so} \end{pmatrix}, \ \widehat{p_z} = i\hbar\frac{\partial}{\partial z} \tag{5.1}$$

Hamiltonian in equation 5.1 acts on an envelope vector $\chi = (\chi_c, \chi_{lh}, \chi_{so})$. Here *c* , *lh*, and *so* label the conduction, light-hole, and split-off band edges respectively. With further simplification, χ_c can be derived as follow:

$$\widehat{p_z}\frac{1}{2m(E,z)}\widehat{p_z}\chi + E_c\chi_c = E\chi_c \tag{5.2}$$

in which

$$\frac{1}{m(E,z)} = \frac{1}{m_0}\left[\frac{2}{3}\frac{E_p}{E+E_G} + \frac{1}{3}\frac{E_p}{E+E_G+E_{so}}\right] \tag{5.3}$$

Here E_p is the Kane energy. In this thesis we derive the E_p from the band edge energies as follow

$$E_p(x) = \frac{3m_0}{m^*(x)} = \left[\frac{2}{E_G(x)} + \frac{1}{E_G(x) + E_{so}(x)}\right]^{-1} \tag{5.4}$$

$$p_{cv}(x) = i\sqrt{\frac{m_0 E_p(x)}{2}} \tag{5.5}$$

We have

$$m^*(x) = m_0[0.067(1-x) + 0.15x] \tag{5.6}$$

$$E_{so}(x) = 0.341(1-x) + 0.28x\,\mathrm{eV} \tag{5.7}$$

$$E_c(x) = CBO \times [E_G(x) - 1.515]\,\mathrm{eV} \tag{5.8}$$

Here, CBO is the conduction band offset, E_G is the bandgap, m_0 is the bare electron mass, and x is the aluminum composition in the barrier (here $x = 0.3$). An accurate estimation of band structure requires both E_p and E_c . Here, E_c depends only on the product of bandgap and the conduction band offset. However, E_p depends directly on E_G.

5.4 Optimization of Band Structure

To improve the accuracy of our band structure computations, we accounted for the fact that in THz QCLs with two-well active regions, the alignment of the levels is very sensitive to the conduction band offset in the hetero-structure of $Al_{0.3}Ga_{0.7}As$, and there is no unanimous agreement on the value [116, 17, 117]. Since the lasing frequency can be measured accurately and lasing occurs at the alignment of the injector to the upper level, we used experimental data on lasing frequencies from previously grown structures here at MIT as a figure-of-merit to train a machine-learning model on the band offset for $Al_{0.3}Ga_{0.7}As$. The band gap parameters that were reported in the work ($E_G = 1.515 + 1.403x$) [116] and the fitted band offset of 72 % provided the best predictive results for the lasing frequencies (with $< 2\%$ error). The resulting 1D

wafer	$h\nu$ (sim) meV	$h\nu(exp)$ meV
G528	16.2	16.4
G552	16.0	16.0
G605	15.7	15.7
G652	16.3	16.3
VB745	13.75	13.85
VB747	12.3	11
VB953	18.5	18.2
G529	18.2	17.8

Table 5.1: Comparison between simulated and experimentally measured lasing frequency for QCLs with two-well active regions.

Schrodinger equation was then solved with a standard shooting method. Some of the predicted lasing frequency versus measured frequency for QCLs with two-well active regions are presented in table 5.1. It is worth mentioning that defining E_p based on band edges defined in equation 5.5 provides much more accurate results compared to linear weighted sum of pre-calculated values for GaAs and AlAs.

5.5 Design And Optimization

Figure 5-1 shows the subband probability density functions in a QCL with a two-quantum-well active region design. In this scheme, electrons are injected into the upper laser level of the n^{th} module,$|u_n\rangle$, from the injector level of the preceding module,$|i_{n-1}\rangle$, via resonant-tunneling. The lower lasing level in the n^{th} module,$|l_n\rangle$, is depopulated through longitudinal optical phonon (LO-phonon) scattering into a ground state, $|i_n\rangle$, which also serves as the injector level for the next module. The optical gain in the n_{th} module is due to a population inversion between levels $|u_n\rangle$ and $|l_n\rangle$. In this work, the design is focused to achieve a clean 3-level system. If most of electrons in the n_{th} module remain within those 3 levels ($|u_n\rangle$, $|l_n\rangle$, and $|i_n\rangle$) even at elevated temperatures, then, because of its fast depopulation scattering ($\approx$ 0.2 ps), the lower lasing level $|l_n\rangle$ will be much less populated than $|i_{n-1}\rangle$ and $|u_n\rangle$. Hence a large degree of population inversion between $|u_n\rangle$ and $|l_n\rangle$ can be maintained with

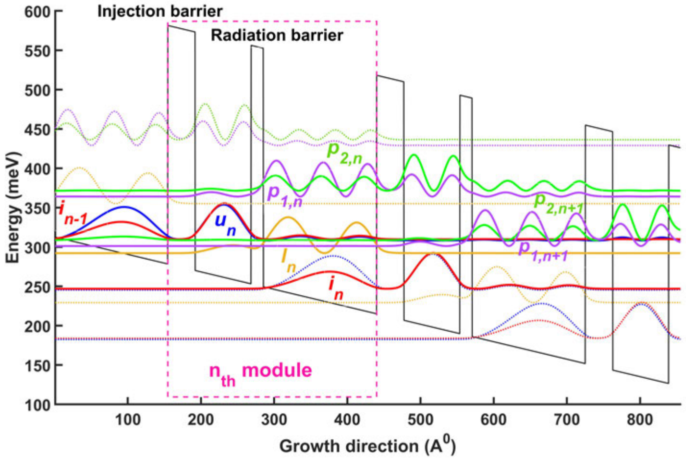

Figure 5-1: Probability density functions of subband states in a THz QCL with two quantum wells per module in the active region (one module is enclosed by the dashed box). Important levels, both the desired 3 levels in one module and levels that may cause carrier leakage, are highlighted with thick lines.

proper designs. There are two main considerations in designing a clean n-level system like this: reducing inter-module tunneling except for the desired $|i_{n-1}\rangle \rightarrow |u_n\rangle$ channel and reducing the coupling to higher lying bound states. Here, we assume with the use of tall barriers, the over-the-barrier leakage can be ignored. Following the works [106, 109, 111] coupling to higher-lying bound states needs to be significantly reduced to achieve a clean 3-level system. The experimental evidence [118] confirms a considerable generation of hot LO-phonons in THz QCLs and further validates the importance of such channels. Accurate knowledge of the band structure (such as conduction band offset and nonparabolicity) is key to minimize parasitic channels, especially those due to undesired inter-module tunneling. Those details are presented in previous section. When the bias is set to align $|i_{n-1}\rangle \rightarrow |u_n\rangle$(injection alignment), a noticeable spatial overlap exists between those two levels and the higher-energy bound states denoted by $|p_{1,n}\rangle$ and $|p_{2,n}\rangle$, as shown in Figure 5-1. At this injection alignment, those higher-energy states form a doublet, which we denote here as $|p_{1,2,n}\rangle$. These states would lie in the continuum for the same scheme with lower barriers [109]. In our band structure engineering, we aimed to minimize the electron-LO-phonon absorption rate into the doublet $|p_{1,2,n}\rangle$ from the $|i_{n-1}\rangle - |u_n\rangle$ levels. This rate depends on the LO-phonon population, the energy separation between $|i_{n-1}\rangle$ and $|p_{1,n}\rangle$ (denoted as $E_{i,pp}$), and the LO-phonon scattering matrix element between the initial and final states. Since the doublet $|p_{1,2,n}\rangle$ is localized, narrower wells will increase the energy separation $E_{i,pp}$, helping to reduce this leakage channel. At the same time, we aimed to maximize the injection strength $|i_{n-1}\rangle - |u_n\rangle$, which is quantified in the tight-binding approach by an anticrossing gap, $\Omega_{i,u}$. The trade-off between reducing leakage channels and increasing injection rate comprises the main part of the design effort. Exploring in this direction, we designed and grew multiple wafers based on $Al_{0.3}Ga_{0.7}As$ barriers with increasing $\Omega_{i,u}$ and $E_{i,pp}$, and reducing oscillator strength $f_{i,pp}$. Here we use the oscillator strength because all scattering mechanisms, including LO-phonon scattering, should decrease at the expense of oscillator strength [119]. To quantify LO-phonon scattering, we use $U_{i,pp}^{\max}$ which is a crude upper bound for LO-Phonon scattering matrix element.

5.6 Optimization Strategy

A useful design tool for minimization of relevant parasitic channels is an anticrossing graph and the anticrossing curves are shown in Figure 5-2 which corresponds to the bands shown in Figure 5-1.This graph shows the level alignments over a wide range of module biases. Minima in anticrossing correspond to a resonant alignment of two levels in energy, and the anticrossing gap is a measure of the coupling strength between those two levels. Because of a strong dephasing rate of 4 meV (corresponding to 1 THz linewidth), the coupling between two levels with anticrossing gap <0.5 meV is not significant. In principle, those levels that align closer to the $|i_{n-1}\rangle \rightarrow |u_n\rangle$ alignment will negatively impact a "clean" 3-level system. The main parasitic channels beside $|i_{n-1}\rangle, |u_n\rangle \rightarrow |p_{1,2,n}\rangle$ are $|i_{n-1}\rangle, |u_n\rangle \rightarrow |p_{2,n+1}\rangle$, and $|l_n\rangle \rightarrow |p_{1,n+1}\rangle$. Here we formulate our optimization problem as the following: $X = [x_1, x_2, x_3, x_4]^T$ is a vector that represents all the barrier and well thicknesses, and the voltage drop per module is denoted by V. The anticrossing gap and the alignment bias between levels $|i\rangle$ and

$|j\rangle$ are defined as:

$$\begin{aligned} V_{i,j}(X) &= \arg\,\min(|E_i(X, V - E_i(X, V|) \qquad (5.9) \\ \Omega_{i,j}(X) &= |E_i(X, V_{i,j}(X) - E_j(X, V_{i,j}(X)| \end{aligned}$$

Here $E_i(X, V)$ is the energy of level $|i\rangle$ at the geometry parameters of X and at bias V. The figure of merit in our optimization problem is:

$$\begin{aligned} &X_{opt} = \arg\,\min(-N_{i,pp}E_{i,pp}(X, V_{i,u}(X)) + N^{W}_{i,pp}f_{i,pp}(X, V_{i,u}(X)) - N_V(V_{i,p_{1,n+1}}(X) - V_{i,u}(X))^2) \\ &V_{\text{design}} = V_{i,u}(X_{\text{opt}}) \end{aligned}$$

subject to

$$\begin{aligned} &0.28 \leq f_{u,l}(X, V_{i,u}(X)) \leq 0.32 \\ &15.5\,\text{meV} \leq E_u(X, V_{i,u}(X)) - E_l(X, V_{i,u}(X)) \leq 16.5\,\text{meV} \\ &\omega^{\text{min}}_{i,u} \leq \omega_{i,u}(X) \leq \omega^{\text{max}}_{i,u} \\ &E_{ex}(X, V_{i,u}(X)) \leq E^{\text{max}}_{ex} \\ &\Omega_{i_{n-1},p_{2,n+1}}, \Omega_{u_n,p_{2,n+1}} \leq 0.5\,\text{meV} \\ &\Omega_{l_n,p_{1,n+1}} \leq 0.9\,\text{meV} \qquad (5.10) \end{aligned}$$

Here, $f_{u,l}$ is the oscillator strength between upper and lower lasing level and is defined as:

$$f_{u,l} = (\frac{2m^*_{\text{GaAs}}e}{\hbar^2})(E_u - E_l)\left|\langle\chi^u_c|\, z \,|\chi^l_c\rangle + \langle\chi^u_{lh}|\, z \,|\chi^l_{lh}\rangle + \langle\chi^u_{so}|\, z \,|\chi^l_{so}\rangle\right|^2 \qquad (5.11)$$

Here, -e is the electron charge, $E_{ex} = E_{l_n} - E_{i_n}$, and $-N_{i,pp}$, $N^W_{i,pp}$, N_V are normalization factors. $f_{i,pp}$ is the oscillator strength between $|i_{n-1}\rangle$ and $|p_{1,n}\rangle$ and is defined in the same way as $f_{u,l}$. The resulting optimization problem was solved using MATLAB fminsearch which is based on a simplex algorithm. For comparison purposes in

Table 5.2, we define an upper bound on phonon scattering matrix element as:

$$U_{i,pp}^{\max} = \int \frac{\int \psi_i(z)\psi_j(z)e^{-Q\left|z-z^{'}\right|}\psi_i(z^{'})\psi_j(z^{'})dzdz^{'}}{Q}dQ \tag{5.12}$$

It is worth mentioning that $U_{i,pp}^{\max}$ is not used directly in our optimization process. This is because all scattering mechanisms, not just LO-phonon scattering, should decrease at the expense of oscillator strength. Therefore, by including $f_{i,pp}$ compared to $U_{i,pp}^{\max}$, we indirectly minimize other scattering mechanisms as well. This can be qualitatively understood by the expansion of a general perturbation Hamiltonian in Fermi's golden rule using Taylor expansion. Assume a position dependent perturbation $H^{'}(z)$ and the matrix element $A_{u,l}$ between between $|u\rangle$ and $|l\rangle$ which reads as:

$$|A_{u,l}|^2 = \left| \int \psi_u(z)H^{'}(z)\psi_l^*(z)dz \right|^2 \tag{5.13}$$

Expanding the $H^{'}(z)$ in Taylor expansion to the first order results in:

$$|A_{u,l}|^2 = \left| \int \psi_u(z)(a + c_1 z)\psi_l^*(z)dz \right|^2 = \text{constant} \times f_{ul} \tag{5.14}$$

This approximation is similar to small momentum exchange in the LO-phonon scattering matrix element. In this case, by expanding $H^{'}(z)$ based on its Fourier transform, we can write:

$$|A_{u,l}(q)|^2 = \left| \int \psi_u(z)e^{iqz}\psi_l^*(z)dz \right|^2 \tag{5.15}$$

For small momentum exchange that is favored in LO-phonon scattering near resonance, we can use the same approximation in Taylor expansion and approximate $|A_{u,l}(q)|^2$ as:

$$|A_{u,l}(q)|^2 \leq |q|^2 \left| \int \psi_u(z)z\psi_l^*(z)dz \right|^2 = \text{constant} \times f_{ul} \tag{5.16}$$

Therefore, by minimization of oscillator strength, in principle, we also indirectly minimize scattering through other scattering mechanisms.

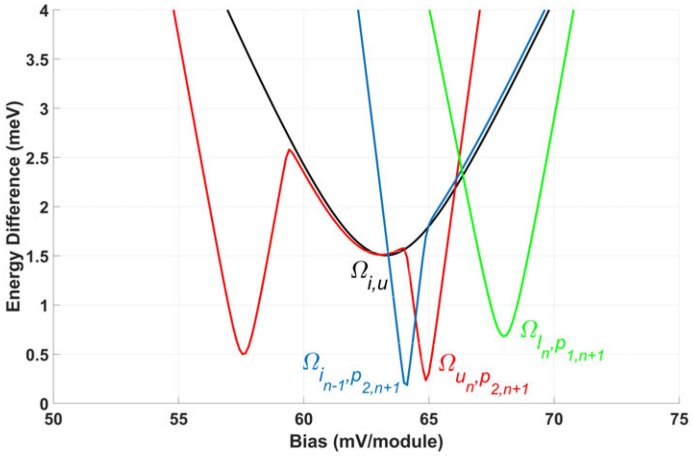

Figure 5-2: Anticrossing graph highlighting three additional parasitic channels $|i_{n-1}\rangle$, $|u_n\rangle \rightarrow |p_{2,n+1}\rangle$, $|l_n\rangle \rightarrow |p_{1,n+1}\rangle$.

5.7 Experimental Demonstration

The experimental and simulated results for this optimization process are presented in Table 5.2. Figure 5-3 shows the measured electrical and optical characteristics of a device fabricated from G652 wafer, which lased up to 250 K. As shown in the inset of Figure5-8a for G652 exhibits no deviation from an exponential increase. Even though an exponential $J_{th} - T$ behavior is purely empirical, in THz QCLs J_{th} often increases faster than exponential at the higher end, suggesting leakage channels are activated at those temperatures. The J-V curves in Figure 5-3b also show NDR up to room temperature. The combination of these two features, exponential $J_{th} - T$ and room-temperature NDR, suggests that no significant leakage channels are activated, at least up to $T_{\max}$. As shown in Table 5.2, increasing $\Omega_{i,u}$ and $E_{i,pp}$ and reducing $f_{i,pp}$ largely leads to progressive improvement. The only exception is between G605 and G552. Even though both G605 and G552 have similar energy separation with the doublet $|p_{1,2,n}\rangle$ and both show NDR at room temperature, G605 did poorly compared to G552. These two structures were nearly identical, except that the injection barrier was made thinner in G605 to increase the anticrossing gap $\Omega_{i,u}$, in order to increase $J_{\max}$ and therefore the gain. However, the injection barrier thickness does not only affect the injector anticrossing gap $\Omega_{i,u}$, it also affects the coupling with other parasitic

Wafer	$E_{i,pp}$ meV	$f_{i,pp}$	$U_{i,pp}^{\max}$	$\approx h\nu$ meV	$\Omega_{i,u}$ meV	$J_{\max}$ $\frac{\text{kA}}{\text{cm}^2}$	J_{th} $\frac{\text{kA}}{\text{cm}^2}$	$f_{u,l}$	$T_{\max}$ (K)	Layer sequence A°
G528	54.3	0.25	1	16.4	1.50	1.60	0.80	0.30	192	**37.4**,76.4,**16.7**,154.7
G552	53.2	0.16	0.94	16.0	2.14	2.67	1.48	0.29	235	**33.0**,76.3,**17.5**,153.8
G605	53.0	0.2	1.1	15.7	2.41	2.87	1.75	0.30	225	**31.4**,76.3,**17.5**,153.1
G652	58.1	0.14	0.8	16.3	2.30	2.60	1.54	0.29	250	**33.7**,72.0,**18.7**,144.9

Table 5.2: Simulation and experimental results of four THz QCLs. $E_{i,pp}$ is the energy spacing between the injector and the doublet $|p_{1,2,n}\rangle$, $h\nu$ is the measured lasing frequency, $J_{\max}$ is the maximum current density, J is the threshold current density, and f_{ul} is the oscillator strength between the upper and lower lasing levels, f_{ul} and $U_{i,pp}^{\max}$ are are the oscillator strength and an upper bound on LO-phonon scattering matrix element between $|i-1\rangle$ and $|p_{1,n}\rangle$. Here $U_{i,pp}^{\max}$ is normalized to G528 wafer. Layer sequences start from the injection barrier. Bold denotes $Al_{0.3}Ga_{0.7}As$ barriers separating GaAs quantum wells. The underline indicates the doped well, with a volume doping of $1.5 \times 10^{17}\,\text{cm}^{-3}$ in the central 30-A° region. Wafers, which are listed in the first column of this table are based on the designs TB1WI350-DesA2 (for G528), TB1WI356-DesA2V2 (for G552), TB1WI356-DesA2V3 (for G605), and TB1WI371-DesA2V6 (for G652), respectively. Here the number after 'TB1WI' (standing for "Tall-Barrier 1-Well Injector") in the design name indicates the number of modules. The number of modules is chosen for ≈ 10 μm of active region.

channels denoted by $|p_{1,n+1}\rangle$, $|p_{2,n+1}\rangle$ in Figure 5-1. The reason for degradation from G552 to G605 appears to be two-fold. First, there is an increased coupling between the lower-lasing level $|l_n\rangle$ and a parasitic channel $|p_{1,n+1}\rangle$ (quantified by an anticrossing gap $\Omega_{ln,p_{1,n+1}} > 1$ meV) and a reduced bias separation ($V_{l_n,p_{1,n+1}} - V_{i,u}$)between this alignment and the injection alignment as shown in Figure 5-4. Increasing $V_{l_n,p_{1,n+1}} - V_{i,u}$ cause higher $E_{p_{1,n+1}} - E_{l_n}$at $V_{i,u}$(7.4 meV for G552 and 6.7 meV for G605) Although this channel may appear to help to depopulate the lower-lasing level, it introduces additional levels beyond the desired 3 levels into the transport process and leads to a net detrimental effect. Second, the thinner injection barrier slightly increases the oscillator strength between $|i_{n-1}\rangle$ and $|p_{1,n}\rangle$. As the electron-LO-phonon scattering rate (and other scattering mechanisms) depends on both energy separation and the scattering matrix element, such increase will increase the scattering rate into the parasitic channel $|p_{1,2,n}\rangle$. As it is shown in Table 5.2, $U_{i,pp}^{\max}$ is higher for G605 compared to G552. These parasitic channels may explain the worse performance of G605, which would emphasize how important it is to minimize the involvement of other levels in the transport process and maintain a clean 3-level system. It is worth mentioning that

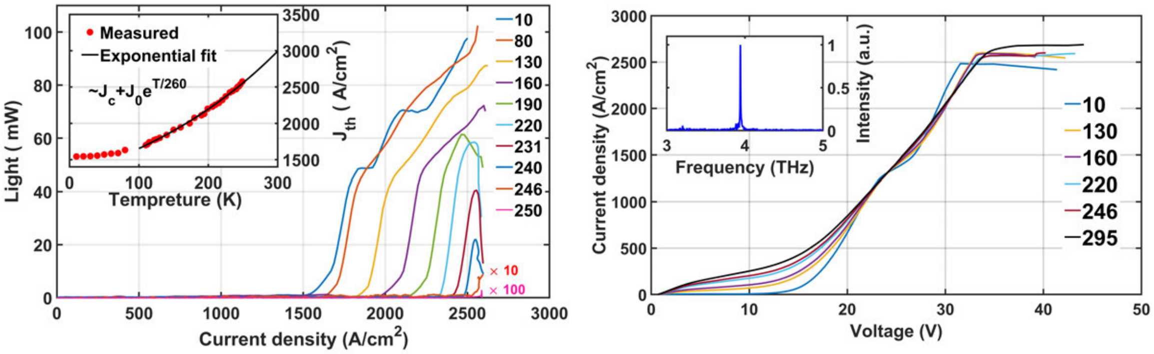

(a)

(b)

Figure 5-3: Optical and electrical characterization of a device fabricated from wafer G652 with dimensions 1.23 mm× 150μm, biased with 400-ns pulse width at 500 Hz. (a), THz power vs. current density at different temperatures and the inset shows the threshold current density vs. temperature ($J_{th} - T$) along with an exponential fit. (b), Voltage vs. current density (J-V). The inset shows a lasing spectrum taken at 246 K. Note there is no deviation from an exponential fitting in $J_{th} - T$ all the way up to $T_{\max}$ and NDR is preserved at room temperature. Both are telltale signs that there are no significant leakages in the 3-level system.

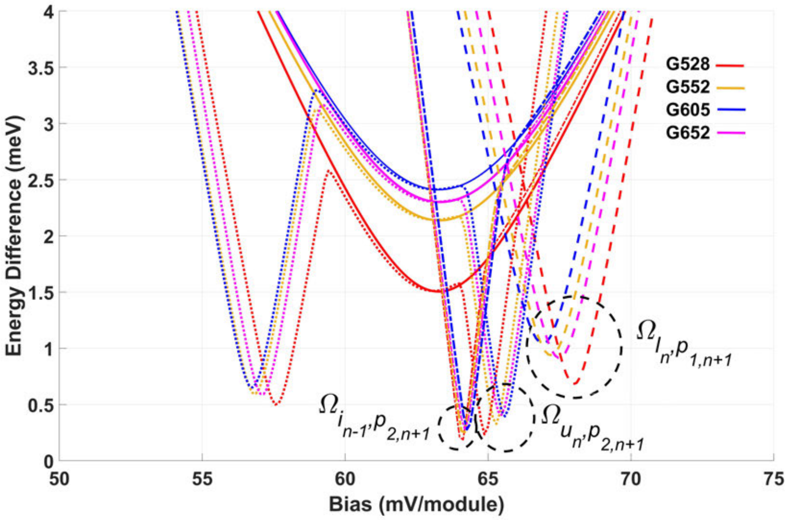

Figure 5-4: Anticrossing graph for the four grown wafers and the parasitic channels. $|i_{n-1}\rangle\,, |u_n\rangle \rightarrow |p_{2,n+1}\rangle$, $|l_n\rangle \rightarrow |p_{1,n+1}\rangle$.

the radiation barrier thickness also plays an important role in the leakage to $|p_{1,2,n}\rangle$. Increasing the radiation barrier thickness can further reduce the leakage to parasitic channels but it will reduce the oscillator strength and therefore gain. It is known that the optimum diagonality (quantified by the oscillator strength) is not universal but depends on the specific structure. Finally, while the $T_{\max}$ trends can be explained by design choices, it should be noted that there may be other factors at play. The quality of the underlying molecular beam epitaxy (MBE) growth can impact the final device performance, and it remains unclear how significant this effect is. By one key metric – the stability of the superlattice period – we observe exceptionally good growth quality for the top-performing structures in this work with $T_{\max} > 220K$ [120]. It is possible, then, that there is some correlation between growth stability and $T_{\max}$, although this is clearly not the only factor since the highest $T_{\max}$ was achieved in the growth with only second-best stability (G652). We anticipate that both high quality MBE growth and careful structure design will be essential ingredients for the further development of high-performance THz QCLs.

It is instructive to compare the $J_{th} - T$ between G652 and G552 as is shown in Figure 5-5. Though G652 has higher injection anticrossing compared to the G552 and in principle has more leakage from injector to the lower lasing level, the rate of increase in J_{th} with temperature is slower for G652. Considering the similarity in other relevant transport parameters(i.e. oscillator strength, lasing frequency), such slower rate of increase in J_{th} with temperature indicates a lower leakage from injector-upper lasing level doublet and can be explained by higher $E_{i,pp}$ and lower $f_{i,pp}$ in G652 as compared to G552.

5.8 Thermoelectric Cooling and THz Imaging

The high temperature performance of G652, which far exceeds a decade-old record of 225 K that was achieved with an impractical strong (up to 30 T) magnetic field [121], opens the door to applications that were previously unattainable. A maximum lasing temperature around 196-210 K already enabled the use of compact and portable

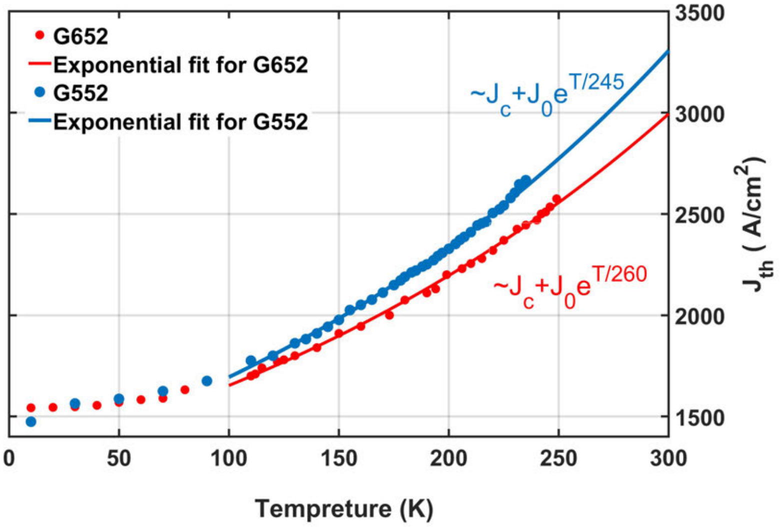

Figure 5-5: $J_{th} - T$ comparison between G652 and G552.

thermoelectric coolers (TECs) [16, 122] instead of bulky cryogenics. However, as $T_{\max}$ being close to the cooling floor of multistage TEC, the output power is not sufficient for real-time imaging applications. In the present work, the maximum operating temperature has been increased significantly to 250 K. Importantly for applications, this high $T_{\max}$ yields much greater average output powers in the range ≈210-240 K, which is within the cooling range of commercial TECs. This enables compact THz lasers with sufficient power for real-time imaging and fast spectral measurements using room-temperature cameras and detectors. To demonstrate this, we operated a QCL based on G652 at 235 K, cooled by a single-stage commercial TEC. The laser was operated in pulsed mode (1% duty cycle, 100 ns pulse at 100 kHz), and it generated ≈2 W of heat. By using a TEC module with only one stage (Laird systems, model ZT6-7-F1-3030-TA-W8), the entire assembly could be kept small. At the same time, it cooled the laser enough that it could supply a sufficient level of output power to perform fast spectral measurements without requiring an especially high-performance detector. The assembled chamber is shown in Figure 5-7. The lasing spectrum of this single-stage TEC-cooled laser was measured using a pyroelectric detector with a noise equivalent power (NEP) of $\approx 460\frac{pW}{\sqrt{Hz}}$, and with only several seconds of integration time. The L-I curve was also measured using the

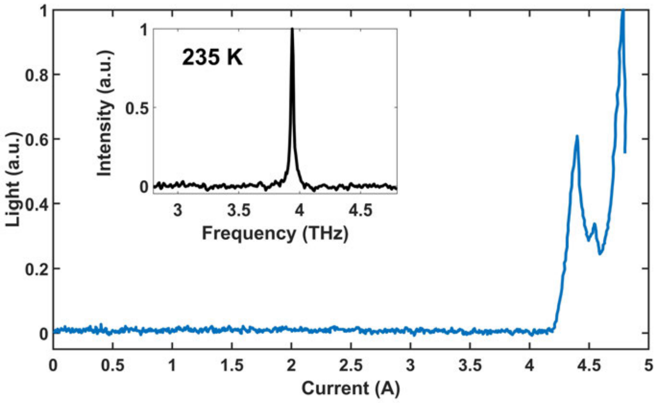

Figure 5-6: Output power vs. current measurements of a TEC-cooled THz QCL device using a room-temperature pyroelectric detector. The inset shows the lasing spectrum. Both measurements were performed using a single-stage TEC at temperature of 235 K.

same detector, and it is shown in Figure 5-6. Using these high-temperature THz QCLs, following the work [77] that was performed with a thermomechanical cooler at 33 K, we have also demonstrated a portable THz imaging system. Real-time imaging measurements using a THz camera (manufactured by NEC with a NEP in the range of $\approx 50\frac{pW}{\sqrt{Hz}}$) require much higher average power levels than the spectral measurements. Thus, a 3-stage TEC (Laird systems, model MS3-119-20-15-11-W8) was used – housed in the same vacuum chamber but with an external single-stage TEC module (TE Technology, Inc, model CP-200HT)– to achieve a 2 W heat removal capacity and operating temperatures down to 210 K.The average output power was sufficient so that the laser beam could be imaged with a 320×240 THz focal-plane array camera with 32-frame averaging (integration time 2 s). The overall assembly is shown in Figure 5-8b. The captured beam patterns are shown in Figure 5-9 at different operating temperatures from 210 K up to 235 K.

In conclusion, by carefully designing QCL structures to reduce carrier leakage channels at elevated temperatures, we have developed THz QCLs (at ≈4 THz) with a maximum operating temperature $T_{\max} = 250$ K. This operating temperature enabled the construction of coherent THz radiation sources using commercial (<100 $) single- and multi-stage thermoelectric coolers, yet with power levels sufficient for real-time imaging of beam pattern and fast spectral measurements without requiring expensive

Figure 5-7: Single stage fan-cooled TEC assembly with 4.5” diameter and 6” height. A pulse tube cooler which is commonly used in a laboratory environment is also shown in the background without showing the required pumps and Helium compressor. The hole spacing on the optical table is 1 inch.

cryogenically cooled detectors. The combination of TEC-cooled THz QCLs with room-temperature cameras and detectors enables portable systems that are operable outside the laboratory environment. Furthermore, and perhaps more importantly, the demonstrated significant increase in $T_{\max}$ and the preservation of room-temperature NDR pave a clear path toward further increases in $T_{\max}$: designing clean n-level systems based on the direct-phonon scheme with tall barriers.

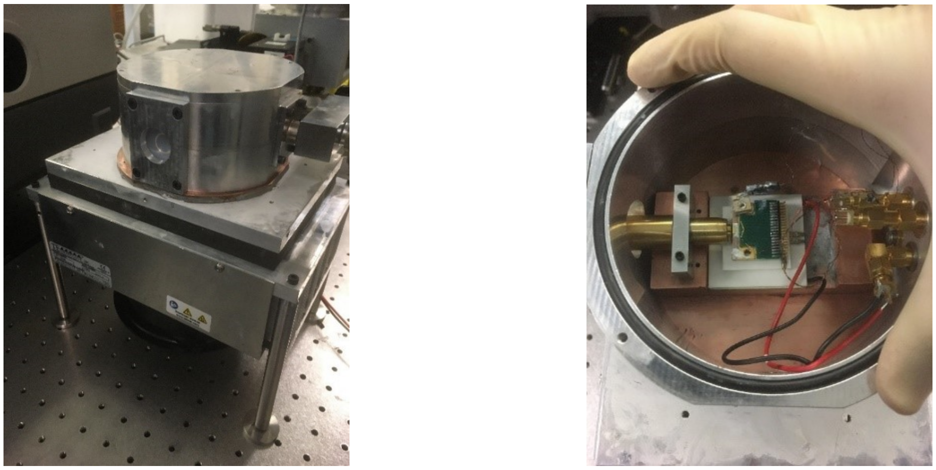

(a) (b)

Figure 5-8: Four-stage TEC with 3 stages inside a vacuum chamber and a single stage outside to stabilize the heat-sink temperature. (a), An exterior picture of the final assembly. (b), QCL chip and an outcoupling Winston cone is shown. The hole spacing on the optical table is 1 inch.

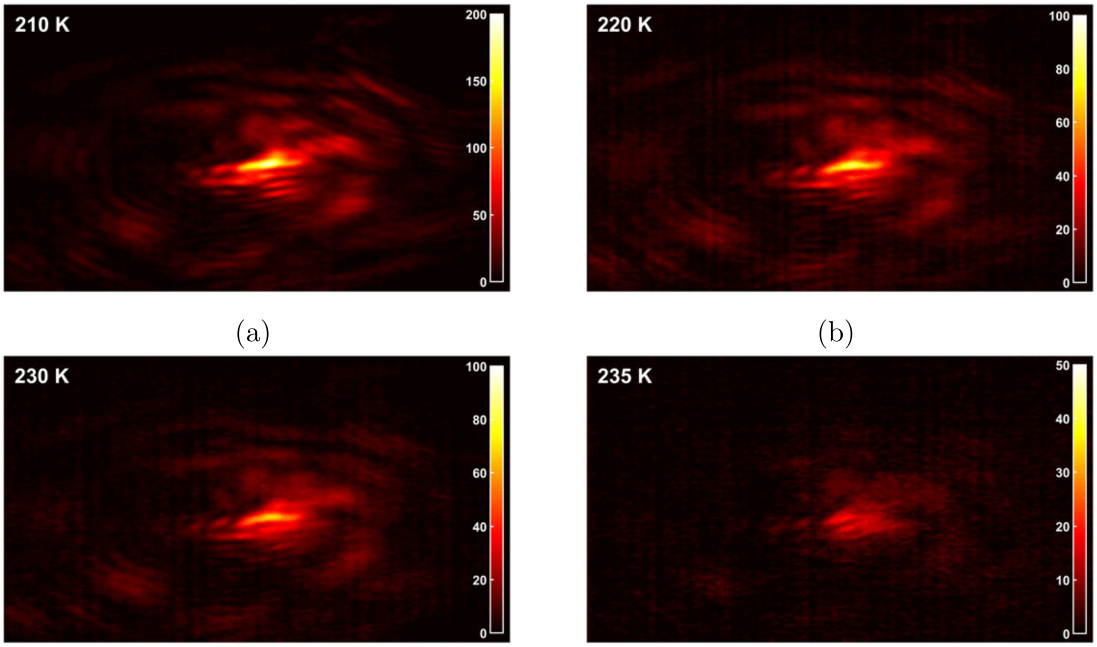

(a) (b)

(c) (d)

Figure 5-9: Beam pattern images taken with a room-temperature 320×240 camera at progressively higher temperature maintained by a 3-stage TEC. ((a), 210 K, (b), 220 K, (c), 230 K, and (d), 235 K.) The ripples in the beam pattern are created by a combination of multiple spatial modes created in the Winston cone out-coupler along with diffraction from the subwavelength laser size in the transverse directions.

5.9 Earlier Designs With Two-Well Active Region and $Al_{0.3}Ga_{0.7}As$ Barriers

Prior to the work in this thesis, in which the extensive investigation to identify the correct parameter of the conduction-band offset (CBO) was prompted by consistent wrong lasing frequency prediction of QCLs with tall barriers, the band structure solver was developed based on finite difference method by Ivan Chan [19]. This solver was used for all prior designs based on tall barriers from 2009-2017. In this solver, for designs based on tall barriers, Vurgaftman's parameters was used for bandgap and conduction band offset [17]. On the other hand, for lower barriers, Williams's parameters [18] for conduction band offset was used in conjunction with the band gap parameters from Vurgaftman. The comparison between the parameters used in this thesis and those mentioned in Ivan chan's thesis [19] is presented in Figure 5-10. A summary of QCLs with two well active region, which were designed based on finite difference method using Vurgaftman's parameters is shown in Table 5.3. In Table 5.3 all the parameters were computed using the CBO parameter and the method in this work, as described earlier. As shown in Table 4.3, when using the corrected CBO parameter, the computed lasing frequencies and oscillator strengths are far off from the intended 16 meV and 0.2, resulting in inferior results and sometimes even nonlasing devices. The failure of VB721,VB722,VB724, and VB727 is mainly due to the wrong bandstructre used for designing these wafers specially energy spacing of upper and lower lasing levels. Compared to G652 which has $f_{ul} \approx .3$, the oscillator strength of all prior designs were too low causing reduction in gain and poor temperature performance. VB747 and VB745 have comparable $E_{i,pp}$ compared with G552 which lased up to 235 K. The room temperature NDR in these lasing devices also indicates the suppressed leakage to the higher level states ($|p_{1,2,n}\rangle$) due to increased E_i, pp. However, The low injection efficiency and extreme diagonality ($f_{ul} < 0.1$) can explain the lower gain and consequently inferior lasing temperature as compared to G528 ($f_{ul} \approx 0.3$). The poor performance of these wafers also emphasise that a clean three level system is only a necessary condition to achieve high $T_{\max}$

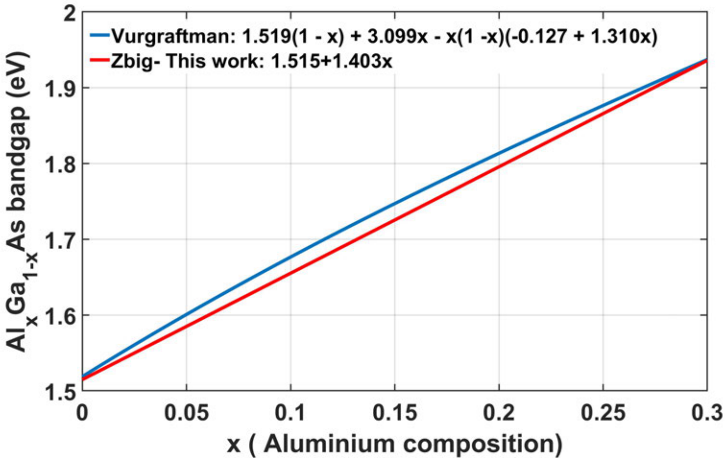

(a)

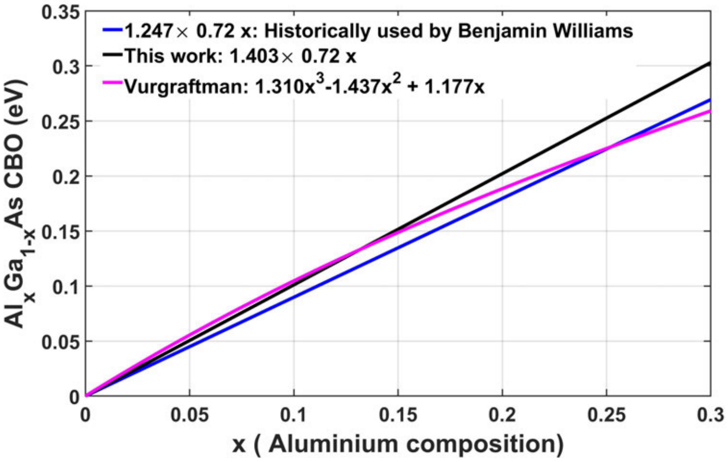

(b)

Figure 5-10: Band structure parameters used in k.p model in this thesis compared to[17, 18, 19]. (a) Bandgap, (b) Conduction band offset.

Wafer	Design	$E_{i,pp}$ meV	simulated $h\nu$ meV	experimental $h\nu$ meV	$\Omega_{i,u}$ meV	$f_{u,l}$	$T_{\max}$ K	Layer sequence A°	Average 3D doping cm^{-3}
VB721	TW313K-M1	46	10.74	-	1.86	0.086	no lasing	**27**,89,**31**,$\underline{173}$	4.69e16
VB722	TW309K-M3	47	8.5	-	1.79	0.079	no lasing	**29**,91,**31**,$\underline{173}$	6.94e16
VB724	TW304K-M4	43	3.2	-	1.75	0.23	no lasing	**30**,97,**29**,$\underline{173}$	1.37e17
VB727	TW311K-M2	47.7	7.5	-	1.74	0.14	no lasing	**31**,92,**26**,$\underline{173}$	9.13e16
VB745	TW313K-M1	47	13.75	13.85	1.66	0.08	104 (RNDR)	**34**,84,**27**,$\underline{168}$	9.38e15
VB781	TW304K-M1	37	14	-	2.12	0.1	no lasing	**28**,92,**23**,$\underline{186}$	9.12e15
VB953	TW354L-M5	55.3	18.5	18.2	1.42	0.2	80	**40**,72,**20**,$\underline{150}$	8.18e15
VB747	TW354K-M3	63.2	12.3	11	1.75	0.08	134 (RNDR)	**38**,72,**31**,$\underline{142}$	9.12e15

Table 5.3: Performance of earlier designs based on one well injector and 30 % barriers grown during 2015-2019. Room temperature NDR is denoted by RNDR. Layer sequences start from the injection barrier. Bold denotes $Al_{0.3}Ga_{0.7}As$ barriers separating GaAs quantum wells. The underline indicates the doped well. The thickness of active region is 10 μm for all the wafers.

Bibliography

[1] https://www.nasa.gov/missionpages/sofia/index.html.

[2] John F Federici, Brian Schulkin, Feng Huang, Dale Gary, Robert Barat, Filipe Oliveira, and David Zimdars. Thz imaging and sensing for security applications—explosives, weapons and drugs. *Semiconductor Science and Technology*, 20(7):S266, 2005.

[3] Anis Rahman, Aunik K Rahman, and Babar Rao. Early detection of skin cancer via terahertz spectral profiling and 3d imaging. *Biosensors and Bioelectronics*, 82:64–70, 2016.

[4] Nathan M Burford and Magda O El-Shenawee. Review of terahertz photoconductive antenna technology. *Optical Engineering*, 56(1):010901, 2017.

[5] Christopher W Berry, Mohammad R Hashemi, and Mona Jarrahi. Generation of high power pulsed terahertz radiation using a plasmonic photoconductive emitter array with logarithmic spiral antennas. *Applied Physics Letters*, 104(8):081122, 2014.

[6] Jose V Siles, Ken B Cooper, Choonsup Lee, Robert H Lin, Goutam Chattopadhyay, and Imran Mehdi. A new generation of room-temperature frequency-multiplied sources with up to 10× higher output power in the 160-ghz–1.6-thz range. *IEEE Transactions on Terahertz Science and Technology*, 8(6):596–604, 2018.

[7] Quanyong Lu and Manijeh Razeghi. Recent advances in room temperature, high-power terahertz quantum cascade laser sources based on difference-frequency generation. In *Photonics*, volume 3, page 42. Multidisciplinary Digital Publishing Institute, 2016.

[8] Rüdeger Köhler, Alessandro Tredicucci, Fabio Beltram, Harvey E Beere, Edmund H Linfield, A Giles Davies, David A Ritchie, Rita C Iotti, and Fausto Rossi. Terahertz semiconductor-heterostructure laser. *Nature*, 417(6885):156–159, 2002.

[9] Benjamin S Williams, Hans Callebaut, Sushil Kumar, Qing Hu, and John L Reno. 3.4-thz quantum cascade laser based on longitudinal-optical-phonon scattering for depopulation. *Applied Physics Letters*, 82(7):1015–1017, 2003.

[10] Giacomo Scalari, Lassaad Ajili, Jérôme Faist, Harvey Beere, Edmund Linfield, David Ritchie, and Giles Davies. Far-infrared (λ 87 μ m) bound-to-continuum quantum-cascade lasers operating up to 90 k. *Applied Physics Letters*, 82(19):3165–3167, 2003.

[11] Benjamin S Williams, Sushil Kumar, Hans Callebaut, Qing Hu, and John L Reno. Terahertz quantum-cascade laser operating up to 137 k. *Applied Physics Letters*, 83(25):5142–5144, 2003.

[12] Benjamin S Williams, Sushil Kumar, Qing Hu, and John L Reno. Operation of terahertz quantum-cascade lasers at 164 k in pulsed mode and at 117 k in continuous-wave mode. *Optics Express*, 13(9):3331–3339, 2005.

[13] Mikhail A Belkin, Jonathan A Fan, Sahand Hormoz, Federico Capasso, Suraj P Khanna, Mohamed Lachab, A Giles Davies, and Edmund H Linfield. Terahertz quantum cascade lasers with copper metal-metal waveguides operating up to 178 k. *Optics express*, 16(5):3242–3248, 2008.

[14] Sushil Kumar, Qing Hu, and John L Reno. 186 k operation of terahertz quantum-cascade lasers based on a diagonal design. *Applied Physics Letters*, 94(13):131105, 2009.

[15] S Fathololoumi, E Dupont, CWI Chan, ZR Wasilewski, SR Laframboise, D Ban, A Mátyás, C Jirauschek, Qing Hu, and HC Liu. Terahertz quantum cascade lasers operating up to 200 k with optimized oscillator strength and improved injection tunneling. *Optics express*, 20(4):3866–3876, 2012.

[16] Lorenzo Bosco, Martin Franckié, Giacomo Scalari, Mattias Beck, Andreas Wacker, and Jérome Faist. Thermoelectrically cooled thz quantum cascade laser operating up to 210 k. *Applied Physics Letters*, 115(1):010601, 2019.

[17] I Vurgaftman, J áR Meyer, and L áR Ram-Mohan. Band parameters for iii–v compound semiconductors and their alloys. *Journal of applied physics*, 89(11):5815–5875, 2001.

[18] Benjamin S Williams, Williams. *Terahertz quantum cascade lasers*. PhD thesis, Massachusetts Institute of Technology, 2003.

[19] Chun Wang Ivan Chan. *Towards room-temperature terahertz quantum cascade lasers: Directions and design*. PhD thesis, Massachusetts Institute of Technology, 2015.

[20] Alexander GGM Tielens. *The physics and chemistry of the interstellar medium*. Cambridge University Press, 2005.

[21] A Giles Davies, Andrew D Burnett, Wenhui Fan, Edmund H Linfield, and John E Cunningham. Terahertz spectroscopy of explosives and drugs. *Materials today*, 11(3):18–26, 2008.

[22] Daniel M Mittleman. Twenty years of terahertz imaging. *Optics express*, 26(8):9417–9431, 2018.

[23] Anthony J Fitzgerald, Vincent P Wallace, Richard Pye, Mercedes Jimenez-Linan, Lynda Bobrow, Anand D Purushotham, and Donald D Arnone. Terahertz imaging of breast cancer, a feasibility study. In *Infrared and Millimeter Waves, Conference Digest of the 2004 Joint 29th International Conference on 2004 and 12th International Conference on Terahertz Electronics, 2004.*, pages 823–824. IEEE, 2004.

[24] Leila H Eadie, Caroline B Reid, Anthony J Fitzgerald, and Vincent P Wallace. Optimizing multi-dimensional terahertz imaging analysis for colon cancer diagnosis. *Expert Systems with Applications*, 40(6):2043–2050, 2013.

[25] Juraj Darmo, Vincas Tamosiunas, Gernot Fasching, Josef Kröll, Karl Unterrainer, Mattias Beck, Marcella Giovannini, Jerome Faist, Christian Kremser, and Paul Debbage. Imaging with a terahertz quantum cascade laser. *Optics express*, 12(9):1879–1884, 2004.

[26] Paraskevas Bakopoulos, I Karanasiou, Nikos Pleros, Panagiotis Zakynthinos, Nikolaos Uzunoglu, and Hercules Avramopoulos. A tunable continuous wave (cw) and short-pulse optical source for thz brain imaging applications. *Measurement Science and Technology*, 20(10):104001, 2009.

[27] Cheon Hwayeong, Jin Ho Paik, Choi Moran, Yang Hee-Jin, and Son Joo-Hiuk. Detection and manipulation of methylation in blood cancer dna using terahertz radiation. *Scientific Reports (Nature Publisher Group)*, 9(1), 2019.

[28] DH Auston, KP Cheung, and PR Smith. Picosecond photoconducting hertzian dipoles. *Applied physics letters*, 45(3):284–286, 1984.

[29] G Zhao, RN Schouten, N Van der Valk, W Th Wenckebach, and PCM Planken. Design and performance of a thz emission and detection setup based on a semi-insulating gaas emitter. *Review of Scientific Instruments*, 73(4):1715–1719, 2002.

[30] J Hawecker, V Pistore, A Minasyan, K Maussang, J Palomo, I Sagnes, JM MANCEAU, R Colombelli, J Tignon, J Mangeney, et al. Cavity-based photoconductive sources for real-time terahertz imaging. 2019.

[31] Nezih T Yardimci, Shang-Hua Yang, Christopher W Berry, and Mona Jarrahi. High-power terahertz generation using large-area plasmonic photoconductive emitters. *IEEE Transactions on Terahertz Science and Technology*, 5(2):223–229, 2015.

[32] Shang-Hua Yang, Mohammed R Hashemi, Christopher W Berry, and Mona Jarrahi. 7.5% optical-to-terahertz conversion efficiency through use of three-dimensional plasmonic electrodes. In *CLEO: QELS_Fundamental Science*, pages FTh4K–2. Optical Society of America, 2014.

[33] A Singh, A Pashkin, S Winnerl, M Helm, and H Schneider. Gapless broadband terahertz emission from a germanium photoconductive emitter. *ACS Photonics*, 5(7):2718–2723, 2018.

[34] Abhishek Singh, Alexej Pashkin, Stephan Winnerl, Malte Welsch, Cornelius Beckh, Philipp Sulzer, Alfred Leitenstorfer, Manfred Helm, and Harald Schneider. Up to 70 thz bandwidth from an implanted ge photoconductive antenna excited by a femtosecond er: fibre laser. *Light: Science & Applications*, 9(1):1–7, 2020.

[35] Ingrid Wilke and Suranjana Sengupta. Nonlinear optical techniques for terahertz pulse generation and detection—optical rectication and electrooptic sampling. In *Terahertz Spectroscopy*, pages 59–90. CRC press, 2017.

[36] Imran Mehdi, Jose V Siles, Choonsup Lee, and Erich Schlecht. Thz diode technology: status, prospects, and applications. *Proceedings of the IEEE*, 105(6):990–1007, 2017.

[37] John C Pearson, Brian J Drouin, Alain Maestrini, Imran Mehdi, John Ward, Robert H Lin, Shanshan Yu, John J Gill, Bertrand Thomas, Choonsup Lee, et al. Demonstration of a room temperature 2.48–2.75 thz coherent spectroscopy source. *Review of Scientific Instruments*, 82(9):093105, 2011.

[38] Miriam Serena Vitiello, Giacomo Scalari, Benjamin Williams, and Paolo De Natale. Quantum cascade lasers: 20 years of challenges. *Optics express*, 23(4):5167–5182, 2015.

[39] Mikhail A Belkin, Federico Capasso, Alexey Belyanin, Deborah L Sivco, Alfred Y Cho, Douglas C Oakley, Christopher J Vineis, and George W Turner. Terahertz quantum-cascade-laser source based on intracavity difference-frequency generation. *Nature Photonics*, 1(5):288–292, 2007.

[40] MA Belkin, F Capasso, F Xie, A Belyanin, M Fischer, A Wittmann, and J Faist. Microwatt-level terahertz intra-cavity difference-frequency generation in mid-infrared quantum cascade lasers. *Appl. Phys. Lett*, 92:201101, 2008.

[41] C Sirtori, F Capasso, Jérôme Faist, LN Pfeiffer, and KW West. Far-infrared generation by doubly resonant difference frequency mixing in a coupled quantum well two-dimensional electron gas system. *Applied physics letters*, 65(4):445–447, 1994.

[42] QY Lu, N Bandyopadhyay, S Slivken, Y Bai, and Manijeh Razeghi. Continuous operation of a monolithic semiconductor terahertz source at room temperature. *Applied Physics Letters*, 104(22):221105, 2014.

[43] Christopher A Curwen, John L Reno, and Benjamin S Williams. Terahertz quantum cascade vecsel with watt-level output power. *Applied Physics Letters*, 113(1):011104, 2018.

[44] Ali Khalatpour, John L Reno, Nazir P Kherani, and Qing Hu. Unidirectional photonic wire laser. *Nature Photonics*, 11(9):555–559, 2017.

[45] David Burghoff, Tsung-Yu Kao, Ningren Han, Chun Wang Ivan Chan, Xiaowei Cai, Yang Yang, Darren J Hayton, Jian-Rong Gao, John L Reno, and Qing Hu. Terahertz laser frequency combs. *Nature Photonics*, 8(6):462–467, 2014.

[46] Markus Rösch, Giacomo Scalari, Mattias Beck, and Jérôme Faist. Octave-spanning semiconductor laser. *Nature Photonics*, 9(1):42, 2015.

[47] Tsung-Yu Kao, John L Reno, and Qing Hu. Amplifiers of free-space terahertz radiation. *Optica*, 4(7):713–716, 2017.

[48] Karl Unterrainer, Raffaele Colombelli, Claire Gmachl, Federico Capasso, Harold Y Hwang, A Michael Sergent, Deborah L Sivco, and Alfred Y Cho. Quantum cascade lasers with double metal-semiconductor waveguide resonators. *Applied physics letters*, 80(17):3060–3062, 2002.

[49] ZR Wasilewski. Mbe growth of thz quantum cascade lasers. In *Molecular Beam Epitaxy*, pages 631–655. Elsevier, 2013.

[50] AJL Adam, I Kašalynas, JN Hovenier, TO Klaassen, JR Gao, EE Orlova, BS Williams, S Kumar, Q Hu, and JL Reno. Beam patterns of terahertz quantum cascade lasers with subwavelength cavity dimensions. *Applied Physics Letters*, 88(15):151105, 2006.

[51] Martin T Hill and Malte C Gather. Advances in small lasers. *Nature Photonics*, 8(12):908, 2014.

[52] MA Noginov, G Zhu, AM Belgrave, Reuben Bakker, VM Shalaev, EE Narimanov, S Stout, E Herz, T Suteewong, and U Wiesner. Demonstration of a spaser-based nanolaser. *Nature*, 460(7259):1110–1112, 2009.

[53] Rupert F Oulton, Volker J Sorger, Thomas Zentgraf, Ren-Min Ma, Christopher Gladden, Lun Dai, Guy Bartal, and Xiang Zhang. Plasmon lasers at deep subwavelength scale. *Nature*, 461(7264):629–632, 2009.

[54] JP Zhang, DY Chu, SL Wu, Seng-Tiong Ho, WG Bi, CW Tu, and RC Tiberio. Photonic-wire laser. *Physical review letters*, 75(14):2678, 1995.

[55] Martin T Hill, Yok-Siang Oei, Barry Smalbrugge, Youcai Zhu, Tjibbe De Vries, Peter J Van Veldhoven, Frank WM Van Otten, Tom J Eijkemans, Jarosław P Turkiewicz, Huug De Waardt, et al. Lasing in metallic-coated nanocavities. *Nature Photonics*, 1(10):589, 2007.

[56] EE Orlova, JN Hovenier, TO Klaassen, I Kašalynas, AJL Adam, JR Gao, TM Klapwijk, BS Williams, S Kumar, Q Hu, et al. Antenna model for wire lasers. *Physical review letters*, 96(17):173904, 2006.

[57] Qi Qin, Benjamin S Williams, Sushil Kumar, John L Reno, and Qing Hu. Tuning a terahertz wire laser. *Nature photonics*, 3(12):732, 2009.

[58] Benjamin S Williams, Sushil Kumar, Qing Hu, and John L Reno. Distributed-feedback terahertz quantum-cascade lasers with laterally corrugated metal waveguides. *Optics letters*, 30(21):2909–2911, 2005.

[59] Sushil Kumar, Benjamin S Williams, Qi Qin, AlanW M Lee, Qing Hu, and John L Reno. Surface-emitting distributed feedback terahertz quantum-cascade lasers in metal-metal waveguides. *Optics Express*, 15(1):113–128, 2007.

[60] Simone Biasco, Andrea Ciavatti, Lianhe Li, A Giles Davies, Edmund H Linfield, Harvey Beere, David Ritchie, and Miriam S Vitiello. Highly efficient surface-emitting semiconductor lasers exploiting quasi-crystalline distributed feedback photonic patterns. *Light: Science & Applications*, 9(1):1–11, 2020.

[61] Simone Biasco, Katia Garrasi, Fabrizio Castellano, Lianhe Li, Harvey E Beere, David A Ritchie, Edmund H Linfield, A Giles Davies, and Miriam S Vitiello. Continuous-wave highly-efficient low-divergence terahertz wire lasers. *Nature communications*, 9(1):1–8, 2018.

[62] Yuan Jin, Liang Gao, Ji Chen, Chongzhao Wu, John L Reno, and Sushil Kumar. High power surface emitting terahertz laser with hybrid second-and fourth-order bragg gratings. *Nature communications*, 9(1):1–7, 2018.

[63] Gangyi Xu, Lianhe Li, Nathalie Isac, Yacine Halioua, A Giles Davies, Edmund H Linfield, and Raffaele Colombelli. Surface-emitting terahertz quantum cascade lasers with continuous-wave power in the tens of milliwatt range. *Applied Physics Letters*, 104(9):091112, 2014.

[64] Carlo Sirtori, Stefano Barbieri, and Raffaele Colombelli. Wave engineering with thz quantum cascade lasers. *Nature Photonics*, 7(9):691, 2013.

[65] Y Ren, DJ Hayton, JN Hovenier, M Cui, JR Gao, TM Klapwijk, SC Shi, T-Y Kao, Q Hu, and JL Reno. Frequency and amplitude stabilized terahertz quantum cascade laser as local oscillator. *Applied Physics Letters*, 101(10):101111, 2012.

[66] Maria I Amanti, M Fischer, G Scalari, M Beck, and Jérôme Faist. Low-divergence single-mode terahertz quantum cascade laser. *Nature Photonics*, 3(10):586, 2009.

[67] Maria I Amanti, Giacomo Scalari, Fabrizio Castellano, Mattias Beck, and Jerome Faist. Low divergence terahertz photonic-wire laser. *Optics express*, 18(6):6390–6395, 2010.

[68] Tsung-Yu Kao, Qing Hu, and John L Reno. Perfectly phase-matched third-order distributed feedback terahertz quantum-cascade lasers. *Optics letters*, 37(11):2070–2072, 2012.

[69] M Wienold, B Röben, L Schrottke, R Sharma, A Tahraoui, K Biermann, and HT Grahn. High-temperature, continuous-wave operation of terahertz quantum-cascade lasers with metal-metal waveguides and third-order distributed feedback. *Optics express*, 22(3):3334–3348, 2014.

[70] Tsung-Yu Kao, Xiaowei Cai, Alan WM Lee, John L Reno, and Qing Hu. Antenna coupled photonic wire lasers. *Optics express*, 23(13):17091–17100, 2015.

[71] CK Walker, C Kulesa, P Goldsmith, C Groppi, C Helmich, D Hollenbach, J Kawamura, W Langer, G Melnick, D Neufeld, et al. Gusto: Gal/xgal u/ldb spectroscopic-stratospheric terahertz observatory. In *231st American Astronomical Society (AAS) Meeting*, 2018.

[72] PH Siegel and RJ Dengler. Applications & early results from thz heterodyne imaging at 119/spl mu/m. In *Infrared and Millimeter Waves, Conference Digest of the 2004 Joint 29th International Conference on 2004 and 12th International Conference on Terahertz Electronics, 2004.*, pages 555–556. IEEE.

[73] Constantine A Balanis. *Modern antenna handbook*. John Wiley & Sons, 2011.

[74] Constantine A Balanis. *Antenna theory: analysis and design*. John wiley & sons, 2016.

[75] Jérôme Faist. Wallplug efficiency of quantum cascade lasers: Critical parameters and fundamental limits. *Applied physics letters*, 90(25):253512, 2007.

[76] David Burghoff, Tsung-Yu Kao, Dayan Ban, Alan Wei Min Lee, Qing Hu, and John Reno. A terahertz pulse emitter monolithically integrated with a quantum cascade laser. *Applied Physics Letters*, 98(6):061112, 2011.

[77] Alan WM Lee, Qi Qin, Sushil Kumar, Benjamin S Williams, Qing Hu, and John L Reno. Real-time terahertz imaging over a standoff distance ($>$ 25 meters). *Applied Physics Letters*, 89(14):141125, 2006.

[78] Chongzhao Wu, Sudeep Khanal, John L Reno, and Sushil Kumar. Terahertz plasmonic laser radiating in an ultra-narrow beam. *Optica*, 3(7):734–740, 2016.

[79] Christopher A Curwen, Luyao Xu, John L Reno, Tatsuo Itoh, and Benjamin S Williams. Broadband continuous tuning of a thz quantum-cascade vecsel. In *CLEO: Science and Innovations*, pages STh4O–2. Optical Society of America, 2017.

[80] Luyao Xu, Christopher A Curwen, Daguan Chen, John L Reno, Tatsuo Itoh, and Benjamin S Williams. Terahertz metasurface quantum-cascade vecsels: Theory and performance. *IEEE Journal of Selected Topics in Quantum Electronics*, 23(6):1–12, 2017.

[81] Qi Qin, John L Reno, and Qing Hu. Mems-based tunable terahertz wire-laser over 330 ghz. *Optics letters*, 36(5):692–694, 2011.

[82] Ningren Han, Alexander de Geofroy, David P Burghoff, Chun Wang I Chan, Alan Wei Min Lee, John L Reno, and Qing Hu. Broadband all-electronically tunable mems terahertz quantum cascade lasers. *Optics letters*, 39(12):3480–3483, 2014.

[83] Dana Turčinková, Maria Ines Amanti, Giacomo Scalari, Mattias Beck, and Jérôme Faist. Electrically tunable terahertz quantum cascade lasers based on a two-sections interdigitated distributed feedback cavity. *Applied Physics Letters*, 106(13):131107, 2015.

[84] L Andrea Dunbar, Romuald Houdré, Giacomo Scalari, Lorenzo Sirigu, Marcella Giovannini, and Jérôme Faist. Small optical volume terahertz emitting microdisk quantum cascade lasers. *Applied physics letters*, 90(14):141114, 2007.

[85] Hua Zhang, Giacomo Scalari, Jérôme Faist, L Andrea Dunbar, and Romuald Houdré. Design and fabrication technology for high performance electrical pumped terahertz photonic crystal band edge lasers with complete photonic band gap. *Journal of Applied Physics*, 108(9):093104, 2010.

[86] Le Zhao, Sudeep Khanal, Liang Gao, John L Reno, and Sushil Kumar. Electrical tuning of single-mode terahertz quantum-cascade lasers operating at high temperatures. In *2016 IEEE Photonics Conference (IPC)*, pages 76–77. IEEE, 2016.

[87] DE Ackley. Single longitudinal mode operation of high power multiple-stripe injection lasers. *Applied Physics Letters*, 42(2):152–154, 1983.

[88] JOSEPH Katz, S Margalit, and AMNON Yariv. Diffraction coupled phase-locked semiconductor laser array. *Applied Physics Letters*, 42(7):554–556, 1983.

[89] Daniel Brunner and Ingo Fischer. Reconfigurable semiconductor laser networks based on diffractive coupling. *Optics letters*, 40(16):3854–3857, 2015.

[90] K-L Chen and Shyh Wang. Single-lobe symmetric coupled laser arrays. *Electronics letters*, 21(8):347–349, 1985.

[91] William Streifer, DAVIDF Welch, PETERS Cross, and DONALDR Scifres. Y-junction semiconductor laser arrays: Part i–theory. *IEEE Journal of Quantum Electronics*, 23(6):744–751, 1987.

[92] D Botez and G Peterson. Modes of phase-locked diode-laser arrays of closely spaced antiguides. *Electronics Letters*, 24(16):1042–1044, 1988.

[93] D Botez. High-power monolithic phase-locked arrays of antiguided semiconductor diode lasers. *IEE Proceedings J (Optoelectronics)*, 139(1):14–23, 1992.

[94] Tsung-Yu Kao, Qing Hu, and John L Reno. Phase-locked arrays of surface-emitting terahertz quantum-cascade lasers. *Applied Physics Letters*, 96(10):101106, 2010.

[95] Tsung-Yu Kao, John L Reno, and Qing Hu. Phase-locked laser arrays through global antenna mutual coupling. *Nature Photonics*, 10(8):541, 2016.

[96] DM Roessler. Kramers-kronig analysis of reflection data. *British Journal of Applied Physics*, 16(8):1119, 1965.

[97] Nicol Beverini, Giorgio Carelli, Andrea De Michele, Augusto Moretti, Lukas Mahler, Alessandro Tredicucci, Harvey E Beere, and David A Ritchie. Frequency characterization of a terahertz quantum-cascade laser. *IEEE Transactions on Instrumentation and Measurement*, 56(2):262–265, 2007.

[98] Gernot Fasching, Vincas Tamosiunas, Alexander Benz, Aaron Maxwell Andrews, Karl Unterrainer, Reinhard Zobl, Tomas Roch, Werner Schrenk, and Gottfried Strasser. Subwavelength microdisk and microring terahertz quantum-cascade lasers. *IEEE journal of quantum electronics*, 43(8):687–697, 2007.

[99] L Rezac, P Hartogh, R Güsten, H Wiesemeyer, H-W Hübers, C Jarchow, H Richter, B Klein, and N Honingh. First detection of the 63 μm atomic oxygen line in the thermosphere of mars with great/sofia. *Astronomy & Astrophysics*, 580:L10, 2015.

[100] Jenna L Kloosterman, Darren J Hayton, Yuan Ren, Tsung-Yu Kao, JN Hovenier, Jian-Rong Gao, Teun M Klapwijk, Qing Hu, Christopher K Walker, and John L Reno. Hot electron bolometer heterodyne receiver with a 4.7-thz quantum cascade laser as a local oscillator. *Applied Physics Letters*, 102(1):011123, 2013.

[101] B Mirzaei, JRG Silva, D Hayton, Christopher Groppi, TY Kao, Q Hu, John L Reno, and JR Gao. 8-beam local oscillator array at 4.7 thz generated by a phase grating and a quantum cascade laser. *Optics express*, 25(24):29587–29596, 2017.

[102] B Mirzaei, JRG Silva, D Hayton, W Laauwen, Y Gan, Q Hu, Christopher Groppi, and JR Gao. Prototype 4.7 thz array local oscillator for gusto. In *29th IEEE International Symposium on Space Terahertz Technology, ISSTT 2018*, 2018.

[103] JR Silva, R Farinha, DJ Hayton, W Laauwen, B Mirzaei, N More, A Young, C Kulesa, C Walker, and JR Gao. Preliminary design study of a 4× 2 heb array at 4.7 thz for gusto. In *Proc. of the 29th Int. Symp. on Space Terahertz Technology/Caltech. Pasadena, CA, USA*, pages 82–86, 2018.

[104] Yuner Gan, Behnam Mirzaei, Jose RG Silva, Ali Khalatpour, Qing Hu, Christopher Groppi, Jose V Siles, Floris van der Tak, and Jian-Rong Gao. 81 supra-thz beams generated by a fourier grating and a quantum cascade laser. *Optics Express*, 27(23):34192–34203, 2019.

[105] Keita Ohtani, Dana Turčinková, Christopher Bonzon, Ileana-Cristina Benea-Chelmus, Mattias Beck, Jérôme Faist, Matthias Justen, Urs U Graf, Marc

Mertens, and Jürgen Stutzki. High performance 4.7 thz gaas quantum cascade lasers based on four quantum wells. *New Journal of Physics*, 18(12):123004, 2016.

[106] Asaf Albo and Qing Hu. Carrier leakage into the continuum in diagonal gaas/al0. 15gaas terahertz quantum cascade lasers. *Applied Physics Letters*, 107(24):241101, 2015.

[107] Asaf Albo, Qing Hu, and John L Reno. Room temperature negative differential resistance in terahertz quantum cascade laser structures. *Applied Physics Letters*, 109(8):081102, 2016.

[108] Chun Wang I Chan, Asaf Albo, Qing Hu, and John L Reno. Tradeoffs between oscillator strength and lifetime in terahertz quantum cascade lasers. *Applied Physics Letters*, 109(20):201104, 2016.

[109] Sushil Kumar, Chun Wang I Chan, Qing Hu, and John L Reno. Two-well terahertz quantum-cascade laser with direct intrawell-phonon depopulation. *Applied Physics Letters*, 95(14):141110, 2009.

[110] G Scalari, MI Amanti, C Walther, R Terazzi, M Beck, and Jérôme Faist. Broadband thz lasing from a photon-phonon quantum cascade structure. *optics Express*, 18(8):8043–8052, 2010.

[111] Asaf Albo, Yuri V Flores, Qing Hu, and John L Reno. Two-well terahertz quantum cascade lasers with suppressed carrier leakage. *Applied Physics Letters*, 111(11):111107, 2017.

[112] H Page, C Becker, A Robertson, G Glastre, V Ortiz, and C Sirtori. 300 k operation of a gaas-based quantum-cascade laser at λ 9 μm. *Applied Physics Letters*, 78(22):3529–3531, 2001.

[113] Martin Franckié, Lorenzo Bosco, Mattias Beck, Christopher Bonzon, Elena Mavrona, Giacomo Scalari, Andreas Wacker, and Jérôme Faist. Two-well quantum cascade laser optimization by non-equilibrium green's function modelling. *Applied Physics Letters*, 112(2):021104, 2018.

[114] Martin Franckié and Jérôme Faist. Bayesian optimization of terahertz quantum cascade lasers. *Physical Review Applied*, 13(3):034025, 2020.

[115] Carlo Sirtori, Federico Capasso, Jérôme Faist, and Sandro Scandolo. Nonparabolicity and a sum rule associated with bound-to-bound and bound-to-continuum intersubband transitions in quantum wells. *Physical Review B*, 50(12):8663, 1994.

[116] ZR Wasilewski, MM Dion, DJ Lockwood, P Poole, RW Streater, and AJ SpringThorpe. Composition of algaas. *Journal of applied physics*, 81(4):1683–1694, 1997.

[117] Yin Wang, Ferdows Zahid, Yu Zhu, Lei Liu, Jian Wang, and Hong Guo. Band offset of gaas/al x ga1- x as heterojunctions from atomistic first principles. *Applied Physics Letters*, 102(13):132109, 2013.

[118] Miriam S Vitiello, Rita C Iotti, Fausto Rossi, Lukas Mahler, Alessandro Tredicucci, Harvey E Beere, David A Ritchie, Qing Hu, and Gaetano Scamarcio. Non-equilibrium longitudinal and transverse optical phonons in terahertz quantum cascade lasers. *Applied physics letters*, 100(9):091101, 2012.

[119] Jérôme Faist. *Quantum cascade lasers*. OUP Oxford, 2013.

[120] Ali Khalatpour, Andrew K. Paulsen, Chris Deimert, Zbig R. Wasilewski, and Qing Hu. High power portable terahertz laser systems. *Nature Photonics*, 2020.

[121] A Wade, G Fedorov, D Smirnov, S Kumar, BS Williams, Q Hu, and JL Reno. Magnetic-field-assisted terahertz quantum cascade laser operating up to 225 k. *Nature Photonics*, 3(1):41–45, 2009.

[122] Martin A Kainz, Mykhaylo P Semtsiv, Georgios Tsianos, Sergii Kurlov, W Ted Masselink, Sebastian Schönhuber, Hermann Detz, Werner Schrenk, Karl Unterrainer, Gottfried Strasser, et al. Thermoelectric-cooled terahertz quantum cascade lasers. *Optics express*, 27(15):20688–20693, 2019.